SENTINEL-1 WIDE SWATH INTERFEROMETRY: PROCESSING TECHNIQUES AND APPLICATIONS

by

Yuxiao Qin

A Dissertation

Submitted to the Faculty of Purdue University

In Partial Fulfillment of the Requirements for the degree of

Doctor of Philosophy

Lyles School of Civil Engineering

West Lafayette, Indiana

December 2018

THE PURDUE UNIVERSITY GRADUATE SCHOOL
STATEMENT OF DISSERTATION APPROVAL

Dr. Daniele Perissin, Chair

Lyles School of Civil Engineering

Dr. Mark Bell

School of Electrical and Computer Engineering

Dr. Julie Elliott

Department of Earth, Atmospheric, and Planetary Sciences

Dr. Ayman Habib

Lyles School of Civil Engineering

Approved by:

Dr. Dulcy Abraham

Lyles School of Civil Engineering

To Yin JIANG

ACKNOWLEDGMENTS

Eleven years ago, I attended a sophomore class called cartography. Back then I was just an ignorant undergrad who was just too busy having fun and had no idea what I would do in the future. However, when I went deeper into that course, I was utterly humbled by the professor who taught the class. The materials were not really hard, but she taught us with extreme carefulness and rigor. She would review all of our reports and homework every time by herself. She would never let go even a tiny mistake, and she would ask students to revise over and over until the work is perfect. She is one of the few who genuinely cares about the student, and who poses the highest standard for herself and her students. I followed her in my undergrad research because of this. And if it is not for her, I would never walk into the field of SAR/InSAR. Although I only had two years of time studying with her (and sadly, I squandered a lot of time as an undergrad), professor JIAO Jian is always my role model as a scholar. Thank you, Professor JIAO Jian.

Then I moved to the Chinese University of Hong Kong for the next level. As a freshman in the field of SAR remote sensing, I met Dr. Daniele Perissin. There is no needs to praise more about his passion, diligence, and professionalism in the field. A few things could reflect how he influenced my career path. I studied and worked with him every day for eight years. I quit my first Ph.D. in Hong Kong just to follow him to Purdue University. He taught me from knowing nothing to becoming a PhD. Everything I know in this field comes from him. Thank you, Professor Daniele Perissin.

There is always my gratitude to Purdue University, an ideal place to meditate, to learn and to research.

The most important thank you is reserved for my family. Eight years of graduate studies is a long time (especially when I was always moving around and "fiddling around" for new challenges), and I could not possibly survive it without the unconditional support of my wife, Yin. Ten years since we have been together, she rescued me a dozen times from my breakdowns and supported me all the way along. I want to thank my parents-in-law for their support all these years while we are not always around. At last, the thanks go to my mum and dad. Although they didn't like the idea of me spending a lot of times on going to classes in ECE, they still supported me by paying all the tuitions and living expenses. :) I guess that is what family does.

the inner voice of my mum

TABLE OF CONTENTS

Page

Page

LIST OF FIGURES

Figure Page

Figure Page

ABBREVIATIONS

AOI	Area Of Interest
AAP	Azimuth Antenna beam Pattern
CRLB	Cramér-Rao Lower Bound
DEM	Digital Elevation Model
DLR	German Aerospace Center
ESD	Enhanced Spectral Diversity
ESA	European Space Agency
EW	Extra Wide swath
FM	Frequency Modulated
IRF	Impulse Response Function
InSAR	SAR Interferometry
IW	Interferometric Wide swath
NASA	the National Aeronautics and Space Administration
MLE	Maximum Likelihood Estimator
MST	Minimum Spanning Tree
PRF	Pulse Repetition Frequency
PRI	Pulse Repetition Interval
PSI	Persistent Scatterer Interferometry
S1	Sentinel-1
S1A	Sentinel-1A
S1B	Sentinel-1B
SAR	Synthetic Aperture Radar
SLC	Single Look Complex
SNR	Signal to Noise Ratio

SCR	Signal Clutter Ratio
SRTM	Shuttle Radar Topography Mission
SM	stripmap
TDE	Time Delay Estimation
TOPS	Terrain Observation by Progressive Scans
TSA	Time Series Analysis
WS	Wide Swath
WV	WaVe mode

ABSTRACT

QIN Yuxiao Ph.D., Purdue University, December 2018. Sentinel-1 Wide Swath Interferometry: Processing Techniques and Applications. Major Professor: Daniele Perissin.

The Sentinel-1 (S1) mission is a part of the European Space Agency (ESA) Copernicus program. In 2014 and 2016, the mission launched the twin Synthetic Aperture Radar (SAR) satellites, Sentinel-1A (S1A) and Sentinel-1B (S1B). The S1 mission has started a new era for earth observations missions with its higher spatial resolution, shorter revisit days, more precise control of satellites orbits and the unprecedented free-to-public distribution policy. More importantly, S1 adopts a new wide swath mode, the TOPS mode as it default acquisition mode. The TOPS mode scans several different subswaths for gaining a larger coverage. Because the S1 mission is aimed at earth observation missions, for example, earthquakes, floods, ice sheets flow, etc., thus it is desired to have large monitoring areas. Although TOPS is still a relatively new idea, the high quality data and wide application scopes from S1 has earned tremendous attention in the SAR community.

The signal properties of wide swath mode such as TOPS are different from the more conventional stripmap mode, and it requires special techniques for successfully processing such data in the sense of interferometry. For the purpose of doing Interferometric SAR (InSAR), the coregistration step is of most critical because it requires a 1/1000 accuracy. In addition, processing wide swath mode requires special steps such as bursts stitching, deramping and reramping, and so on. Compared with stripmap, the processing techniques of wide swath mode are less developed. Much exploitations are still needed for how to design a generic and robust wide swath interferometric processing chain.

Driven by the application needs of S1 wide swath interferometric processing, this research studies the key methodologies, explores and implements new processing chain, designs a generic wide swath processing flow that would utilize the existing stripmap processing platform, as well as carries out preliminary applications. For studying key methods, this study carries out a quantitative analysis between two different coregistration methods, namely the cross-correlation approach and the geometrical approach. The advantages and disadvantages for each method are given by the author, and it is proposed to choose the suitable method based on one's study area. For the implementation of the new processing chain, the author proposes a user-friendly stripmap-like processing flow with all the wide swath related process done behind the scene. This approach allows people with basic knowledge in InSAR and very few knowledge in wide swath mode to be able to process and get interferometric products. For designing the generic process flow, the author applied TOPS's workflow to the other wide swath mode, ScanSAR mode and demonstrated the feasibility of processing two different wide swath mode with the same processing chain. For preliminary applications, the author shows a large number of interferometric data throughout the research and presents a case study with multi temporal time series analysis using a stack of S1 dataset.

This research is application oriented, which means the study serves for real-world applications. Up to now, the processing chain and methodologies implemented in this research has been shared by many research groups around the world and has seen a number of promising outcomes. The recognition from others is also an affirmation to the value of this research.

1. INTRODUCTION

1.1 Background of Sentinel-1A/B SAR Satellite Constellation

The Sentinel-1 (S1) mission serves under the European Space Agency (ESA) Copernicus program and consists of two identical C-band Synthetic Aperture Radar (SAR) satellites. The first satellite, Sentinel-1A (S1A), was launched in April 2014. Its twin, Sentinel-1B (S1B), was launched in April 2016. Up to January 2018, more than two million S1 products were made available to the public, representing 3.4 PB of data. Upon the launch of the S1 mission, the entire Europe are being routinely scanned every six days per track and the majority of the rest of the world are being scanned every twelve days per track. This has made S1 the richest SAR data source at almost everywhere in the world. It is especially worth mentioning that, all S1 data are free to the public. Although this is not a technical detail, the free distribution policy is significant for promoting SAR and Interferometric SAR (InSAR), and it is indeed opening an new era for the entire SAR/InSAR community.

Unlike any other space-borne SAR sensors that use the stripmap as the default operating mode, S1 is the first long-term-mission space-borne satellite that operates in the wide swath (WS) mode as its default scanning mode (another space-borne satellite mission with wide swath mode is the Shuttle Radar Topography Mission (SRTM) by NASA in 2000, but the mission only lasted eleven days for generating the world wide digital elevation model (DEM) data [1]). The initiative behind using wide swath as the default mode is to scan larger area at an acceptable pixel resolution.

Here it is worth tracing back a bit into the history of the wide swath mode. In the conventional stripmap mode, the range width is restrained by the pulse repetition frequency (PRF), nadir return and received window timing [2]. For the purpose of scanning larger areas by increasing the swath width, in 1981 Tomiyasu [3] and Moore

[4] proposed the ScanSAR mode. The name ScanSAR comes from the "scanning" antenna in different swaths as a tradeoff to azimuth resolution. Nowadays ScanSAR is widely implemented in most of the synthetic aperture radar (SAR) sensors, including Radarsat, Envisat, TerraSAR-X, COSMO, and ALOS-1&2.

However, ScanSAR system is not initially designed for interferometry. It is not until the 1990s when Politecnico di Milano [5] and German Aerospace Center [6] started relevant work. One of the most successful ScanSAR interferometric application is the SRTM mission in 2000 [1], where the global topography was mapped in an eleven-days mission. In 2005, the ESA started to release ScanSAR single look complex (SLC) products for the interferometric purpose.

Still, for a few reasons, despite the long history of ScanSAR interferometry, its scientific studies and applications are very limited. To start with, the first generation of ScanSAR, such as Envisat ASAR, has a very low spatial resolution (8 m slant range $\times$ 80 m azimuth). The low resolution makes the speckle effect worse and hence restricts the application scope for interferometry. Secondly, Envisat ScanSAR has very limited ability to control burst synchronization [7, 8]. This will lead to the loss in the azimuth common bandwidth [9] and the decorrelation in the interferogram. Another issue with ScanSAR system for the interferometric purpose is the scalloping effect [10]. In ScanSAR mode, ground targets at different azimuth positions are illuminated by the different portion of the azimuth antenna beam pattern (AAP). As a result, the received signal to noise ratio (SNR) becomes azimuth dependent. While the amplitude modulation in the scalloping effect could be compensated by multilook, it would be very unlikely to correct the azimuth-dependent SNR for interferometric purpose [5]. A low SNR at the edges of the bursts will decrease the coherence in interferometry. The TOPS mode is hence proposed to minimize the scalloping effect in interferometry [10].

In the TOPS mode, the antenna sweeps in the opposite direction to a SPOT mode, hence the name "TOPS" [10]. In the ScanSAR mode, the antenna only switches between different subswath without any "sweeping" along azimuth. In the TOPS

mode, the antenna "sweeps" in the azimuth direction in each subswath to gain a larger scanning area. In TOPS mode all targets are scanned by the entire AAP, and their amplitude gain are at the same level. There is still a minor scalloping effect in TOPS, but it is mainly due to phase array steering and grating lobes [11, 12]. The ESA distributed SLC data has also corrected this effect [13].

This new acquisition mode was firstly tested on the German satellite TerraSAR-X for validation [14–16]. Then in 2014, the Sentinel-1 mission made TOPS famous by setting TOPS as the default acquisition mode and by distributing the data for free to the public. Comparing with Envisat ScanSAR, S1 increases the azimuth resolution to around 20 meters, decreases revisit time to 12 days, tightens the orbital to a 200 meters tube to favor interferometry. At last, S1 achieves a perfect timing control, baseline control and burst synchronization so that the temporal, geometrical and spectral decorrelation could be minimized [13, 17]. The superb control of S1 burst synchronization means that in most cases there will be no significant coherence loss even if no filtering in azimuth is performed [9]. Unlike its ancestors, every detail in S1 TOPS mode is aimed at doing interferometry [18, 19].

Since the launching of the twin satellites in 2014, Sentinel-1 system has played important roles with its TOPS mode in delivering interferometric product. The system has reacted superbly fast in the events of a number of natural hazards and has provided invaluable information. To name a few, the 2015 Chile Illapel earthquake of magnitude 8.3 [20], 2016 New Zealand earthquake of magnitude 7.8 [21], landslide in Maoxian County in China [22] and the urban area ground subsidence in Beijing China [23], along with many other successful case studies. Up to now (August 2018), the twin satellites S1A & S1B are still operating in their excellent shapes and are keeping providing massive real time data of the earth.

1.2 Significances and Challenges of Sentinel-1

Unlike the ScanSAR system, which was not initially designed for interferometric purpose, TOPS is designed for delivering interferometric products as one of its top priorities from the very beginning. For this purpose, S1 system shows its significances in the following way:

1. Systematic acquisitions. For the old sensors, the acquisition capability is rather limited and haphazard. On the other side, S1 maintains a systematic routine operation that covers almost the entire land on earth. The rich dataset gives us the opportunity to keep track of long term changes in almost any study area on earth. What is more important is that the designed operations lifetime of S1 is more than 20 years [24]. The long time series could give raise to a more accurate deformation monitoring in the long run [18];

2. Wide swath coverage. In the wide swath mode, S1 scans three subswaths; In the extra wide swath mode, S1 scans five subswaths. The large coverage provides convenience for monitoring large scale ground movements such as earthquakes and ice sheet flows;

3. Short temporal baseline. Temporal coherence decays exponentially [25]. For InSAR and time series analysis, it is desired to have short temporal baseline and high coherence. Both S1A and S1B provides 12 day revisiting time, and the cross revisit time between S1A and S1B could be 6 days;

4. Short spatial baseline. The S1 constellation flies within a tube of 200 meters diameter with an excellent control of orbits [13]. Shorter spatial baseline reduce geometrical decorrelation [26]. The combination of short temporal and spatial baseline can greatly reduce the decorrelation effect and provide an ideal condition for carrying out time series analysis such as persistent scatterers interferometry (PSI). As a matter of fact, ESA has even relaxed the orbital normal

Table 1.1.
Selected Parameters for S1 TOPS SLC Product

Revisit Days	12 days (6 days for S1A-S1B)
Band	C
Wavelength	5.55cm
Range Resolution	2.7-3.5m
Incidence Angle	∼30-45°
Ground Subswath Width	∼80km
Azimuth Resolution	22m
Azimuth Bandwidth	∼ 320Hz
PRF	486 Hz
Doppler Centroid Span	4.6-5.2 kHz
Azimuth Steering Angle	±0.6°
Burst Length	2.75s (∼20km)
Price Per Image	Free

baseline a bit to allow for a better estimation of the relative height for persistent scatterers [27].

Despite the excellent product quality of S1, there are still a few challenges in TOPS interferometric processing:

1. Coregistration. In the stripmap mode, a miscoregistration introduces decorrelation to the interferogram. In the wide swath mode, such as TOPS and ScanSAR, an additional interferometric phase error is also introduced by miscoregistration. Meanwhile, due to the large doppler centroid that is introduced by the azimuth steering that exceeds the pulse repetition frequency (PRF), TOPS requires a 0.001 pixel coregistration accuracy so that the interferometric phase error due to miscoregistration is below 0.05 radians [28]. The commu-

nity has suggested a common workflow [28] using the geometrical coregistration method [29] followed by the enhanced spectral diversity (ESD) method [14]. However, the coregistration accuracy of this method depends on the precision of the orbits, thus it only works with orbits of high accuracy [29, 30]. There are still some open room for discussing other coregistration methods. For example, it would be interesting to understand the performance of the conventional cross-correlation-and-rigid-transformation method, which does not rely on the orbital information at all;

2. The promotion a user-friendly wide swath mode processing package. Despite the increasing popularity of the wide swath mode, the interferometric process is still more complicated than the stripmap mode. For users who only have the basic familiarity with the stripmap mode, and simply wish to derive the interferometric product for their own earth observation applications, the burst mode of wide swath looks quite counterintuitive. In addition, the wide swath mode requires extra steps in the coregistration, including deramping/reramping and ESD, that requires some fundamental understanding to the signal characteristics of the wide swath mode. It is desired to have a user-friendly processing package that could give users the interferometric products for TOPS without any prerequisites on wide swath mode;

3. Coregistering a stack of images. The accuracy of ESD method depends on spatial coherence, but coherence decays exponentially in time [25]. For time series analysis, which requires coregistering lots of images, the temporal decorrelation and error propagation becomes a critical issue for TOPS coregistration. A few works have been carried out for this topic [31, 32], but more studies and experiments are still desired as the S1 system are collecting more and more images.

1.3 Scope of this Research

This thesis focuses on a complete interferometric processing flow for the wide swath mode. For accomplishing this goal, the study is carried out in the following aspects:

1. Studying the different approaches of TOPS coregistration. The aim is to evaluate the performance and feasibility for different coregistration approach, and to understand the best approach depending on the processing area. This will increase the robustness of TOPS coregistration for complex scenarios. Specifically, the author proposes to study and understand the conventional cross-correlation method followed by enhanced spectral diversity. The feasibility, correctness and robustness of this coregistration method will be carefully studied;

2. Realizing the S1 TOPS interferometric processing flow. This part will include studying the TOPS related issues in the processing flow and delivering high quality interferometric products out of the flow. Specifically, the author proposes to realize a stripmap-like processing flow so that the S1 processing chain could be integrated into an existing stripmap processing platform. The stripmap-like flow could fully utilize all the functions that are already realized in the stripmap processing platform, meanwhile implementing all the TOPS related process into the platform. For the users who are already very familiar with the stripmap mode, a stripmap-like processing flow would be more user-friendly, in the sense that, the interface and the processing steps and the outcome (SLCs and interferograms) will all be identical to the stripmap case, and all TOPS related processes will be implemented under the hood;

3. At last, it is proposed to use the same interferometric processing flow for the other wide swath mode, the ScanSAR mode. The aim is to develop a common wide swath processing chain that could be used for both TOPS and ScanSAR mode.

The three aspects are closely related to each other. The theories, methodologies and processing steps all serve for the purpose of studying and realizing the interferometric processing of the wide swath mode. Realizing the processing flow is for the purpose of working with applications such as civil engineering projects and earth observation missions. Throughout the thesis, for application purpose, a number of interferogram examples are demonstrated in each chapter for validating the applicability of the proposed study. A complete case study is also presented in the last chapter to emphasize the powerfulness of S1 TOPS in monitoring large studying sites.

The chapters are organized in the natural order of the wide swath interferometric processing flow. Chapter two introduces the basics, mainly the TOPS working mode and the azimuth impulse response function. All the theories, methodologies and processing flows are based on this chapter. Chapter three studies the most important step in TOPS interferometry, the coregistration. Two different coregistration approaches are carefully studied and evaluated. Chapter four proposes the workflow for processing the TOPS mode from importing SLC to doing interferometry. Chapter five extends the same processing flow to the other wide swath mode, the ScanSAR mode. Chapter six presents a ground monitoring application in the California Central Valley with the proposed TOPS interferometric processing flow. Chapter seven is the summary of this study.

2. TOPS MODE INTRODUCTION

2.1 Introduction

The TOPS mode is different from the stripmap mode in many aspects. Some main topics with TOPS include the burst mode nature of TOPS, the deramping & reramping process and the strict coregistration requirement. However, all these issues essentially come down to how the image is acquired and what is the signal representation in the TOPS system. This will be discussed in this chapter. The TOPS burst nature and acquisition mode will be introduced in the first place; followed by the impulse response function (IRF). Then some other factors that affect the interferometric product quality such as burst synchronization and doppler centroid will be discussed. The discussion in this section prepares all the necessary theory for the coming chapters where the implementation of processing flow will be discussed.

2.2 Bursts Nature of Sentinel TOPS

Sentinel-1 could operate in four different modes: stripmap (SM), interferometric wide swath (IW), extra wide swath (EW) and wave mode (WV). Out of all four working modes, WV is mainly used over open ocean area. IW mode is the default working mode over land area. EW mode is mainly for sea-ice, polar zones and certain maritime areas including ice, oil spill monitoring and security services. SM mode is only used for small islands plus a few routine sites for calibration purpose. The way IW and EW work is called Terrain Observation Progressive Scan, or TOPS. The main difference between IW and EW is that IW scans three subswaths and EW scans five subswaths. In the following contexts, I will use the term TOPS, Wide Swath, or IW interchangeably unless otherwise indicated.

An illustration of TOPS burst mode with two subswaths is shown in figure 2.1(b). The satellite starts with the first subswath. By electronically steering the antenna back-to-forth along the azimuth direction, the scan covers a longer area in the same scanning duration of stripmap mode (figure 2.1(a)). In TOPS mode the steering angle usually goes from $-0.6°$ to $0.6°$ in the azimuth direction. A complete antenna steering back-to-forth is called a burst. Inside one burst the image is continuous (means the sampling grid is even). After scanning one burst in the first subswath, the antenna switches to the next subswath by adjusting the incidence angle. Upon completion, in a two-subswath system, the system will then switch back to the first subswath and scan the next burst. To make sure the final image (after stitching) is continuous and do not have any gaps, the consecutive bursts from the same subswath will have a small overlapping area. This means that every target inside the overlapping area is scanned twice from different squint angles. This overlapping area is critical for the coregistration purpose. The typical overlap is around 120 valid lines (around 2 km on the ground). TOPS burst mode trades resolution in azimuth for broader coverage in range. To scan more subswaths, the time duration for scanning each burst will decrease. Hence the azimuth bandwidth will decrease. This will correspondingly decrease the azimuth resolution.

There are two initiatives in the TOPS mode. The first one is to increase the scanning area. Serving under the ESA's Copernicus program, S1 is designed to be a scientific operational system for large scale monitoring work such as land, natural disasters mapping, etc. For such purpose it is desired to have the capability of scanning larger area all at once. The IW mode can cover up to 250 km in range direction, approximately three times of stripmap mode. The second initiative is to minimize the scalloping effect and serve as an improvement to the ScanSAR mode [10]. The ScanSAR mode also switches between subswaths to increase the scanning area; however its scanning mode [3] will give raise to the scalloping effect. More discussions on ScanSAR will be carried out in chapter 5.

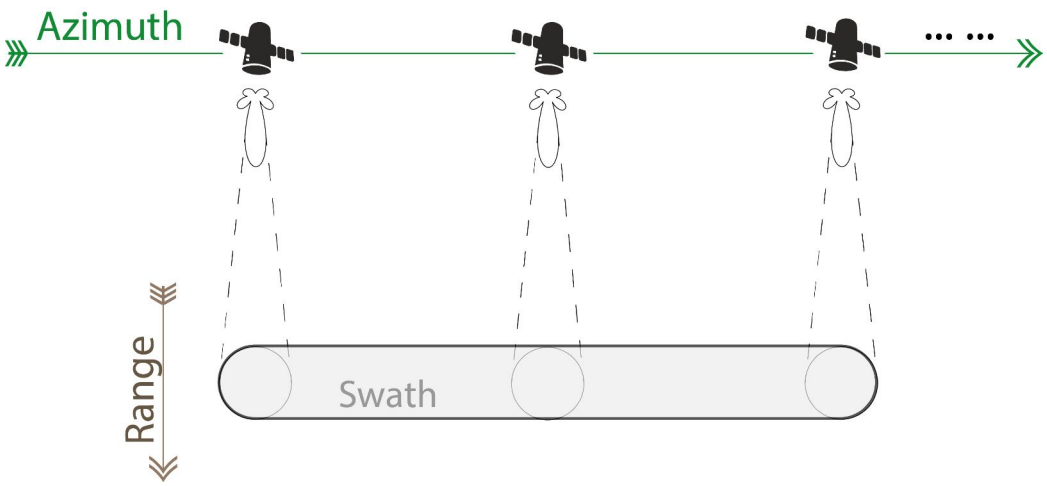

(a) stripmap

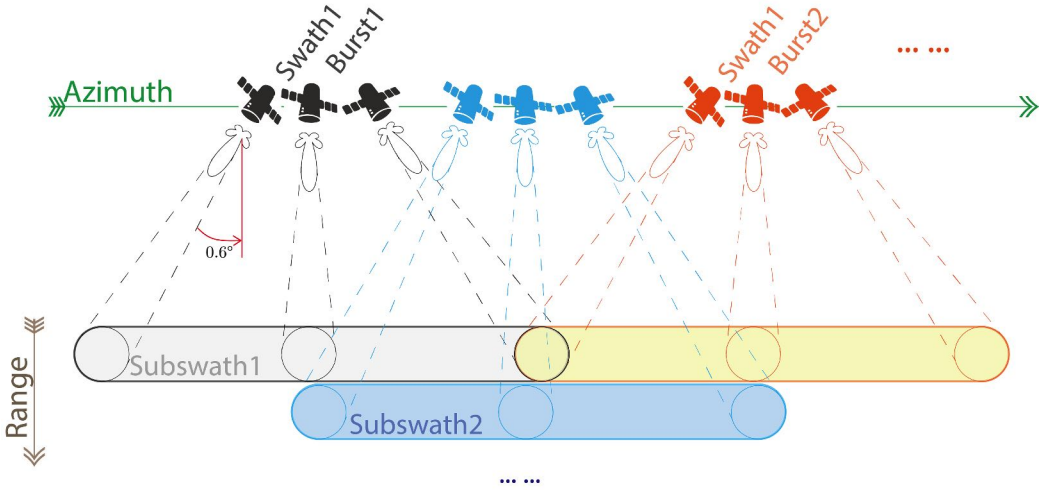

(b) tops

Fig. 2.1. (a): An illustration of stripmap working mode. Stripmap simply works in a "scan-and-receive-line-by-line" mode. (b): A simplification of TOPS working mode with 2 subswath. The antenna sweeps in azimuth direction so that in the same time a bigger area in azimuth could be scanned when comparing with stripmap mode. The antenna then switches to the next subswath by increasing incidence angle. For the same subswath and adjacent bursts, there is always a small portion of overlap to ensure the image could be mosaicked without any gaps.

2.3 TOPS Impulse Response Function

TOPS impulse response function as a function of azimuth time is [33, 34]:

$$\begin{aligned} s(\eta) = s_a(\eta) \cdot \exp\Big\{ -j \cdot \frac{4\pi}{\lambda} \cdot R_0 \Big\} \\ \cdot \exp\big\{ j \cdot 2\pi \cdot f_{\eta_c} \cdot (\eta - \eta_c) \big\} \\ \cdot \exp\big\{ j \cdot \pi \cdot K_t \cdot (\eta - \eta_c)^2 \big\} \end{aligned} \tag{2.1}$$

η is the azimuth zero doppler time; η_c is the beam center crossing time; s_a is the azimuth envelope of compressed target and is typically a sinc$(\cdot)$ function; R_0 is the slant range of closest approach to the target; K_t is the doppler centroid rate in the focused TOPS SLC data; f_{η_c} is the doppler centroid frequency without introducing the steering of the antenna, and could be thought of equivalent to the doppler centroid in the stripmap case. Since TOPS is total zero doppler steered [13], f_{η_c} is very close to zero (a measured 6.2 ± 19.494 Hz for S1).

Here it is worth stating a few notes regarding the IRF of TOPS:

1. This equation is the most important point in this thesis. Everything hereinafter is based on this equation: stitching, deramping, coregistration, etc. This equation is what makes TOPS different from the stripmap mode. However, the equation is really very simple, elegant and the only difference between TOPS and stripmap [35] is the last term in the equation, the quadratic phase term $\exp\{j\pi K_t(\eta - \eta_c)^2\}$. The intuitive understanding of this term is the extra doppler introduced by the steering of the antenna along the azimuth;

2. This extra quadratic phase term is also a legitimate measurement of the slant-range distance to the point target and it provides the real distance for the zero doppler geometry [16]. Therefore, this term need to be preserved and can not be discarded if one wants to do interferometry;

3. This quadratic phase term is azimuth dependent and is responsible for the high coregistration accuracy requirement along azimuth direction. For example, in

the presence of a miscoregistration time of $\Delta\eta$ in the azimuth direction, the interferometric phase error would become $2\pi K_t \eta \Delta\eta$ and varies with azimuth time η. A special coregistration method, enhanced spectral diversity (ESD), is required for perfect spectral alignment. In addition, This quadratic phase term exceeds the PRF. By Nyquist sampling theorem, when the bandwidth exceeds sampling rate (in complex domain), an alias occurs when resampling. To solve this, the quadratic term and baseband term needs to be resampled separately. This is well known as the deramping and reramping process.

For completeness, the IRF as a function of range time τ is also given [36]:

$$\begin{aligned} s(\tau) = s_r(\tau) \cdot \exp\Big\{ -j \cdot \frac{4\pi}{\lambda} \cdot R_0 \Big\} \\ \cdot \exp\big\{ j \cdot 2\pi \cdot f_0 \cdot (\cos\beta - 1) \cdot (\tau - \tau_0) \big\} \end{aligned} \tag{2.2}$$

s_r is the range envelop of the compressed target and is also typically a $\mathrm{sinc}(\cdot)$ function, f_0 is the carrier frequency, τ is range time, τ_0 is the reference range position of the impulse response, and β is the squint angle. Due to the presence of squint angle, there is a linear phase term in range direction with slope equal to $f_0(\cos\beta - 1)$. When β is zero this phase ramp disappears; when β is significant, the doppler centroid varies in the range direction. In the case of TOPS, the range phase ramp is very small due to the small squint angle in TOPS ($\pm 0.6°$) and could be neglected [16] in general. In later sections, it will be shown that a miscoregistration in range direction due to the squint angle β together with a strong topology will add a small interferometric phase bias. In most cases, the IRF in range direction for TOPS could be treated as the same as the stripmap case. Thus in the following discussions the focus will mainly be on the azimuth IRF unless otherwise stated.

2.4 TOPS Burst Synchronization

Burst Synchronization, azimuth spectral shift, azimuth spectral alignment and azimuth common bandwidth all refers to the same thing, and they are essentially

equivalent to the range spectral shift [37]. In the range direction, the spectral shift is mainly due to the local topography (slope). Other terminologies that also refer to the range spectral shift include range spectral decorrelation and geometrical decorrelation. The baseline value that causes a total decorrelation (or, no range common bandwidth) is referred to as the critical baseline. In the azimuth direction, however, the spectral shift due to topography is quite small and could be ignored [38]. The main contribution to the azimuth spectral shift is the squint angle and the doppler centroid [9]. However the idea of the common bandwidth and spectral decorrelation could be shared for both range and azimuth direction.

The essence of the common bandwidth is stated in [26, 37, 39]. In the azimuth direction, the wide swath mode poses a more strict requirement on the burst synchronization than the stripmap mode. This is because the wide swath mode usually has a narrower azimuth bandwidth, which means that the same amount of spectral shift will end up in a smaller percentage of the common bandwidth. For the TOPS mode, the bursts in the master and slave images must be "synchronized" in terms of the squint angle and the doppler centroid at any moment. Burst synchronization determines the coherence of interferometric product. When the burst synchronization is not ideal and common bandwidth is low, the common bandwidth filter is required for filtering out the noise and increasing interferometric coherence.

In the TOPS system, there are two factors affecting the burst spectral alignment in the azimuth: the doppler centroid and the timing. Looking back at equation 2.1, the variables that could cause a burst misalignment are f_{η_c}, K_t and $\eta - \eta_c$. A different doppler centroid (either cause by a different doppler centroid value f_{η_c} and K_t, or a different steering angle due to antenna mis-pointing) will shift the azimuth spectrum and decorrelate the interferogram. On the other hand, a shift in time by $\Delta\eta$, either caused by miscoregistration or burst timing mis-synchronization, could also decorrelate the interferogram. It has been demonstrated in [40] that the TOPS system is more robust to burst spectral alignment in both cases addressed above when comparing with the ScanSAR mode. When it comes to a different doppler centroid,

one could perform a common bandwidth filtering; when it comes to a slight timing mis-synchronization, the enhanced spectral diversity method could be used to correct this timing error.

In general, TOPS has quite an ideal burst synchronization. After the commissioning phase of S1A and S1B, their doppler centroid frequency f_{η_c} are all located quite precisely around zero [13, 41]. A number of efforts were also made to control the burst timing and minimize the timing error, such as timing calibration [13], using on-board schedule execution based on orbit position angle [40] and tightening the orbital tube [42]. It has been reported that the majority of interferometric pairs from both S1A and S1B shares a common bandwidth of greater than 90% [40, 41]. The excellent performance for S1 system in burst synchronization and antenna steering indicates that the azimuth common band filtering could be skipped without having a significant coherence drop [9, 28].

2.5 Summary

This chapter introduced the burst mode of TOPS. The most important thing is the IRF function in the azimuth direction, where the quadratic phase term introduces an azimuth dependent doppler centroid term. This term is the result of the antenna steering in the azimuth direction. This term is responsible for all the processing techniques and methodologies required by TOPS. Then the issue of burst synchronization and azimuth common bandwidth is mentioned. Because of the excellent system control, the common bandwidth after commissioning phase would be greater than 90% for most of the time and the band filtering step could be skipped. The residual timing error could be corrected in the coregistration step. Overall TOPS is an excellent system with superb performance in all aspects for interferometric purpose.

3. COREGISTRATION OF TOPS

3.1 Introduction

This chapter discusses the coregistration of TOPS SLC images. Coregistration is one of the important steps in InSAR. Coregistration means that the SLC images must be "aligned" well so that the they could be compared pixel-wise for differences, where the differences reveal ground information such as height or movement. The miscoregistration will cause coherence loss in the interferogram for stripmap mode [43]. Common stripmap product requires a coregistration accuracy of around 0.1 pixel to avoid non-negligible decorrelation [43]. However, coregistration for TOPS mode has a much stricter requirement than stripmap. In TOPS mode, the sweeping of antenna introduces a quadratic doppler frequency in azimuth that exceeds the PRF. For "aligning" this high-frequency quadratic phase term, a very high coregistration accuracy is required. A miscoregistration will not only cause decorrelation, but will also introduce a phase bias [16] into the interferometric product. To avoid introducing non-negligible phase error (usually 0.05 radians) into the interferogram, a coregistration accuracy of 0.001 pixel is required. For such reasons, it is important to exploit the suitable coregistration methods for TOPS that meets the 0.001 pixel accuracy requirement.

There are mainly three ways of doing coregistration: cross-correlation-and-rigid-transformation (**from now on referred to as "cross-correlation method"**) [37], geometrical approach [29] and (enhanced) spectral diversity [14,44]. Cross-correlation method firstly estimates shifts between master and slave image at different locations. Then a rigid transformation is performed for slave image based on the estimated shifts (or sometimes a non-linear transformation, but the discussion throughout this study will be limited to rigid transformation due to the small orbit crossing angle of TOPS.

This will also be discussed in section 3.2.1). Then, in recent years, with the improving quality of satellite orbital state vectors, the geometrical approach is brought to the table. This approach could be seen as a mapping from SAR coordinates to Cartesian coordinates with the help of very precise orbits and DEM. The coregistration accuracy for this approach mainly depends on the accuracy of orbital state vectors (it also depends on the topography, e.g., an available SRTM; but due to the very small orbital crossing angle of S1, the impact of topography to the final coregistration accuracy is very small and SRTM is already good enough for that [14, 42]. Details will be given in section 3.2.2). With the availability of precise orbital state vectors for S1 with an accuracy of 5 cm [45], this approach is accepted by the current SAR community as the initial coregistration method. Meanwhile, neither of the two aforementioned methods could guarantee to reach the required 0.001 pixel coregistration accuracy in azimuth direction for TOPS [9]. Thus, after the initial coregistration, the enhanced spectral diversity method [14, 44] will be applied to correct the residual coregistration error and achieve the coregistration requirement for TOPS. ESD has been proved to be quite robust in most of the stationary scenes [9].

ESD compares the phase differences of two images. The azimuth miscoregistration is derived from this differential phase. Since ESD operates on phase, one should always note the wrapped nature of phase. This means that an as-precise-as-possible initial coregistration should be performed so that the differential phase in ESD step is limited to $[-\pi, \pi)$. Later into the chapter it will be shown that the $[-\pi, \pi)$ in ESD is equivalent to a 0.05 pixel accuracy for avoiding phase ambiguity. The current trend for TOPS is the geometrical coregistration followed by ESD (**from now on referred to as "established approach"**) when the precise orbits are available. On the other side, the cross-correlation method followed by ESD (**from now on referred to as "proposed approach"**) is rarely studied and discussed for S1 TOPS case. It is desired to explore the feasibility of using the proposed approach, to understand if there are some special processing steps related to the proposed approach, and to determine if and when the proposed approach could be used as an alternative to the

established approach with a negligible discrepancy. In fact, the features of S1 system, such as the small temporal baseline (6 days for S1A-S1B or 12 days for S1A-S1A and S1B-S1B), small spatial baseline (120∼200 meters tube [13]) and small orbital crossing angle ($< 0.001^\circ$ [42]), are all in favor of the cross-correlation method, as the quality of cross-correlation and estimation depends on good coherence and all the merits of S1 significantly reduce the temporal and geometrical decorrelation.

For a comprehensive understanding of the proposed approach, the study is carried out in two aspects: (1) to understand the coregistration accuracy of the cross-correlation method; and (2) to evaluate if the proposed approach (cross-correlation method followed by the ESD) could give identical interferogram with the established approach.

Specifically, for evaluating the theoretical coregistration accuracy of the cross-correlation method, the Cramér-Rao lower bound (CRLB) is used for showing the lower bound on the coregistration accuracy. For validating the accuracy of the cross-correlation method, one could read the coregistration residual from the cross-interferogram phase in the ESD step. For verifying the correctness of the proposed approach with respect to the established approach, one could compare the interferograms from the two approaches, and check if there is a non-negligible phase.

This chapter is organized in accordance with the two aspects that are proposed for studying. The second section discusses the theoretical coregistration accuracy of the two methods, the cross-correlation method and the geometrical method, using the idea of CRLB. The third section briefly describes the ESD method. The fourth section experiments on real data for a variety of different cases. There are two purposes for running experiments. The first one is to validate the coregistration accuracy of the cross-correlation method by looking at the cross-interferogram. The second purpose is to check for interferogram phase difference between the proposed approach and the established approach. The last sections discuss a few points regarding the proposed approach, focusing on some issues related to the cross-correlation method, such as the topography, the orbital crossing angle and temporal baseline.

3.2 The Coregistration Accuracy of Cross-correlation Method and Geometrical Method

3.2.1 Cross-Correlation & Rigid-Transformation

The problem of coregistration is very similar to the time delay estimation (TDE) problem in signal processing [46, 47]. In sequence, the cross-correlation method does the following:

1. Performs the cross-correlation between master and slave image using small windows at different locations;
2. Performs the maximum likelihood estimation (MLE) on the cross-correlation between master and slave windows to estimate the offsets;
3. Estimates the transformation matrix for the slave image based on the calculated offsets at different locations;
4. Perform the rigid transformation based on the estimated transformation matrix.

In the steps above, two estimations are performed. In the first place, one estimates the offsets for small windows between master and slave at different locations. In the second place one estimates the transformation matrix. The two estimations accuracy will be discussed separately.

The Accuracy of Estimating Offsets A number of patches distributed uniformly on master and slave images are selected for estimating the offsets. A patch is usually a small square window of the size n (for example, 8×8, or 64×64). When $n = 1$ the patch is a point. For each patch, the offset will be estimated with MLE after

cross-correlation. Now once can express this process in a mathematical way. Suppose there is a mutual shift between the master and slave patch, denoted as the following:

$$u_1[n] = s[n] + w_1[n], \tag{3.1}$$

$$u_2[n] = \alpha s[n - \Delta n] + w_2[n], \qquad n = 1, ..., N \tag{3.2}$$

$$\gamma = \frac{E[u_1 u_2^*]}{\sqrt{E[|u_1|^2]\, E[|u_2|^2]}} \tag{3.3}$$

where $u_1[n]$ is the master signal, $u_2[n]$ is the slave signal with offset Δn, $*$ is the conjugation operator, $s[n]$ is the signal, $w[n]$ is the speckle noise in SAR imagery, α is the amplitude gain; γ is the coherence which is also related to the signal clutter ratio (SCR), N is the size of the patch. Δn is the mutual shift for this patch that needs to be estimated. Note that in general u_1 and u_2 are complex signals and the cross-correlation is carried out in the complex domain [48]. In several literatures $w[n]$ is assumed as the complex, zero mean stationary white noise, and then $u_i[n]$ is referred as the stationary circular Gaussian process [29, 49, 50]. In the following discussion, the analysis is carried out for the 1D signals as in equation 3.1 and 3.2 but the conclusions could also be expanded to the 2D case.

The MLE of the cross-correlation between u_1 and u_2 gives an estimated mutual shift value denoted as $\Delta\hat{n}$. The CRLB of $\Delta\hat{n}$ is [49, 51]:

$$\sigma_{\Delta\hat{n}} = \sqrt{\frac{3}{2N}} \frac{\sqrt{1 - \gamma^2}}{\pi\gamma} \tag{3.4}$$

The reason for using the CRLB is because the MLE is asymptotically unbiased and efficient. Here, the CRLB could also be expressed as a function of SCR. Here it is assumed that the master and slave patches have close enough SCR, where the SCR is defined as:

$$\text{SCR} = \frac{\sigma_s^2}{\sigma_w^2} \tag{3.5}$$

σ_s^2 and σ_w^2 are the variances of signal and noise in equation 3.1 and 3.2. Then, by the definition of coherence in equation 3.3, and suppose that $w_i[n]$ are uncorrelated

zero mean complex Gaussian noise [49, 50], and that $s[n]$ and $w[n]$ are also uncorrelated, then, by the definition of coherence, one would have the following [52, 53]:

$$\gamma = \frac{\sigma_s^2}{\sigma_s^2 + \sigma_w^2} = \frac{1}{1 + 1/\mathrm{SCR}} \tag{3.6}$$

Then equation 3.4 becomes

$$\sigma_{\Delta\hat{n}} = \sqrt{\frac{3}{2N}} \frac{\sqrt{1 + 2\mathrm{SCR}}}{\pi\ \mathrm{SCR}} \tag{3.7}$$

When the estimation use strong point scatterers (characterized by sufficiently high SCR values), the lower bound become [48, 54]:

$$\sigma_{\Delta\hat{n},point} = \frac{\sqrt{3}}{\pi} \sqrt{\frac{1}{\mathrm{SCR}}} \tag{3.8}$$

Comparing with equation 3.7, the $\sqrt{N}$ in the denominator is not there due to the central limit theorem. For strong point scatterers, SCR $\gg 1$, so that $\sqrt{1 + 2\mathrm{SCR}}/\mathrm{SCR} \approx \sqrt{2} \cdot \sqrt{1/\mathrm{SCR}}$.

It can be seen from both equation 3.4 and 3.8 that, the key factor for estimation accuracy is the coherence/SCR. For getting a higher accuracy in estimating the offsets, patches with higher SCR should be prioritized. The size of the patch is also important; however, it follows the reciprocal of square root, which means when N is large enough then increasing the patch size won't decrease CRLB significantly.

The Accuracy of Estimating Transformation Matrix Now let's evaluate the accuracy for the rigid transformation step. Suppose now the offsets for a number of points (or patches) have been calculated and denoted as $\Delta\hat{n}_1, ..., \Delta\hat{n}_m$. At this point, one could use again the MLE to estimate the coefficients of the rigid transformation for the slave image. The 2D slave image in vector form is $\mathbf{S_{2\times M}}$ where M is the number of points to be transformed; the linear transformation matrix is $\mathbf{D_{2\times 2}}$; the translation matrix is $\mathbf{t_{2\times 1}}$, the resampled slave image is $\tilde{\mathbf{S}}_{\mathbf{2\times M}}$, then the rigid transform is expressed in the following way:

$$\tilde{\mathbf{S}}_{\mathbf{2\times M}} = \mathbf{D_{2\times 2}} \cdot \mathbf{S_{2\times M}} + \mathbf{t_{2\times 1}} \otimes \mathbf{1_{2\times M}} \tag{3.9}$$

where $\tilde{\mathbf{S}}_{\mathbf{2\times M}}$ is the resampled slave image. $\otimes$ is the Kronecker product, $\mathbf{1}_{\mathbf{2\times M}}$ is a vector with all ones. A different way of writing the transformation function without using vectors is given in [37]. Equation 3.9 will have the following effects to the resampled slave image [37]:

1. The Kronecker product term represents a mutual shift (on azimuth and range) between master and slave image. In InSAR, this shift is mainly due to orbital timing error (azimuth) and perpendicular baseline component (range);

2. The transformation matrix $\mathbf{D}_{\mathbf{2\times 2}}$ could include a stretch in range and a rotation that skews both azimuth and range.

For understanding the accuracy of the rigid transformation, the focus is on the accuracy regarding the mutual shift and the rotation. The two cases could be representative for SAR image coregistration and are enough for understanding the rigid transformation accuracy in terms of CRLB. Detail regarding a more general case could be found in [55].

For the case of a mutual shift between master and slave image, suppose there are M points/patches used for the estimation, each has an estimated offset with variance $\sigma^2_{\Delta\hat{n}}$. Since the M points/patches do not overlap, it is safe to assume that they are independent, and thus the estimated offsets $\Delta\hat{n}_i$ are mutually independent. The CRLB for estimating the mutual shift is thus given by [55]:

$$\sigma_{\tilde{\mathbf{S}},\text{shift}} = \frac{1}{\sqrt{M}}\,\sigma_{\Delta\hat{n}} \tag{3.10}$$

It can be seen from equation 3.10 that the lower bound is independent of the locations of the points. Also equation 3.10 applies to both range and azimuth direction.

Now let's evaluate the CRLB for estimating the rotation matrix. Although in SAR coregistration, the rotation angle is very small [37], later it will be shown that it does have non-negligible effects on TOPS coregistration. With the assumption that

the variance for each point on the range and azimuth directions are the same, the following simplified CRLB could be derived [56]:

$$\sigma_{\tilde{\mathbf{S}},\text{rot}} = \frac{1}{\sqrt{\sum_{i=1}^{M}(s_{ix}^2 + s_{iy}^2)}}\,\sigma_{\Delta\hat{n}} \tag{3.11}$$

where s_{ix} and s_{iy} are the coordinates for the i^{th} point in $\mathbf{S_{2\times M}}$. Note that by default the rotation matrix rotates the image by an angle α about the origin of the coordinate system. If the variances are different on the two dimensions, CRLB will dependent on the rotation angle α [55]. Unlike the mutual shift case, rotation estimate depends on the location of points. When s_{ix} and s_{iy} are larger, CRLB is smaller. The intuition is that points further from the rotation center will affect more in rotation estimation. For coregistration purpose, this requires points taken from the image to be as uniformly distributed as possible so that the estimated rotation matrix can be more precise.

Conclusion on Cross-correlation & Resampling In conclusion, the cross-correlation-and-rigid-transformation coregistration method mainly depends on three factors: coherence, number of patches, and the location of patches. The first two factors play more important roles in the process. In the first place, it is desired to select patches/points with coherence/SCR as large as possible. Then it is desired to select a sufficient number of patches, M. However, since the standard deviation is proportional to the inverse square root of M, at one certain point the increase of M will play a less important role to the final accuracy determination.

3.2.2 The Geometrical Method

Another widely-applied coregistration method is the geometrical coregistration [29]. The basic idea of geometrical coregistration is stated here. With the help of state vectors and external DEM, each pixel (in azimuth and range coordinate) on master and slave image could be mapped to the Cartesian reference system. One could consequentially calculate the range and azimuth shift based on the Cartesian

coordinates offsets. There are two advantages of this method. In the first place, while the accuracy of cross-correlation depends largely on the availability of coherent patches, geometrical coregistration does not depend on coherence at all. In the second place, in this approach, the relative coregistration pixel-to-pixel is very accurate, and the topography is being properly considered. The only residual error between master and slave after geometrical coregistration is a constant shift in range and azimuth that comes mainly from the orbit error [14]. This error depends on the orbit accuracy and should be estimated and removed with ESD or conventional cross-correlation. In addition, the accuracy of this method also depends on DEM (e.g., SRTM), but the effect of DEM is only important when the orbital crossing angle is large [42].

The pixel offset for one point target between master and slave image in azimuth is given in the following form [29]:

$$\Delta j = \left(\frac{\Delta^{(\mathrm{az})}}{\Delta_s^{(\mathrm{az})}} \mathbf{v_s} - \mathbf{v} \right) \cdot \frac{\mathbf{P}}{\Delta^{(\mathrm{az})}} + \mathbf{v} \cdot \frac{\mathbf{S_{az}}}{\Delta^{(\mathrm{az})}} \tag{3.12}$$

where Δj is the azimuth offset (in pixel) between master and slave, $\Delta^{(\mathrm{az})}$ and $\Delta_s^{(\mathrm{az})}$ are the azimuth sampling spacing (in meters) for master and slave; $\mathbf{v}$ and $\mathbf{v_s}$ are the velocity unit vectors for master and slave; $\mathbf{P}$ is the coordinate of ground point (in Cartesian system), $\mathbf{S_{az}}$ is the orbital along track offset between master and slave. It can be shown from equation 3.12 that the azimuth offset Δj is determined by two parts: the first term in the equation is related to the ground coordinates $\mathbf{P}$, or in other words, the external DEM. The second term in the equation, $\mathbf{S_{az}}$, is derived from the orbital state vectors.

In the first term of equation 3.12, $\alpha \mathbf{v_s} - \mathbf{v_s}$ is the orbital crossing angle. For the same ground target, the larger the crossing angle, the larger the azimuth offset. However, the orbital crossing angle is usually very small for TOPS (0.001° in the worst case [42]). To achieve a 0.001 pixel accuracy on the azimuth direction, DEM with accuracy less than 250m is good enough, which means SRTM is sufficiently

accurate [42]. Thus the accuracy of azimuth offset is mainly based on the second term. If one takes derivative in the second term to $\mathbf{S_{az}}$ for equation 3.12:

$$\delta(\Delta j) = \frac{\delta \mathbf{S}_{\text{az}}}{\Delta^{(\text{az})}} \tag{3.13}$$

where $\delta \mathbf{S}_{\text{az}}$ is the orbital offset error along azimuth direction, and $\delta(\Delta j)$ is the azimuth offset error (or, the azimuth coregistration error) in pixel. It is worth noting that in [29] the author conducted a sensitivity analysis by considering state vectors deterministic value and taking derivative of equation 3.12 with respect to $\mathbf{S}_{\text{az}}$. On the other side, one could also consider $\mathbf{S}_{\text{az}}$ a random variable and derive the uncertainty of Δj (as a matter of fact, some people [57] treats the orbital as a random variable). The same conclusion could be derived.

The accuracy of precise orbit along azimuth direction is usually within 5cm and restitute orbit along track accuracy is usually within 10cm [45]. Equation 3.13 says that 5cm along track baseline error leads to an azimuth coregistration accuracy of around 0.004 pixel (the azimuth sampling spacing for TOPS is around 13$\sim$14 meters). To achieve the same goal with strong & isolated point targets, one would need around 2,000 points with SCR 10dB. This shows the advantage of geometrical distribution: the accuracy does not depend on neither the spatial distribution nor the SCR of ground features. In addition, in a number of real-data cases, the along-track baseline error of precise orbits is within 1.5cm [45], corresponds to 0.0012 pixel, which meets the coregistration requirement of TOPS. In [58] the author claims that the geometrical coregistration is enough for most cases of TOPS coregistration and that spectral diversity step is largely unnecessary if the orbital precision could be achieved.

Range Dependent Residual Shifts It has been reported that the residual shifts after the geometrical approach in cross interferogram for one burst overlapping area is almost a constant along range direction [30, 31] unless it is a non stationary scene. The approach is then to estimate a single value of mutual shift for each burst. This will also later be validated in the experiments.

3.3 Enhanced Spectral Diversity

Introduction to Enhanced Spectral Diversity Suppose there is a target on the ground with a slight miscoregistration of azimuth time $\Delta\eta$ in the slave image. From equation 2.1, the interferogram will be $\exp\{j\phi_{\text{interf}}\}\exp\{j2\pi K_t\eta\Delta\eta\}$ where $\phi_{\text{interf}} = 4\pi/\lambda\cdot(R_{0,\text{master}} - R_{0,\text{slave}})$. Now there are two unknown variables, ϕ_{interf} and $\Delta\eta$, but only one observation at time η. The equation is underdetermined and $\Delta\eta$ could not be solved.

If there is another observation at time η', then one will have two observations at time η and η'. With two observations and two unknowns, the system is determined and there is a unique solution to the miscoregistration time $\Delta\eta$. If one writes:

$$\text{ifg} = \exp\{j\phi_{\text{interf}}\}\exp\{j2\pi K_t\eta\Delta\eta\} \tag{3.14}$$

$$\text{ifg}' = \exp\{j\phi_{\text{interf}}\}\exp\{j2\pi K_t\eta'\Delta\eta\} \tag{3.15}$$

Then the cross-interferogram [59] (some literatures call this differential interferogram [14]) is:

$$\text{ifg} * \text{ifg}'^{*} = \exp\{j2\pi K_t(\eta - \eta')\Delta\eta\} \tag{3.16}$$

As shown in figure 2.1(b), for the same subswath, there is always a small area that is illuminated in consecutive bursts. This means that the target inside this small area are illuminated twice, at time η and η' separately. One could use pixels inside this "common area" to generate the cross-interferogram and derive the miscoregistration time $\Delta\eta$ using equation 3.16.

1/1000 Coregistration Accuracy The common Doppler Centroid rate K_t of focused TOPS is around 1750Hz/s. Take $(\eta - \eta')$ to be 2.75s, suppose one requires a coregistration accuracy that limits the interferogram bias to 0.05 radians, the maximum allowed miscoregistration time $\Delta\eta$ should be $0.05/(2\pi\times 1750\times 2.75) \approx 1.65\mu s$. Taking azimuth PRF of 486Hz, the miscoregistration time would convert to 0.0008 pixel and round up to 1/1000 pixel. In conclusion, to achieve a coregistration accuracy of 0.05 radians, a 1/1000 pixel coregistration accuracy in azimuth is required.

Phase Ambiguity of ESD In the ESD step, if the cross-interferogram phase is π, it corresponds to approximately $104\mu s$ or 0.05 pixel miscoregistration in azimuth. This means that for avoiding the phase ambiguity, the initial coregistration should achieve at least a 0.05 pixel accuracy. Remember that for the stripmap mode, a convention of 1/8 pixel accuracy is desired [43, 60].

3.4 Evaluation of the Proposed Approach with Test Sites

In this section, the performance of the proposed approach with some test sites under different conditions will be evaluated. The focus will be on two points:

1. The first one is to evaluate the coregistration accuracy of the cross-correlation method by checking the cross-interferogram phase in the ESD step. If the cross-correlation method accuracy is low, then the cross-interferogram phase is away from zero; if the cross-correlation method accuracy is high then the cross interferogram phase is close to zero;

2. The second point is to check the interferogram phase difference between the proposed approach and the established approach, and here the established approach is treated as the "reference result". The aim is to test the correctness and robustness of the proposed approach and to understand the conditions for when the proposed approach could apply.

3.4.1 Introduction to Test Sites

For the experiment, three different test sites are used. In sequence, the three examples are representing an ideal testing case, a generic testing case, and a case with large topography:

1. The first test site is located at the Atacama desert in northern Chile. The Desert is a plateau and is the driest desert in the world. From the InSAR point of view, the site is very coherent. Even interferograms with very long temporal

baselines (for example, a few years) could show very high coherence. The idea is to select an ideal case as the first test;

2. The second site is a more generic one. This is a pair of data taken in the early summer (April & May 2018) that covers Purdue University, the U.S.A. The surroundings of Purdue University is mostly farmlands and countrysides. There are a few towns inside the AOI connected by the highway. This dataset has 24 days temporal baseline and 60 meters spatial baseline. The majority of ground features is distributed scatterers, where the coherence will decrease exponentially in time. Also, later in the discussion section, another case in the California Central Valley is presented that shows a very similar ground feature;

3. The third site is Mt Etna in Italy. Mt Etna represents a case with large topography and a relatively large spatial baseline of 123 m (in the sense of S1). The highest point of Mt Etna can reach more than 3,000 meters where the lowest height is close to the sea level. The aim is to test the performance of the proposed approach when there is large height variation in the scene.

3.4.2 The Atacama Desert: a Long Swath with 17 Bursts

The first example comes from Sentinel-1A track 149, subswath 2 on 2017-Nov-16 and 2017-Nov-28. The AOI is in the Atacama desert in the northern Chile[1]. In the cross-correlation method, 40,295 points with SCR over 7dB are selected for estimating the rigid transformation coefficients. The cross-interferogram after the cross-correlation method and geometrical method are plotted in figure 3.1. Note that only the cross-interferogram at burst overlapping area have a none-zero value. Each burst overlapping area is typically around 100∼120 pixels in azimuth. The

[1]Dataset used for this example:
S1A_IW_SLC__1SDV_20171116T230610_20171116T230637_019296_020B1F_BC1A
S1A_IW_SLC__1SDV_20171116T230635_20171116T230700_019296_020B1F_FC0E
S1A_IW_SLC__1SDV_20171128T230610_20171128T230637_019471_0210A6_4730
S1A_IW_SLC__1SDV_20171128T230635_20171128T230700_019471_0210A6_D735

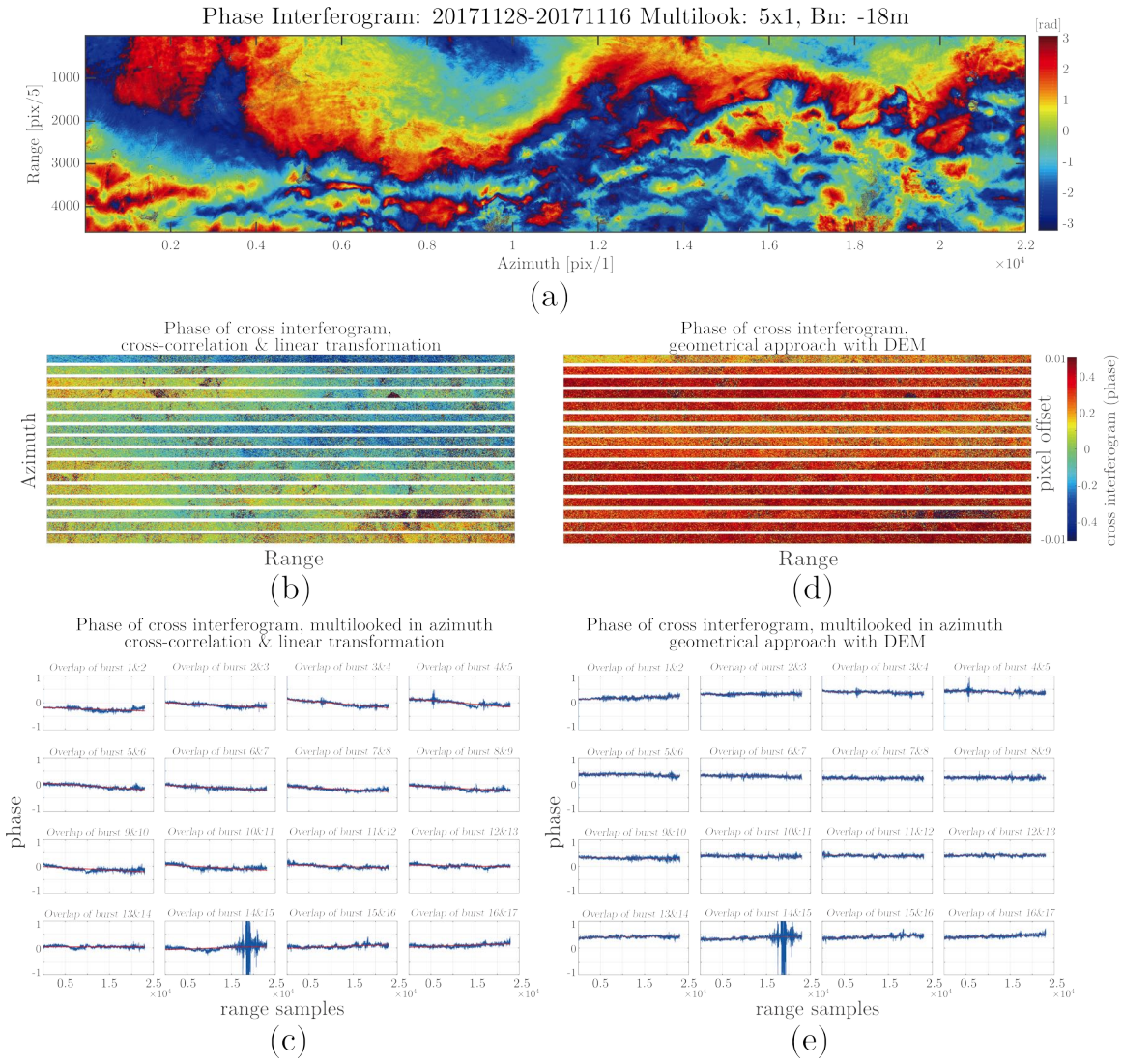

Fig. 3.1. Interferogram of two S1A images on 2017-Nov-16 and 2017-Nov-28 from subswath 2. For each date, 17 bursts are stitched together. (a) the Interferogram, multilooked by 5 in range and no multilook in azimuth, no filter is used; (b) the cross-interferogram at only the burst overlapping area between two consecutive bursts, after the cross-correlation method. The color bar is from 0.5 to -0.5 radians, corresponds approximately from 0.01 to -0.01 pixel miscoregistration; (c) the cross-interferogram at the 16 burst overlapping areas in the 1D plot. The azimuth dimension is multilooked (summed) to get the 1D plot. The x-axis is range and y-axis is the cross-interferogram phase; (d) the cross-interferogram after the geometrical approach; (e) the 1D plot of cross-interferogram at 16 burst overlapping areas after the geometrical approach.

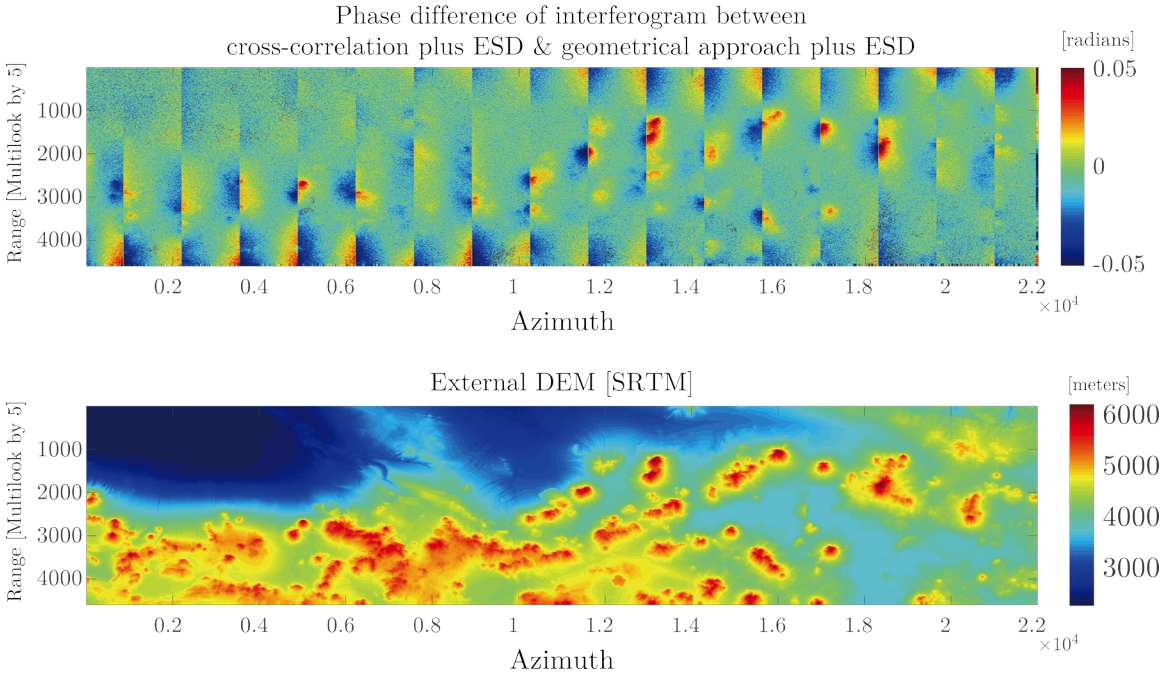

Fig. 3.2. top: the interferogram phase difference between the proposed approach and the established approach; bottom: the DEM from SRTM for this AOI.

cross-interferogram is shown in figure 3.1(b) and (d). In addition, to observe the cross-interferogram phase variation in range direction, I multilooked the 100∼120 pixels in azimuth direction for each burst overlapping area and plot out the cross-interferogram phase as a function of range. The results are shown in figure 3.1(c) and (e) respectively.

In the first place, using equation 3.10, one could calculate that the coregistration accuracy with the cross-correlation method should be approximately 0.001 pixel, or, 0.07 radians in the cross-interferogram. In figure 3.1(b) & (c), the average cross-interferogram phase value is approximately 0.01 radians. This shows that the coregistration residual more or less corresponds to the theoretical value.

In the second place, regardless the initial coregistration method used, the cross-interferogram phases for different bursts overlapping areas are almost the same. This means that even for a very long track (the AOI spans approximately 300 km in az-

imuth) there is only mainly a mutual shift between the master and slave image after the initial coregistration. In fact, it has been shown that the cross-interferogram phase is consistent in azimuth for even much longer datasets [31]. Still, the cross-interferogram phases in different bursts show a very small discrepancy in the magnitude of 0.1 radians. A number of reasons could contribute to such small discrepancy in different bursts. The typical contributing factors could be orbit inaccuracies, timing errors, or geophysical effects [16, 28, 30].

At last, the cross-interferogram phase in the geometrical method does not vary much in range (figure 3.1(e)). This has been reported by others [14, 30, 31] as well. On the other side, the cross-interferogram phase after rigid transformation is sometimes showing a linear trend in the range direction with a noticeable slope (figure 3.1(c)). The reason is a small rotation angle estimation error. More details are in the discussion section.

In figure 3.2 the phase difference between the two interferograms from the proposed approach (cross-correlation followed by ESD) and the established approach (geometrical followed by ESD) is plotted. Overall, the phase difference is within 0.05 radians in most part of AOI, meaning that the difference between two approaches is within the error margin at most parts. Still, it could be seen that the phase difference at some places exceeds the 0.05 radians margin. The places with large phase difference have the following common characteristics:

1. They all have very large height values (comparing with the mean height of the AOI);

2. They are all located at or near the the edges of bursts.

This non-negligible phase difference should mainly come from a miscoregistration in the azimuth direction due to the presence of the crossing angle and the fact that the topography is not considered during cross-correlation method [42]. Another similar case will be presented in the subsection 3.4.5.

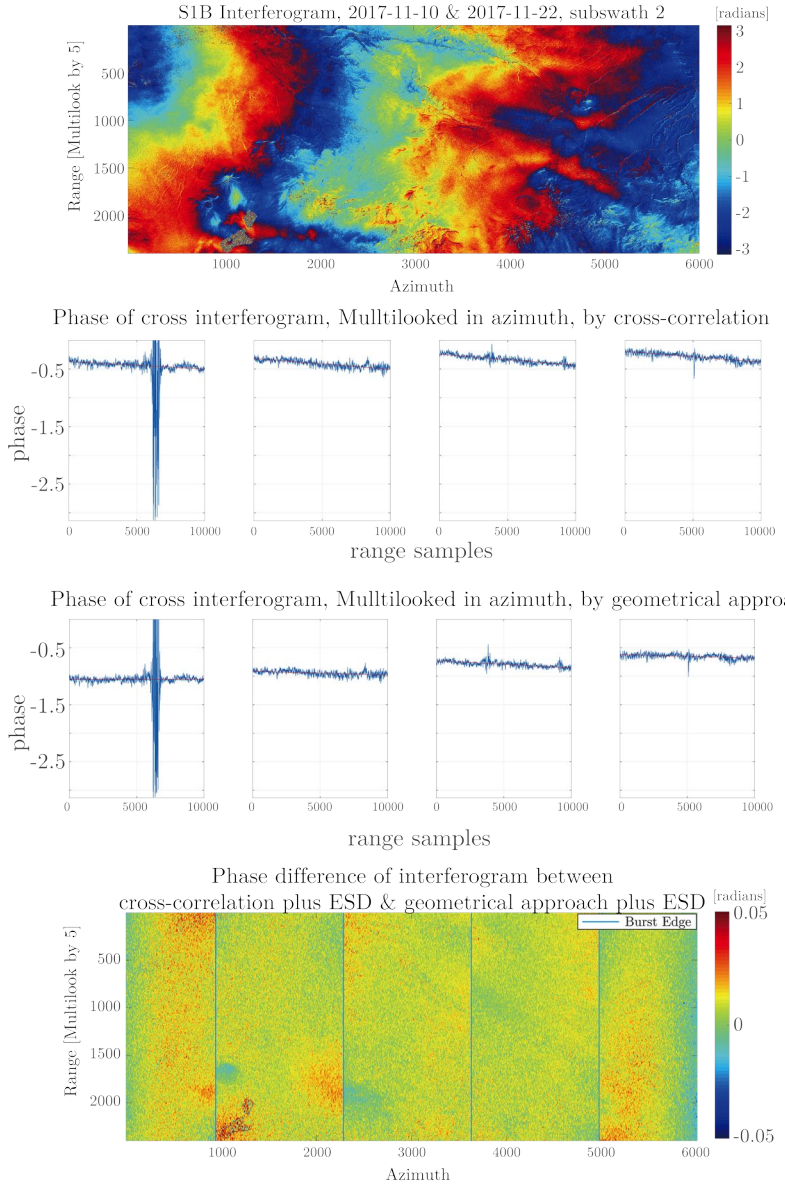

Fig. 3.3. The Interferogram of two S1B images on 2017-Nov-10 and 2017-Nov-12 from subswath 2. First row: the Interferogram, multilooked by 5 in range and no multilook in azimuth, no filter; Second row: the cross-interferogram at burst overlapping area in the 1D plot after the cross-correlation method. Third row: the 1-D cross-interferogram for each burst overlapping area after the geometrical approach; Last row: the interferogram phase difference between the proposed approach and the established approach.

3.4.3 The Atacama Desert: a Short Swath with 4 Bursts

Examples of a smaller area (range 10,000 by azimuth 6,000) is shown in figure 3.3. The two SLCs come from Sentinel-1B track 149, subswath 2 on 2017-Nov-10 and 2017-Nov-22 in the same area [2]. A total of 7,795 points with SCR greater than 7dB are selected for the cross-correlation method. The theoretical coregistration accuracy should be on the scale of 0.15 radians on cross-interferogram. In figure 3.3, the phase read from cross-interferogram is slightly larger than this theoretical value, but they are still more or less at the same level of magnitude. For showing the correctness of the proposed approach, one could see that the phase difference in interferograms is well limited to within -0.02 to 0.02 radians.

3.4.4 Purdue University: an Example with 24 Days Temporal Baseline in April

This example includes two S1A data in April and May with 24 days temporal baseline and 55 m spatial baseline[3]. Subswath 2 covers the entire Purdue University, and the area is typical farmland with scattered small towns (such as the university campus). From the interferogram in figure 3.4, one can see the "blocks" that represent different types of crops. The noisy "blocks" should indicate the fast growth of some types of crops in April; while the coherent "blocks" could indicate no changes over the 24 days period.

The cropped area has 12,000 pixels in range and 5,550 pixels in azimuth. The interferogram is multilooked by 10 $\times$ 2 with no filters applied. 1,229 points with SCR higher than 7dB are selected for estimating the rigid transformation matrix. In theory (equation 3.8 & 3.10), this would correspond to around 0.05 pixel coregistration

[2]Dataset used for this example:
S1B_IW_SLC__1SDV_20171110T230533_20171110T230600_008225_00E8C3_1BA6
S1B_IW_SLC__1SDV_20171122T230533_20171122T230559_008400_00EE11_75CF

[3]Dataset used for this example:
S1A_IW_SLC__1SDV_20180419T234016_20180419T234044_021543_0251FA_381A
S1A_IW_SLC__1SDV_20180501T234017_20180501T234045_021718_02577C_001E

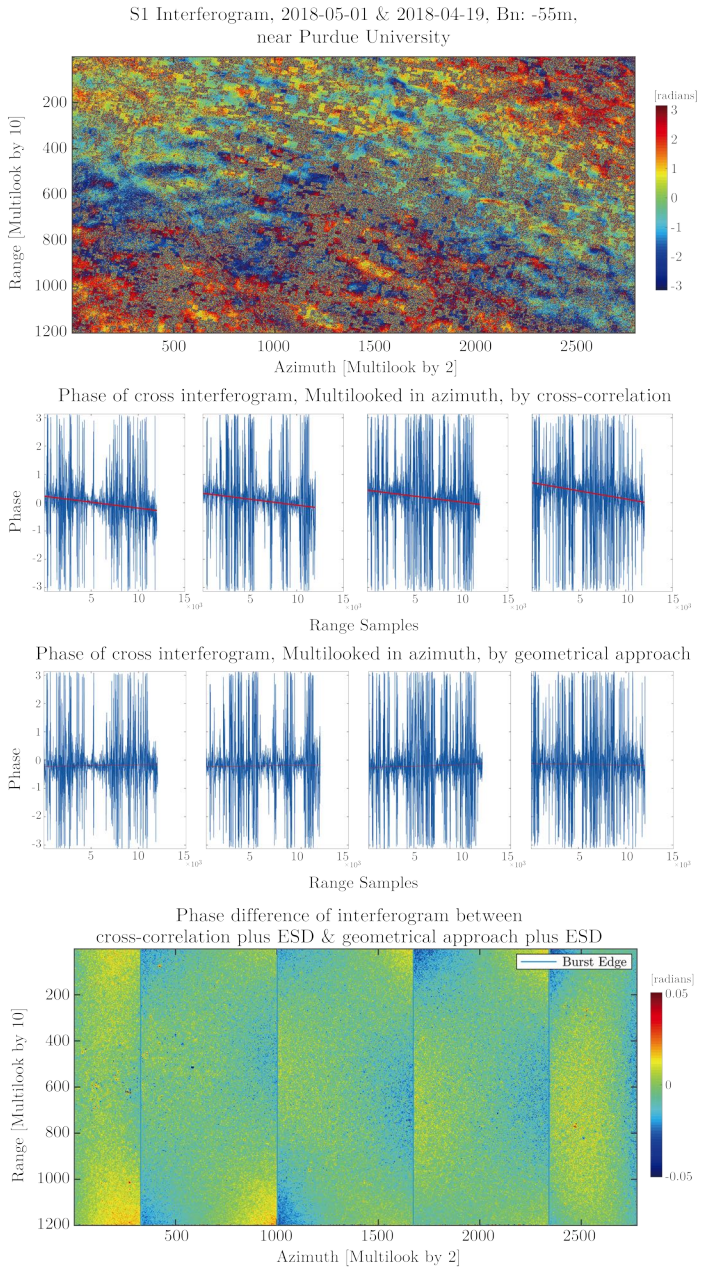

Fig. 3.4. An example with Purdue University as the test site with 24 days baseline. First row: the interferogram mutlilooked by 10×2 with no filter applied; Second row: the cross-interferogram after applying the cross-correlation method; Third row: the cross-interferogram after applying the geometrical method; Last row: the difference of interferogram phase between the proposed approach and the established approach.

accuracy, or around 0.37 radians in the cross-interferogram. The average of the cross-interferogram phase read from the four burst overlaps is 0.42, which is pretty close to the theory.

Comparing with the previous case of the Atacama desert, the cross interferogram of this example looks less coherent due to the temporal decorrelation of distributed scatterers. However, after the cross-correlation method, the linear trend in range for each burst overlap could still be observed and estimated despite the noise. The final interferogram phase between the proposed approach and the established approach shows a very small difference that is limited to within the 0.05 radians error margin. This example shows that the proposed approach could also work well in a more generic case.

In addition, it can be inferred from the examples that the correctness of the final interferogram product from the proposed approach depends on how well one can estimate the phase and slope from the cross-interferogram in the presence of the noise. When interferogram coherence is low, the cross interferogram will be noisier, and the estimation of coregistration residuals from interferogram will be less accurate. This also means that, for a more robust ESD, it is desired to choose image pairs of shorter temporal baseline and hence less temporal decorrelation effect.

3.4.5 Mt Etna: an Example with Large Topography and 123 Meters Spatial Baseline

Mt Etna is an active volcano on the island of Sicily, Italy, and its current height is 3,329 m. The purpose of this testing site is to understand the effect of large topography to the proposed approach. To make this case more general, a relatively large spatial baseline (for Sentinel-1 case) of 123 m is selected. The temporal baseline is 18 days[4]. The cropped area has 19,000 pixels in range and 7,200 pixels in azimuth.

[4]Dataset used for this example:
S1A_IW_SLC__1SDV_20180126T050434_20180126T050501_020321_022B4C_48A0
S1B_IW_SLC__1SDV_20180213T050354_20180213T050428_009600_0114CD_9865

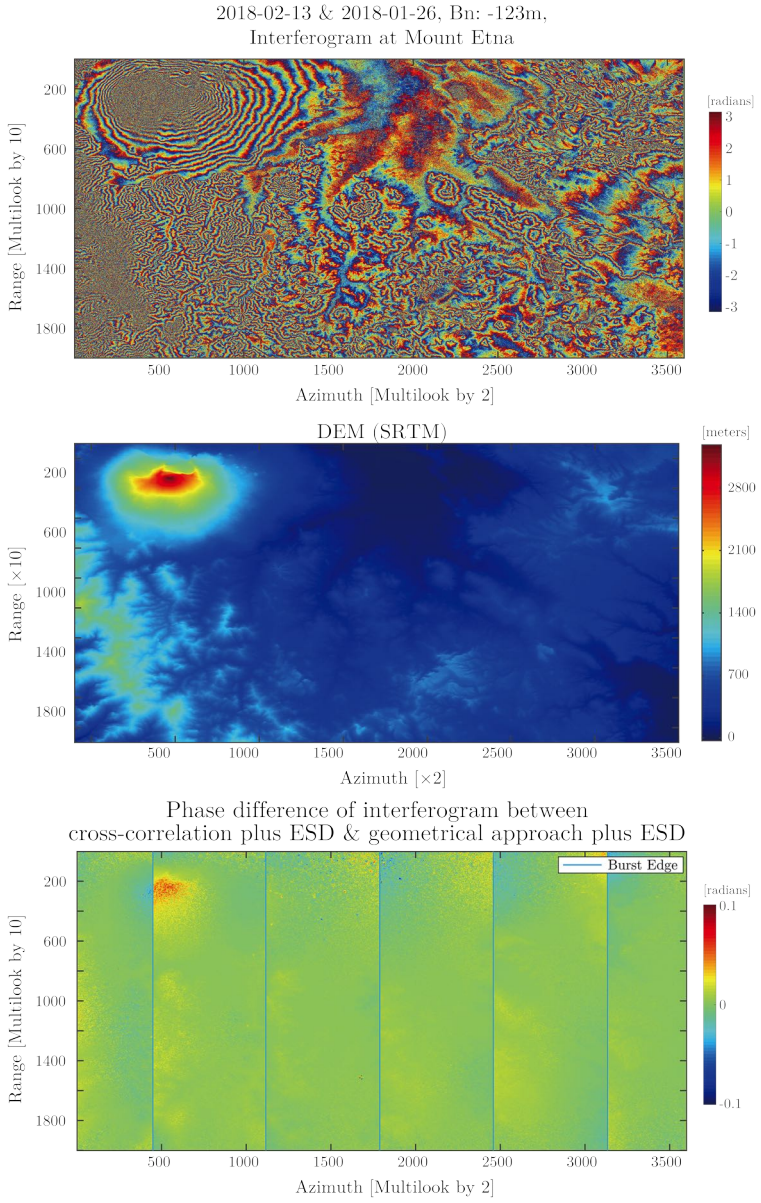

Fig. 3.5. An example with Mt. Etna as the test site with 18 days temporal baseline and 123 meters spatial baseline. First row: the interferogram mutlilooked by 10 × 2 with no filter applied and no topographic phase removed; Second row: the DEM using SRTM; Third row: the difference of interferogram phase between the proposed approach and the established approach. It could be seen that the phase difference is the largest (close to 0.1 radians) at the top of the mountain.

The interferogram is multilooked by 10×2 with no filters applied. To highlight the location of the volcano, the topography phase is not removed from the interferogram. In the rigid transformation, 10,054 points with SCR higher than 7dB are selected for estimating the rigid transformation matrix.

The interferogram phase difference between the proposed approach and the established approach shows a very similar pattern as in the case of the Atacama desert (figure 3.2):

1. (To use the established approach as the reference, then) The interferogram phase error correlates with the topography. The phase error is the largest at the top of the mountain;

2. The interferogram phase correlates with the azimuth position inside the burst. The phase error is the largest at burst edges (because the squint angle is the largest at burst edges) and tends toward zero at the center of the burst (because in zero doppler steering there will be no phase error from miscoregistration).

In this Mt Etna case, the phase discrepancy at the top of the mountain could reach 0.1 radians or more. Similar to the case in section 3.4.2, this phase residual should mainly come from the miscoregistration in the azimuth direction due to the orbital crossing angle and the fact the cross-correlation method fails to consider the topography during coregistration. This effect was well analyzed in [42]. The conclusion is that for cases with very large height variation in the AOI, the proposed approach will introduce a non-negligible phase bias at or near burst edges by failing to consider the DEM during coregistration.

3.5 Further Discussion

3.5.1 Validation: Coregistration Accuracy and AOI Size

ESD could not only coregister the complex number SLC images to the desired level, but could also serve as a tool to check the accuracy of the initial coregistration

method. If the initial coregistration accuracy is low, then the cross interferogram phase will be away from zero; if the initial coregistration accuracy is very high then the cross interferogram phase will be close to zero. In section 3.2.1, it is mentioned that bigger AOI indicates more strong scatterers. More strong scatterers means a better coregistration accuracy, and the relationship between scatterers number and coregistration accuracy follows the law of large numbers. In this section one example is shown to demonstrate this trend.

The same dataset used in section 3.4.3 is used in this example. A small area at the center of subswath 2 is extracted. For validation purpose, 1,500 azimuth lines is selected, and in range direction, I started with 500 range samples, and then double the size to 1,000 and then to 2,000 range samples. For the three small areas, both the cross-correlation and geometrical approach are performed before ESD. The cross interferogram phase at each burst overlapping area is plotted to show the coregistration accuracy of initial coregistration method. It should be anticipated that, for the cross correlation method, the coregistration accuracy increases with the area, and for the geometrical approach, the coregistration accuracy should be independent of the processing area.

The result is shown in figure 3.6. The coregistration accuracy of geometrical approach is shown in the lower part of figure (b), (d) & (f). No significant difference could be observed. The coregistration accuracy of cross-correlation method is showing in the upper part of figure (b), (d) & (f). It could be seen that the coregistration accuracy is the lowest for the smallest area as the phase is furthest from zero with a significant rotation. As the size of area grows large the coregistration accuracy increases and the cross interferogram phase tends towards zero. In addition, the increase of coregistration accuracy when increasing range from 500 to 1,000 is more significant than when increasing from 1,000 to 2,000. Equation 3.10 says this is because the accuracy is proportional to the square root of number of points, or equivalently, the size of area.

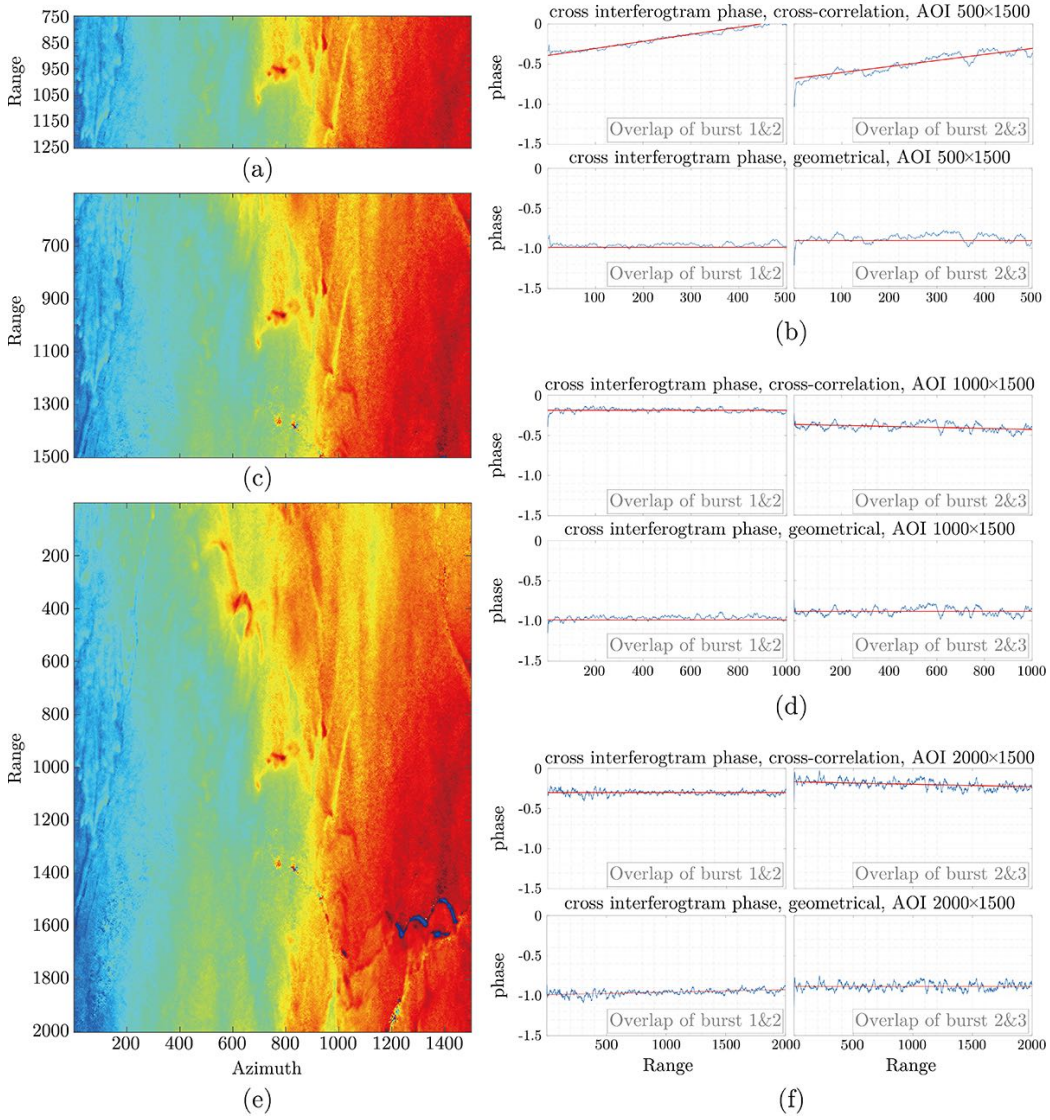

Fig. 3.6. A comparison of initial coregistration accuracy for cross-correlation and geometric approach as the size of AOI grows. The sample dataset comes from the same one as in figure 3.3. All three examples shown here have 1500 lines in azimuth and consists of three bursts. (a) Interferogram of the AOI with size 500 (range) × 1500 (azimuth); (c) Interferogram of AOI with 1000 × 1500; (e) Interferogram of AOI with 2000 × 1500. (b), (d) & (f) are the corresponding cross-interferogram phase at burst overlapping area after cross-correlation approach and geometrical approach.

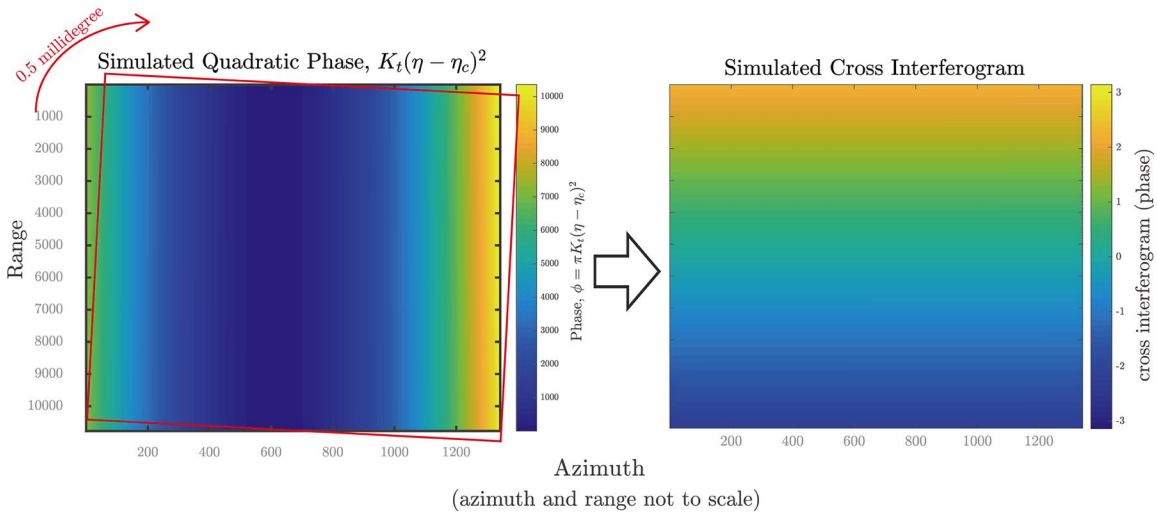

Fig. 3.7. The effect of image rotation on the cross interferogram. A simulated rotation of 0.5 millidegree will be reflected to the cross-interferogram as a linear slope. For a simulated data with 10,770 samples in range, the cross-interferogram phase goes approximately from 2.2 to -2.2 radians.

3.5.2 The Rotation of Slave Image

In all the examples that are shown in the previous section, when using the proposed approach, it can be seen that linear slopes appears in the range direction on the cross-interferogram phase. The linear slope is caused by the residual rotation angle of slave image during the rigid transformation estimation process.

For the purpose of doing interferometry, it is desired to have perfect parallel repeat pass satellite orbits. However, due to the eccentricity of ellipsoid earth, one could never get a perfect parallel between the repeat pass. There will be a very small crossing angle [42]. The crossing angle, albeit small, could introduce some error to the TOPS interferogram. There are mainly three effects for the crossing angle: (1) It will introduce a small amount of burst mis-synchronization and spectrum decorrelation to TOPS [42]. The mis-synchronization could be corrected by the ESD and the decorrelation could be corrected by applying an azimuth common-bandwidth filter (or, since the burst mis-synchronization is usually very small for TOPS, mostly

under 5% [28, 41], one could just ignore the minor coherence loss there); (2) The small crossing-angle post an accuracy requirement to the availability of DEM when performing geometrical coregistration. Though the requirement is quite low, an accuracy of around 300 meters in DEM is still needed to keep the interferometric phase error under 1.5° [42]. (3) The last one is for the cross-correlation method. Since there will be a small rotation between master and slave due to the small crossing angle, the rigid transformation will estimate this rotation angle. The residual between the true rotation angle and the estimated rotation angle will introduce this linear slope in the cross-interferogram.

I start by simulating a small rotation between master and slave image using the real parameters from TOPS. The steps are: (1) read the quadratic phase parameters from a real sample dataset, specifically K_t and $(\eta - \eta_c)^2$ [33]; (2) rotate the quadratic phase by a small angle in the counterclockwise direction around its center point; (3) simulate the two looks from two difference squint angles and generate the cross-interferogram.

The simulation result is shown in figure 3.7. A rotation angle error of 0.5 millidegree corresponds to a linear slope of approximately 4.1×10^{-4} radians/sample. In our example, the phase changes 4.4 radians in range over the 10,770 samples. To correct the rotation error, when performing the ESD one should estimate the range slope and compensate for the rotation angle error. Since the phase could be wrapped, the estimation of the slope could be done with the Fourier transform. Estimating the slope of cross interferogram phase is equivalent to find the peak of shift after Fourier transform:

$$\begin{aligned} x(\tau)\exp\left\{-j2\pi f_{\text{rot}}\tau\right\} &\xrightarrow{\mathcal{F}} X(f - f_{\text{rot}}) \\ \hat{f}_{\text{rot}} &= \arg\max\ X(f - f_{\text{rot}}) \end{aligned} \tag{3.17}$$

where f_{rot} is the desired slope in range for the cross interferogram. The range slope in the cross-interferogram only depends on the residual rotation angle and does

not depend on the mutual shift between master and slave. The bigger the rotation angle, the steeper the slope.

According to [42], at the initial stage of S1 mission the crossing angle reaches 1 millidegree in the worst case. Later on, ESA tightened the cross angle to less than 0.25 millidegree. However, as shown in the simulation, a 0.25 millidegree rotation error could indicate almost a full 2π phase variation along a full burst (usually around 24,000 samples in range). Even a very small estimation error in the rotation angle could be clearly observed on the cross interferogram as a slope in range. In conclusion, it is very necessary to estimate and correct this rotation angle estimation error when using cross-correlation method.

3.5.3 Examples of Correcting Residual Rotation Angle

The first example is shown in figure 3.1. Although the residual rotate angle is small, it could still be observed on the cross interferogram, and the linear trend in range is clear when comparing with the geometrical approach. The linear slope is estimated and removed using equation 3.17.

In examples with long azimuth (2 or more SLCs concacenated together) and cross correlation, taking figure 3.1 as an example, the estimated slope value appears to have a trend of increasing. The estimated slope for each bursts for this particular example is shown in figure 3.8. An increasing trend in the slope could be observed. A bigger slope indicates a bigger rotation angle. Since the bursts are stitched together into a SLC data in the first place, a possible explanation of the increasing slope is the increasing crossing angle in the orbit. Since the linear transformation is performed to the whole SLC image, when there is an increasing crossing angle between master and slave image, one should observe a bigger rotation angle when doing coregistration. An illustration of this phenomenon is illustrated in figure 3.9.

Other examples of correcting residual rotation angle are shown in figure 3.3. A very obvious linear trend in range of the cross interferogram could be observed. After

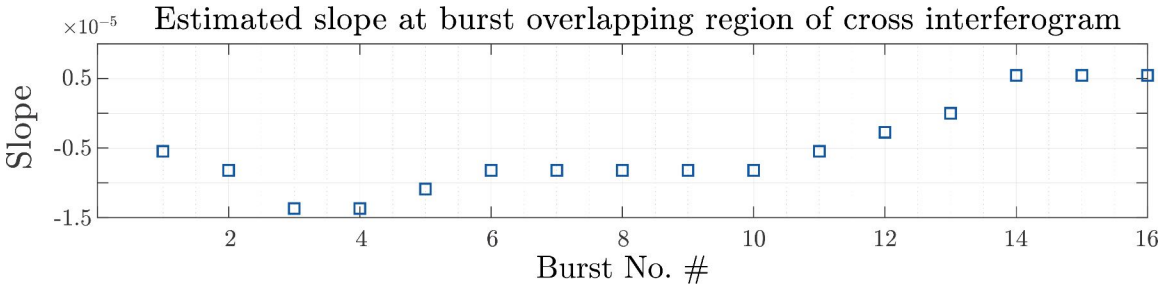

Fig. 3.8. The estimated slope for each burst overlapping area for the data example in figure 3.1.

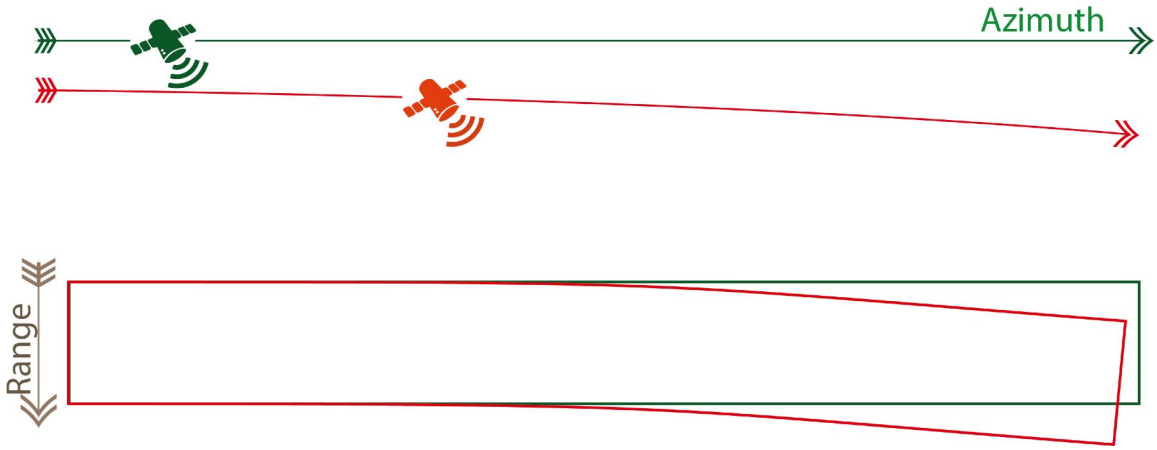

Fig. 3.9. An illustration of increasing crossing angle of orbits for very long tracks.

estimating the linear slope and applying ESD, it could be seen that the interferogram shows negligible difference when comparing with the geometrical approach.

3.5.4 DEM Related Distortions in TOPS Interferogram

This section discusses the impact of DEM in TOPS coregistration and interferometry. DEM/topography could influence the TOPS interferometric process in a number of different ways. In this section, a few error sources when DEM is not available and how will the absence of DEM bias the interferogram are discussed.

The first impact of DEM is related to the crossing angle. As appears in equation 3.12, the accuracy requirement of DEM increase with an increasing crossing angle [29]. Since the crossing angle for S1 is much smaller than the case of ERS or Envisat, the requirement on DEM is not so strict. For example, for a 0.001° crossing angle, one only needs DEM accuracy of around 300 m to fulfill the TOPS coregistration requirement [42]. In general, for flat areas with height deviation smaller than a couple of hundred meters, one could use the earth ellipsoid model instead of SRTM. In our example in figure 3.2 and figure 3.5 with large topography deviation, it is still important to have the SRTM when using the established approach. More details for TOPS case could be found in [15, 42]. The general idea is that an available SRTM as the DEM is good enough for an accurate coregistration in the established approach.

The second impact that DEM has is the azimuth positioning error due to a change of effective velocity and squinting angle. In general, since the baseline of S1 is usually very small, the difference between master and slave effective velocity is very small, thus the interferometric phase difference with or without using DEM due to this factor is negligible [38].

The last impact appears in range direction with the presence of a squint angle. In the presence of a large height variation, say, a very high building, then there will be a mismatch for the building during coregistration because the projection of the building to different slant range direction will be slightly different. In stripmap case, this slight miscoregistration in range will only cause a decorrelation. In the case where a squint angle is presented, such as TOPS, then there will be a linear phase ramp imposed to the IRF in range direction (equation 2.2). The linear phase ramp will introduce a phase error if there is a slight miscoregistration in range direction as well [30, 36]. However, the effect is very small and negligible in general. Even if for very large height difference, since the squint angles in the TOPS mode are smaller than 0.7°, and also the baseline is small, thus the interferometric phase bias that is contributed by the range miscoregistration is still very small and can be considered negligible [36].

3.5.5 The Break Down Point of Cross-Correlation Method

This section explores the breakdown point for correctly performing the proposed approach. From the previous discussion, one could know that there should be two factors in general. The first factor is whether there are enough points with high SCR for estimating the rigid transformation matrix and avoiding the phase ambiguity in the ESD. The second factor is whether the cross-interferogram phase is too noisy for getting a robust estimation of the phase & slope value in ESD.

Are There Enough Points for Rigid Transformation to Avoid ESD Phase Ambiguity? The previous calculation shows that a 0.05 pixel coregistration accuracy is enough for avoiding the ESD phase ambiguity. In theory, this is equivalent to around 10 strong scatterers with SCR over 10dB. In most cases, this should be a relatively easy goal to reach, even when one's processing area is small. Then the ESD step is able to compensate for the coregistration residuals (assuming that the estimation of ESD phase & slope is correct).

Here one interferogram near Purdue University with 24 days temporal baseline is given[5]. The AOI has 1,200 range samples and 4,000 azimuth lines, making it a relatively small area. Again the majority of AOI consists of distributed scatterers. In the cross-correlation process, 120 points with SCR over 7dB are selected for estimating and performing the rigid transformation. This corresponds to 0.02 pixel coregistration accuracy, or 1.2 radians in cross-interferogram phase. In figure 3.10, the average phase from the cross-interferogram is more or less this value; but the rotation angle estimation error in this case is larger. Still, the example shows that around 100 points is enough for the cross-correlation method to avoid the phase ambiguity in ESD. The difference in interferogram between the proposed approach and the established approach is mostly limited to within 0.05 radians. A few spots still show phase difference approaching 0.05 radians. This discrepancy should mainly come from the

[5]Dataset used for this example:
S1A_IW_SLC__1SDV_20180302T234015_20180302T234043_020843_023BEE_CDC1
S1A_IW_SLC__1SDV_20180326T234016_20180326T234044_021193_02470B_BE68

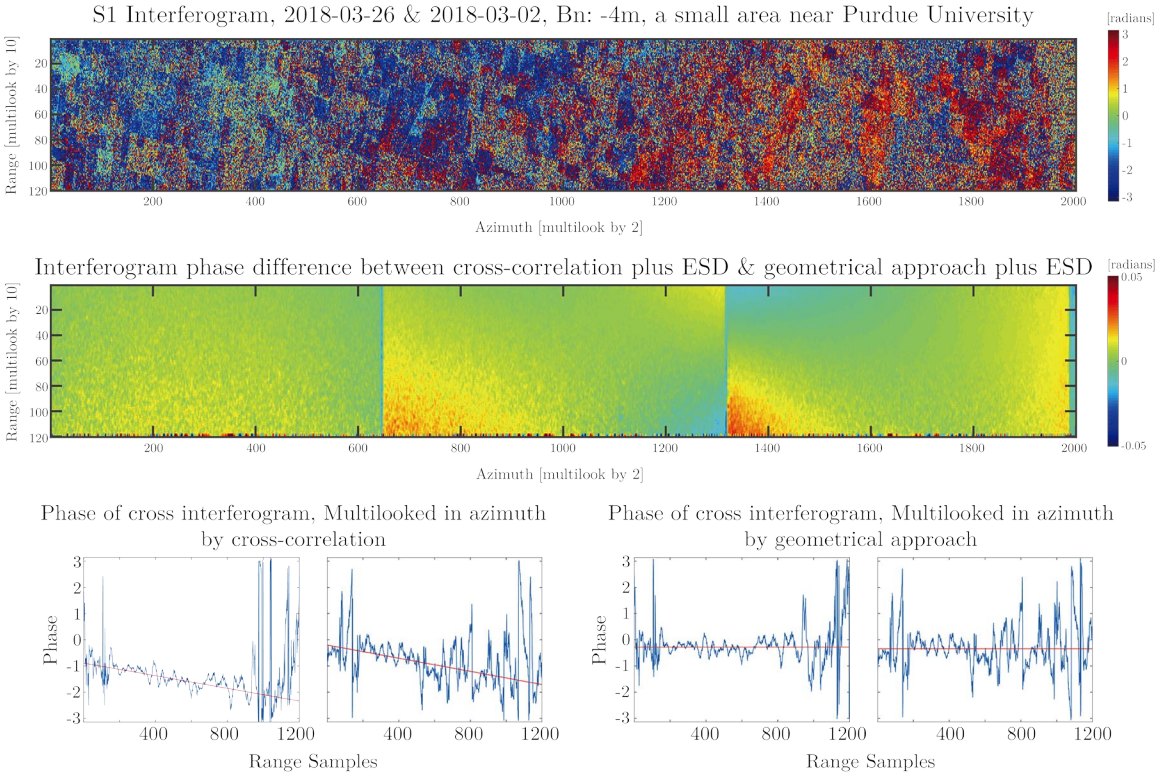

Fig. 3.10. An example near Purdue University as a small test site. The AOI is 1,200 (range) × 4,000 (azimuth). First row: the interferogram mutlilooked by 10 × 2 with no filter applied; Last row: the difference of interferogram phase between the proposed approach and the established approach; Last row: the cross-interferogram after applying the cross-correlation method and after applying the geometrical method.

estimation error of the ESD phase and slope, which will be discussed in the next section.

Cross-correlation Method with Long Temporal Baseline As discussed in previous sections, for the established approach, the coregistration residual after the geometric approach is mainly a constant value, so that one could conveniently estimate one value for one burst overlapping area. However, in the cross-correlation method, there is the rotation angle estimation error, which will be reflected as a linear slope in the range direction on the cross interferogram. The slope needs to be

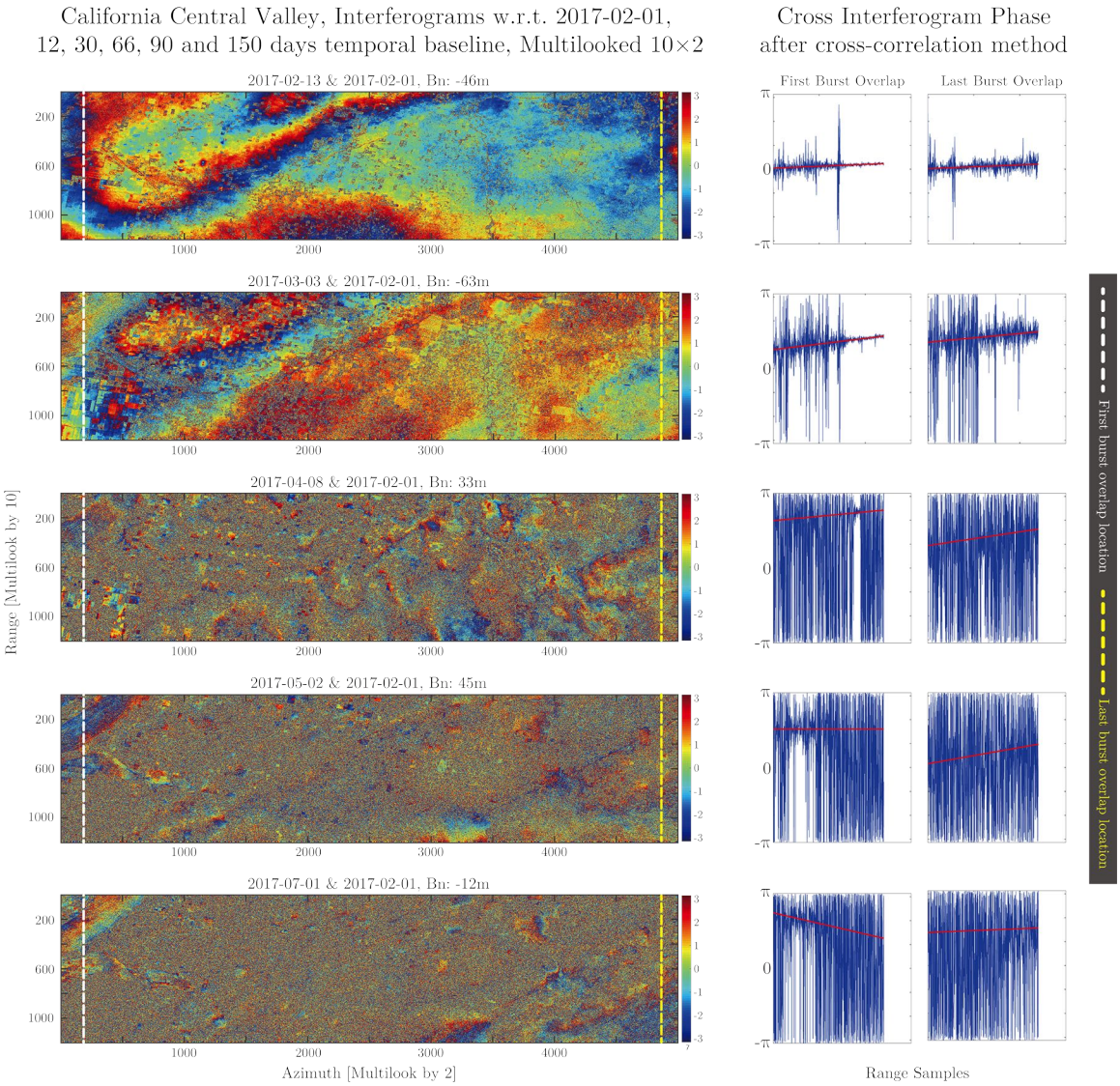

Fig. 3.11. The test case in California Central Valley. The interferograms are processing with the proposed approach. From top to bottom, the temporal baseline is 12, 30, 60, 90 and 150 days. For each data, the first burst overlap area (location showed in white dash line) and the last burst overlap area (in yellow dash line) are shown as example. The test site has 12,000 range samples and 10,000 azimuth lines. The interferograms are only multilooked 10 (range) by 2 (azimuth). No additional filter is applied.

estimated and removed. If the slope is wrongly estimated, the error will propagate to the interferogram.

The accuracy of estimation depends on the SNR of the cross-interferogram phase, or equivalently, the coherence. It is already well known that the coherence decreases as spatial and temporal baseline increase. For Sentinel-1 the spatial baseline is well controlled to a small orbital tube, so that the spatial decorrelation is not the key factor here. In this experiment, I use the proposed approach for image pairs with from 12 days to 150 days temporal baseline. The test site is the California Central Valley. The Central Valley is a flat valley in the center of California, and the majority of the valley is vegetated. The situation is very similar to the previous test case of Purdue University. For the experiment, the image on 2018-02-01 is set as the master and is paired up with images from 12 days to 150 days apart. Each image has 12,000 range pixels and 10,000 azimuth lines. 5 interferograms with 12, 30, 66, 90 and 150 days temporal baseline are shown in figure 3.11. The interferograms are multilooked by 10×2.

The interferogram decorrelates exponentially with temporal baseline. In this example, the 12-days-baseline and 30-days-baseline still shows a "clean" cross-interferogram, where the slope could be well estimated with a higher significance level. Then as the temporal baseline increase, the interferogram becomes noisier, and the estimation of ESD phase & slope will have much lower significance level. When the cross-interferogram is incoherent and the estimation is not precise, then the coregistration error will be carried into the interferogram as the phase error.

Figure 3.12 shows the cross-interferogram phase standard deviation as a function of temporal baseline. For each pair of images, the phase standard deviation is the average for all burst overlaps in the cross-interferogram. It could be observed that the reciprocal of phase standard deviation decays exponentially in time. At around 60 days, the value reaches approximately 0.35 and stays more or less the same afterward. Consider a scene with complete circular Gaussian noise, then the phase should be uniformly distributed and the phase standard deviation is $\pi^2/3$, roughly around 3.3,

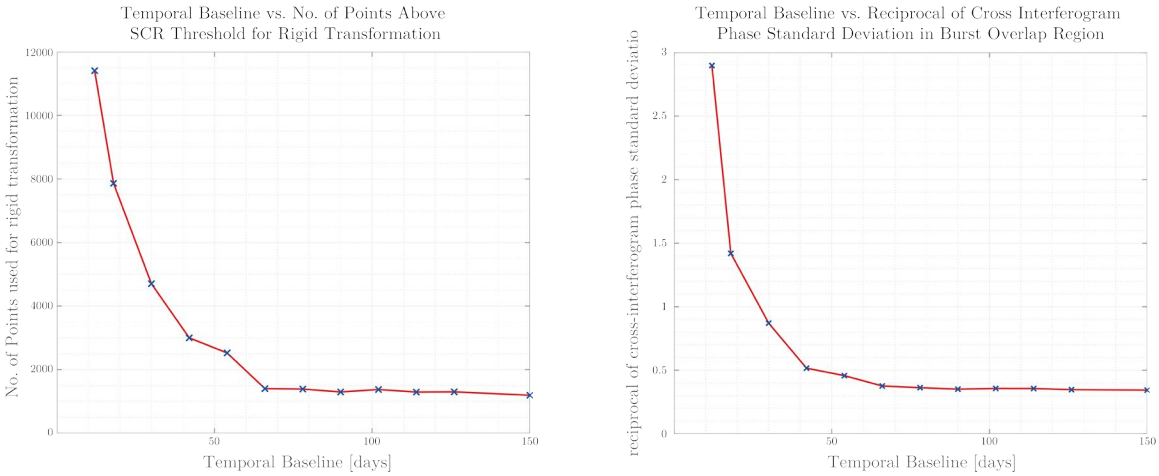

Fig. 3.12. Left: the number of available points with SCR greater than 7dB used in cross-correlation method as a function of temporal baseline. Right: the average reciprocal of cross-interferogram phase standard deviation in burst overlap area as a function of temporal baseline. When the reciprocal value approaches 0.3, the scene will be totally noisy, meaning it is very unlikely to estimate correctly the ESD phase and slope from the data.

making the reciprocal value around 0.3. This means that at around 60 days the cross-interferogram becomes almost totally noisy and the estimated phase & slope might not be reliable.

On the other side, although the number of points with SCR higher than 7dB also decrease exponentially in time, after 60 days the value becomes quite stable at around 1,000. As discussed in the last section, this number is still enough for avoiding the ESD phase ambiguity. Thus the key to a successful coregistration is to select pairs with short temporal baseline and coherent interferometric phase. This test dataset shows that it is possible to get a good estimation of phase and slope for temporal baseline shorter than 50 days. After that, the cross-interferogram might be too noisy, and the estimation will have a lower level of significance, possibly giving a non-negligible error to the interferogram.

It is worth noting that, for a time series analysis, with the aforementioned discussion, it is thus not recommended to use a single-master approach to perform the proposed approach. For retrieving coherent image pairs, one can either use the MST graph or a redundant graph approach [31, 32]. The other improvement that could be done is to estimate the ESD phase and slope not with the full burst overlapping area, but only with strong and coherent scatterers (that are not affected by noise).

3.6 Summary

This chapter studied the coregistration accuracy using the cross-correlation-and-rigid-transformation method (referred to as "cross-correlation method" throughout the chapter) and analyzed the feasibility, correctness, and robustness of coregistering Sentinel-1 TOPS images using the cross-correlation method followed by the enhanced spectral diversity (referred to as "proposed approach"). The idea of Cramér-Rao lower bound is used for studying the accuracy of the two key steps in the cross-correlation method. Based on the analysis of CRLB, the coregistration accuracy mainly depends on the number and signal clutter ratio of points/patches that are available for the rigid transformation. For increasing the coregistration accuracy, it is desired to have more points with higher SCR.

In the proposed approach, the rigid transformation step will estimate a rotation angle for the slave image. An estimation error of the rotation angle, albeit small, will introduce a modulation in range to the cross interferogram and will be reflected as a linear slope on the cross interferogram phase in range. For successfully performing the proposed approach, a key step is to estimate well the starting phase and the slope, thus to correct the rotation angle error.

To verify the correctness of the proposed approach, I compared the interferogram from the proposed approach with the established approach (geometrical plus ESD). The experiments show that the most important factor for success is the coherence of cross interferogram. For example, when the area is less coherent, the estimation of

slope in ESD might not be precise, and the interferogram might be erroneous. The most likely contributing factor to a low coherence is the temporal decorrelation. Still, in the two general cases (Purdue University and the California Central Valley), for a site that is dominated by vegetated land and has 24 or 30 days temporal baseline, the proposed approach could work well. Work well means that the interferogram difference with the established approach is mostly within the 0.05 radians error margin.

To avoid the phase ambiguity in the ESD step, the experiments show that 100 points or more is already good enough, which is relatively easy to achieve. However, with smaller areas or less coherent areas, the question again becomes if the estimation in the ESD step could be successfully performed.

At last, for areas with large topography variation, due to the presence of the orbital crossing angle, and the fact that the proposed approach failed to consider the topography during coregistration, there will be an azimuth miscoregistration and it will introduce a non-negligible phase error. For Mt Etna case with 123 m normal baseline and 3,000 m height variation, this topographic miscoregistration will introduce at most 0.1 radians interferometric error.

4. TOPS INTERFEROMETRIC PROCESSING FLOW

4.1 Introduction

This chapter describes the technical implementation of a "stripmap-like" interferometric processing flow for TOPS. In this "stripmap-like" approach, the discontinuous bursts of wide swath mode for the same subswath are stitched into a continuous SLC image at the very beginning of the processing chain. For users who wish not to get into the complexity behind the wide swath mode and simply want to use the interferometric products, this implementation provides the identical processing steps and output products to the stripmap case. This implementation designs a user-friendly processing interface, where all the wide-swath-related processes are hidden under the hood. In addition, this approach makes the best use of an existing standard InSAR processing software. In this chapter, the complete processing chain for TOPS is elaborated and some key issues are discussed, starting from stitching, deramping to coregistration and ESD. A quick implementation of fine coregistration during the ESD step that does not require resampling the slave image using the conventional method is also introduced. In addition, the minimum spanning tree (MST) graph is proposed for deciding the coregistering sequence when processing a stack of images. A MST updating algorithm is proposed for updating new images to the existing stack.

This chapter is organized as follows. The second section gives the background and introduction to the proposed interferometric processing chain. The third section introduces the design of the processing interface. The fourth section describes the technical details behind the implementation of the TOPS interferometric processing chain. A quick way of doing slave resample in the ESD is also introduced here. The fifth section introduces the MST approach to coregister a stack of images. The last section shows two interferometric examples.

4.2 The "Stripmap-like" Processing Chain for TOPS

Despite the increasing popularity of the wide swath mode, the interferometric process is still more complicated than the stripmap mode. For users who only have the basic familiarity with the stripmap mode, and simply wish to derive the interferometric product for their own Earth observation applications, the burst mode of wide swath looks quite counterintuitive. This is because the burst mode SLC is not continuous in the azimuth (see figure 4.4), making it very different from the stripmap case and harder to interpret. In addition, the wide swath mode requires extra steps in the coregistration, including deramping/reramping and ESD, that requires some fundamental understanding to the signal characteristics of the wide swath mode.

Currently, one approach that is widely adopted in the SAR community for processing the wide swath mode (including both ScanSAR and TOPS) is to process each burst individually and to generate the burst interferogram. The burst interferogram is stitched into the continuous interferogram at the last step (figure 4.1). Examples of this approach are [61] and [62] for ScanSAR, and [63] and [9] for TOPS. The advantage of this approach is that it is straightforward to think and easy to implement. One starts by reading in the burst mode SLC image (figure 4.1). The coregistration (with the geometrical approach [29]) and the ESD steps are all performed on the burst SLC. It should be noted that, although there are overlapping areas between adjacent bursts, they are not redundant information because they have different phase values. For the burst SLC, the bursts are kept intact and no signals (for the overlaps between bursts) are thrown away. Since the signals from the overlaps are required in the ESD step, then they could be read conveniently from the (resampled) burst SLC. The software development complexity for this approach is lower.

In this chapter, another approach is proposed, which is to generate a continuous SLC image, identical to a stripmap SLC image, at the very beginning of the processing chain. The initiative of this approach is to provide a more user-friendly interface for users who do not wish to understand all the theories and processing steps of

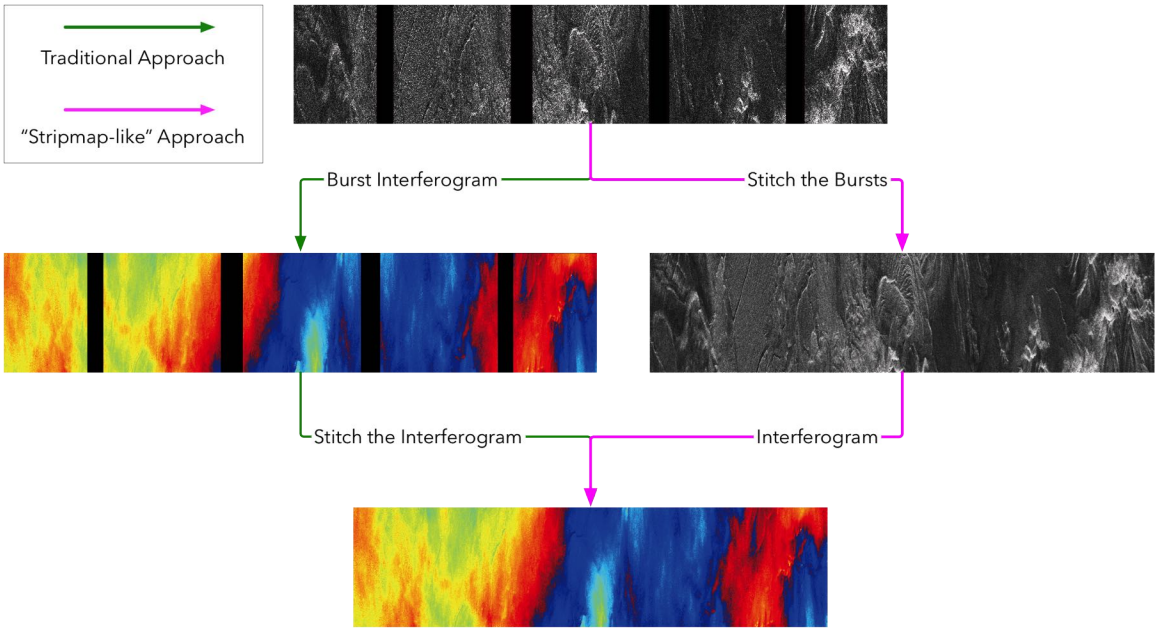

Fig. 4.1. A comparison between the conventional wide swath interferometric processing flow and the proposed "stripmap-like" flow.

the wide swath mode, i.e., burst mode, stitching (in some literature this is referred as "debursting" [63]), deramping, ESD, etc. Users will start by seeing the images exactly the same as for the stripmap mode. For non-expert users, no extra steps or knowledge is required for data processing, and no difference will be noticed in the processing software interface. The wide-swath-related processes are implemented under the hood. In addition, the stripmap-like processing chain would take advantage of an existing and mature stripmap processing platform. The integration between the proposed processing flow for wide swath and existing stripmap processor would be more convenient in the aspects of processing platform development and maintenance. A realization of this approach is shown in figure 4.2.

Stitching bursts into a continuous SLC as the very first step is not entirely a new idea. In the past, some software also implemented similar ideas [64, 65]. However, very few technical details were revealed in the reference. [59] also implemented a very similar idea, but a lot of the details deviates from what will be discussed in this article.

For example, in [59]'s paper the author only performed the deramping process and modulated the signal to baseband, but in this chapter, one will still reramp the signal after the initial coregistration. Compared with previous studies that showed similar ideas, this chapter will focus more about the technical details in the following aspects:

1. To design the user-friendly "stripmap-like" interface for processing the wide swath mode. As mentioned above, this interface, including the processing steps and all outcomes will be identical to processing a stripmap;

2. In addition, a simple method is proposed for correcting the miscoregistration that is estimated during the ESD step. This method does not require a re-sampling of the slave SLC using the conventional interpolation methods, but only requires a modulation in the frequency domain. This method will be more efficient because it only requires a point-wise multiplication in the time domain.

4.3 The Processing Interface Design

Compared with the traditional approach, the proposed approach considers more from the user experience and software development compatibility point of view. Figure 4.2 shows the designed "stripmap-like" processing interface and the basic processing flow. On the left of figure 4.2 is the interface. For users, the interface, processing steps and outcomes (SLCs and interferograms) are all identical to the stripmap case. No wide-swath-related processing steps and products are revealed in the interface. Anyone with the basic understanding of stripmap interferometric processing could also process wide swath mode with this interface and processing flow, and derive interferometric/time series analysis products. On the right of the figure is the processing sequence of the wide-swath related steps that are implemented behind each button. It should be worth mentioning that the proposed processing flow and the interface are already implemented into an existing SAR/InSAR processing package, SARPROZ [66], and is open to the public users.

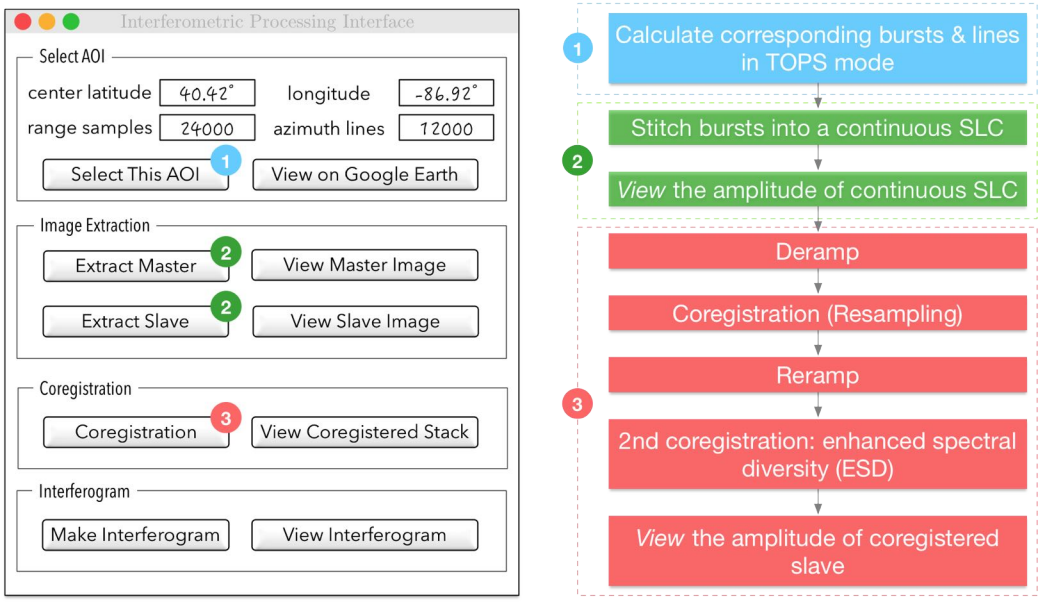

Fig. 4.2. The sketch of the interferometric processing interface for the proposed processing chain. Left: the user interface. Right: an overview of the wide-swath related processing steps that are implemented behind each button.

4.4 The Interferometric Processing Flow

Figure 4.3 shows the complete proposed interferometric processing flow. Note that the color in figure 4.3 corresponds to the colors in figure 4.2 that represent each steps. In sequence, the proposed processing chain includes the following steps: (1) stitching all bursts together into a single SLC image; (2) deramping the quadratic phase of each burst; (3) conducting the initial coregistration either using the cross-correlation method [37] or the geometrical method [29]; (4) reramping the resampled quadratic phase back to resampled (coregistered) slave image; (5) conducting the fine coregistration using the ESD method and compensating for the miscoregistration that is estimated by ESD; (6) generating the interferogram. Some of the standard process details could also be found in [9]. Next paragraphs will address some key steps, issues and new implementations.

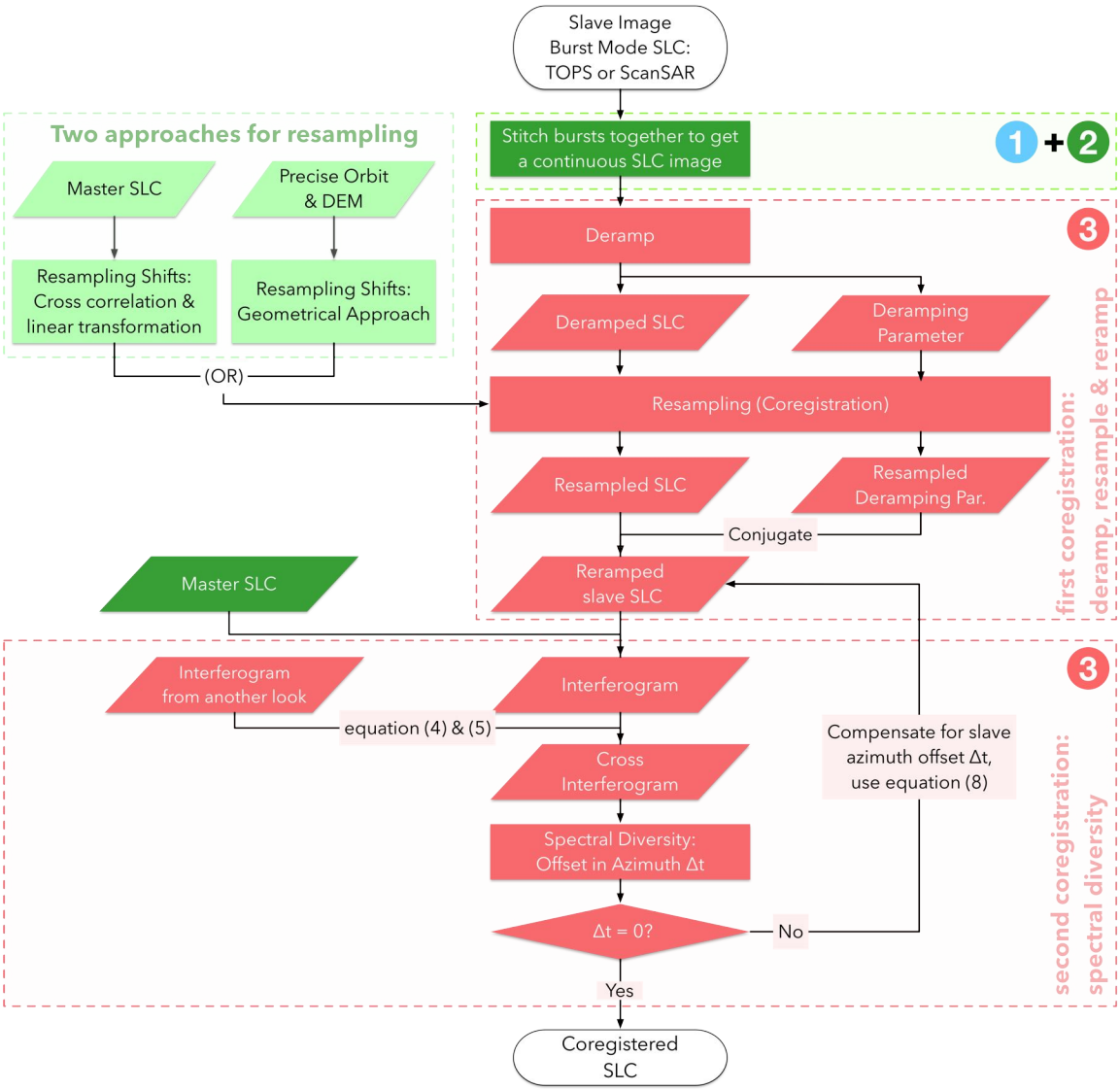

Fig. 4.3. The complete interferometric processing flow for TOPS (and ScanSAR, which will be discussed in the next chapter). The color and the numbers correspond to the processing steps in the designed interface that is shown in figure 4.2.

4.4.1 Stitching Bursts

As shown in figure 2.1(b), there is always an overlapping area between adjacent bursts so that one could stitch them together seamlessly. The idea is simple. The zero

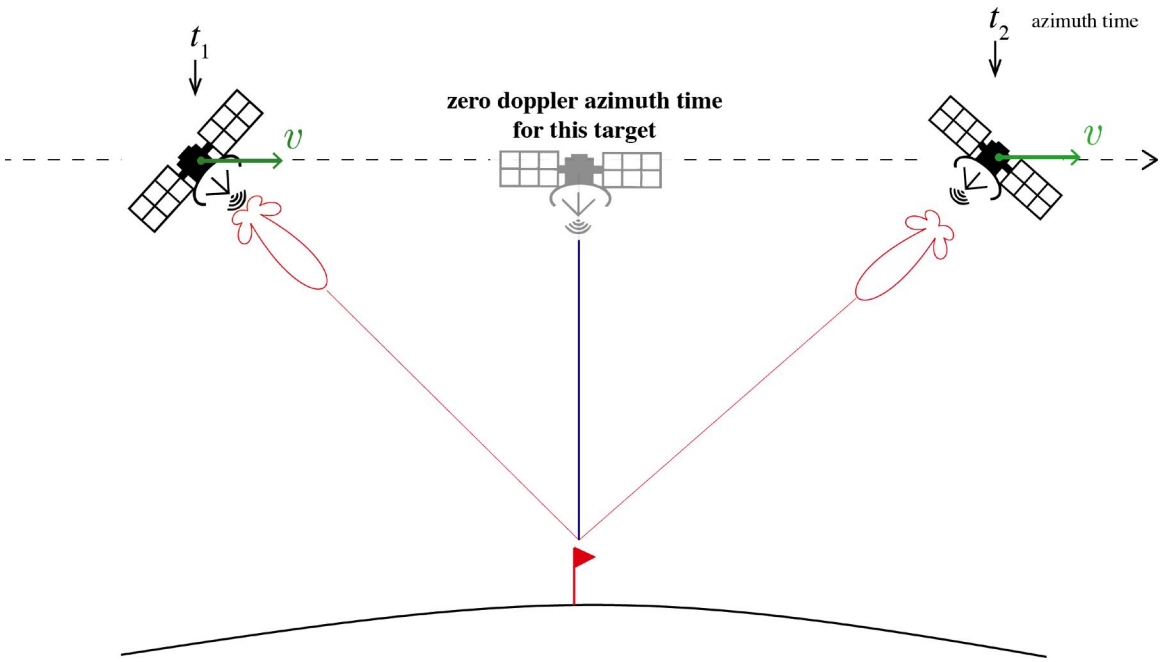

Fig. 4.4. Stitching bursts using the zero doppler time tag of each target.

doppler azimuth time tag for each line is used for stitching. As shown in figure 4.4, take one target standing inside the bursts overlapping area as an example. The target would be illuminated twice at time t_1 and t_2. However, the zero doppler azimuth time for this given target is unique because the zero doppler position of the satellite with respect to the target is unique. Sentinel-1 SLC is focused to zero doppler azimuth time and this time tag is written for every target. The zero doppler time tag could be used to identify the same target in burst one and burst two. The stitching is done accordingly.

Another thing to make sure is the following: for the target shown in figure 4.4, there will be two time-tags written for this target, recorded separately in burst 1 & burst 2. It is important to make sure that the two time tag have negligible difference during SLC formation process. Since TOPS coregistration requires a 0.001 pulse repetition interval (PRI) coregistration accuracy [9], the time tag difference should be much smaller to avoid introducing extra error during the ESD steps. For validating

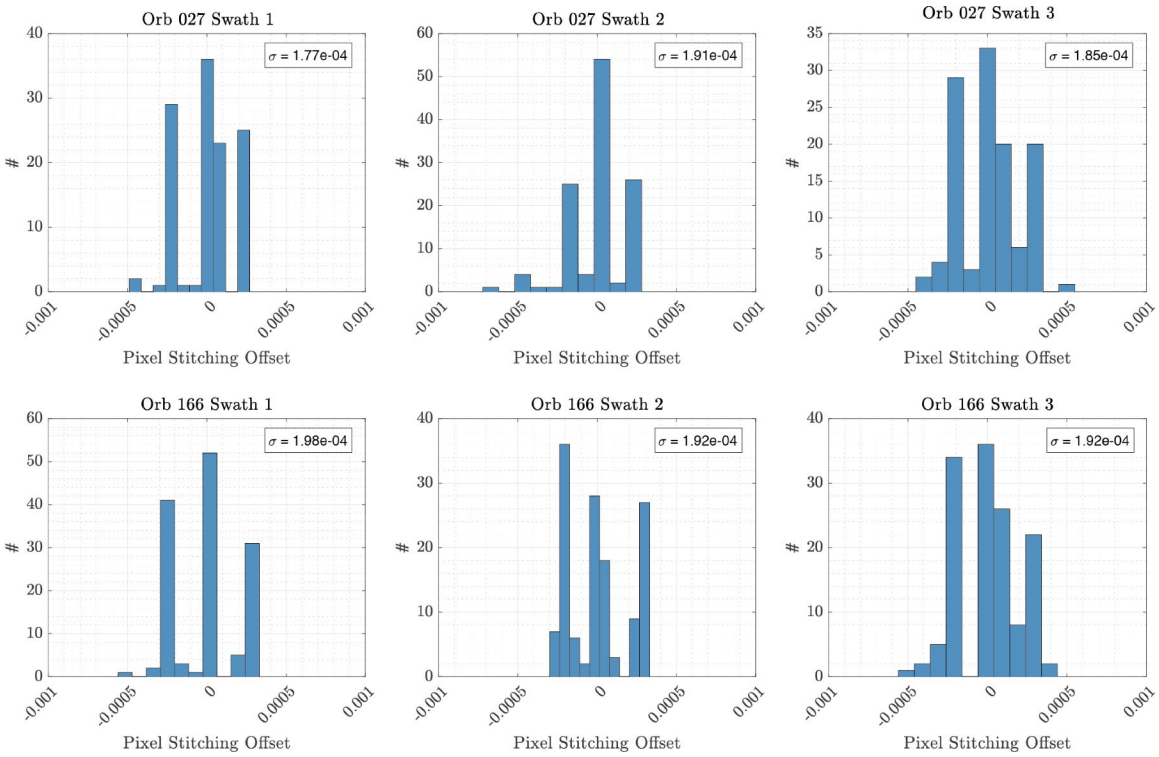

Fig. 4.5. The histogram of zero doppler time difference for targets in the burst overlapping zone. A total of 117 adjacent bursts are selected for the S1A track 27 and 135 bursts for S1B track 166.

purpose, I took one slice of S1A that consists of 117 bursts and one slice of S1B that consists of 135 bursts. The time difference in the unit of PRI for the same target in burst i and $i+1$ are plotted as histograms and shown in figure 4.5. The result shows that the variations are all within 2×10^{-4} PRI, one-fifth of 0.001 PRI. An accurate regular sampling space means that after stitching the sampling space remains a constant and no further resampling is needed. As a matter of fact, in the early experimental stage of S1A, it has been reported that [67] the time difference for stitching can be as high as 0.01 pixel, which means a resampling process is needed when stitching so that all pixels are in a common sampling grid. The issue was reported to be resolved by ESA later on.

At last, due to Sentinel's burst nature, concatenating more than one consecutive SLCs in azimuth direction for the same subswath is the same as stitching the bursts. The way that most SLCs delivered by ESA consists of nine bursts per subswath is merely a human-made rule. It is a trivial step to stitch consecutive SLCs in the azimuth direction.

4.4.2 Deramp

The deramping step comes directly from IRF (equation 2.1). Again, TOPS is total zero doppler steered, which means in equation 2.1, f_{η_c} is close to zero and can be considered as independent of range (in reality, f_{η_c} still varies in range, but the variation is very small and could be considered negligible [33]), so that IRF is baseband without the quadratic term (third term). The azimuth bandwidth without the quadratic term for TOPS is around 313Hz and the PRF is approximately 486Hz. However, with K_t around 1750Hz/s and $\eta - \eta_c$ taking 1.35s maximum, the maximum bandwidth for the quadratic term is around 3200Hz, almost 7 times the sampling rate. According to Nyquist theorem, resampling equation 2.1 directly in coregistration will alias the signal. The solution is to separate the quadratic phase term from baseband signal, resample them separately, and put them together afterwards. The baseband part could be resampled without any problem. An comprehensive instruction on deramp is given in [33].

The parameters in quadratic phase, namely K_t, η and η_c, could be precisely calculated or directly read from the meta file. Then the deramping process is simply the following:

$$s(\eta) \cdot \exp\left\{ -j \cdot \pi \cdot K_t \cdot (\eta - \eta_c)^2 \right\} \tag{4.1}$$

A plot of the spectrum before and after deramp process is shown in figure 4.7. To emphasize the azimuth-dependent quadratic phase before deramp, the spectrogram is also plotted in azimuth direction. A linear variation in azimuth direction in frequency domain could be observed. By equation 2.1 one should know that the slope in figure

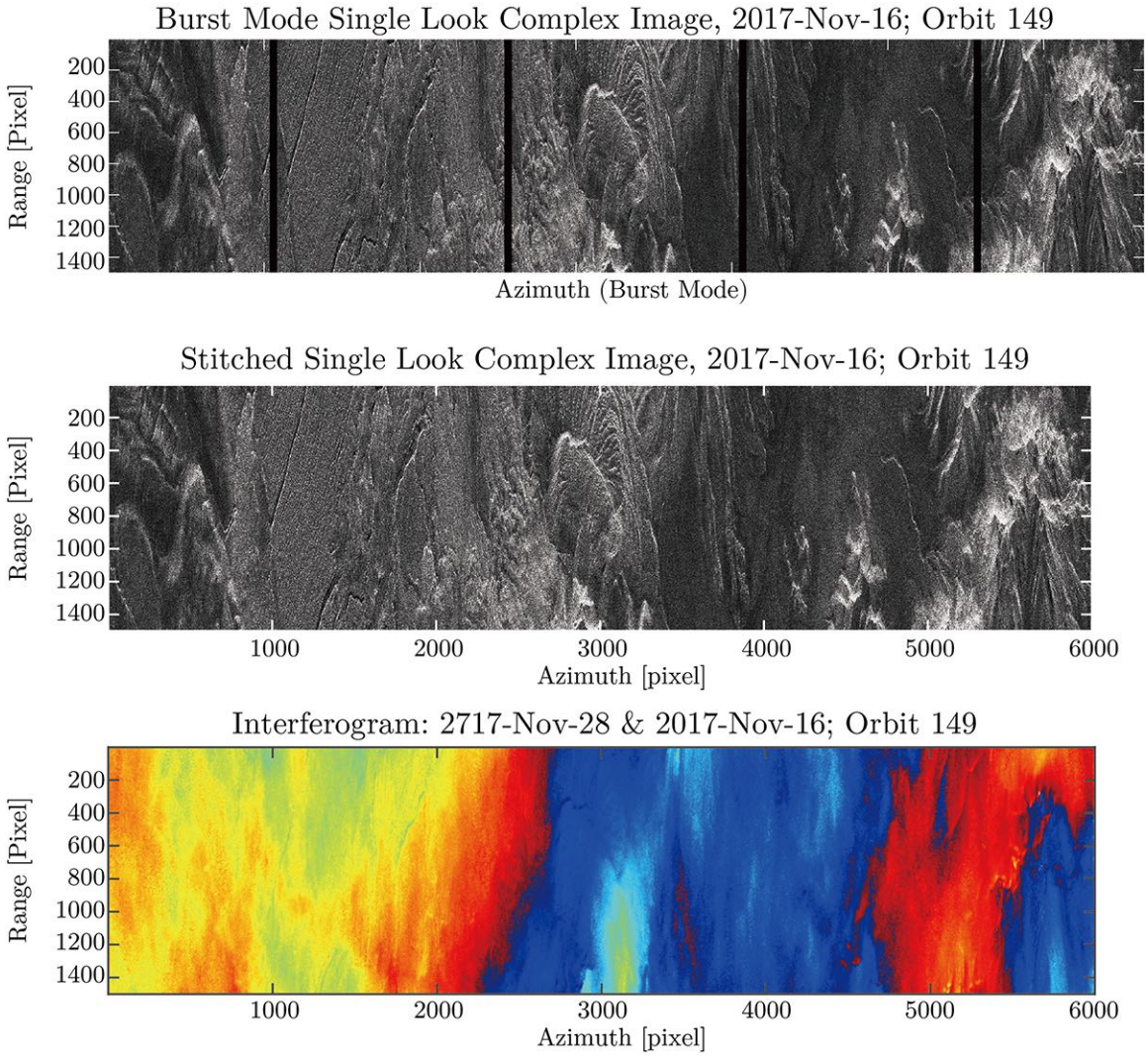

Fig. 4.6. An example of the original burst mode image and what it looks like after the bursts are stitched together into a continuous SAR image. Top: a subsection of the full SLC data that contains 1,500 samples in range and 5 bursts. The same ground features could be observed at the edges of burst i and burst i+1. Middle: the stitched SLC image where the ground features are stitched seamlessly using the time tag. Bottom: The corresponding interferogram of the stitched SLC.

4.7(b) is equal to $2\pi K_t$. After applying equation 4.1, two things happen: (1) The spectrum in azimuth is azimuth dependent; (2) The spectrum is restrained within PRF. At this point the deramped slave image could be resampled aliasing-free.

Two trivial things regarding this topic:

1. TOPS is zero doppler steered, and f_{η_c} is very close to zero. For resampling process it is not necessary to demodulate azimuth frequency to baseband, since the PRF of TOPS system left enough margin in azimuth bandwidth. However, when one is using S1A or S1B data from their commissioning phase (S1A is before September 2014, S1B is before September 2016), it has been reported that the doppler centroid frequency could exceed 100Hz [13, 41]. In such cases it is advised to also demodulate to baseband before the resampling process.

2. Figure 4.7(e) and (f) shows that the range spectrum is baseband. This corresponds to the IRF function (equation 2.2) in range as well. No extra care needs to be taken during the resampling process on range.

4.4.3 Coregistration and Reramping

The coregistration is already being thoroughly discussed in chapter 3. Here a few points not discussed previously will be stated here.

As shown in the previous chapter, during the initial coregistration step, where cross-correlation approach or geometrical approach is used, one can generally reach an accuracy of 0.05 pixel or less depending on the quality of data or orbital state vectors. Regardless the coregistration method that is used, the essence is to calculate the sub-pixel offset between each targets on master and slave image. The slave image is then interpolated using this offset map. One will first resample the deramped baseband complex signal in 4.1. For resampling the quadratic phase, only the phase part $\phi = \pi K_t(\eta - \eta_c)^2$ is resampled. This is a real number and could be resampled without getting any alias. It is because the real part is only a quadratic function with no significant high frequency oscillations. The bandwidth is limited. The sampling theorem could apply here. After the real part is resampled, it is wrapped inside the $\exp(j\cdot)$ operator and multiplied to the resampled baseband signal. This step is referred as reramping.

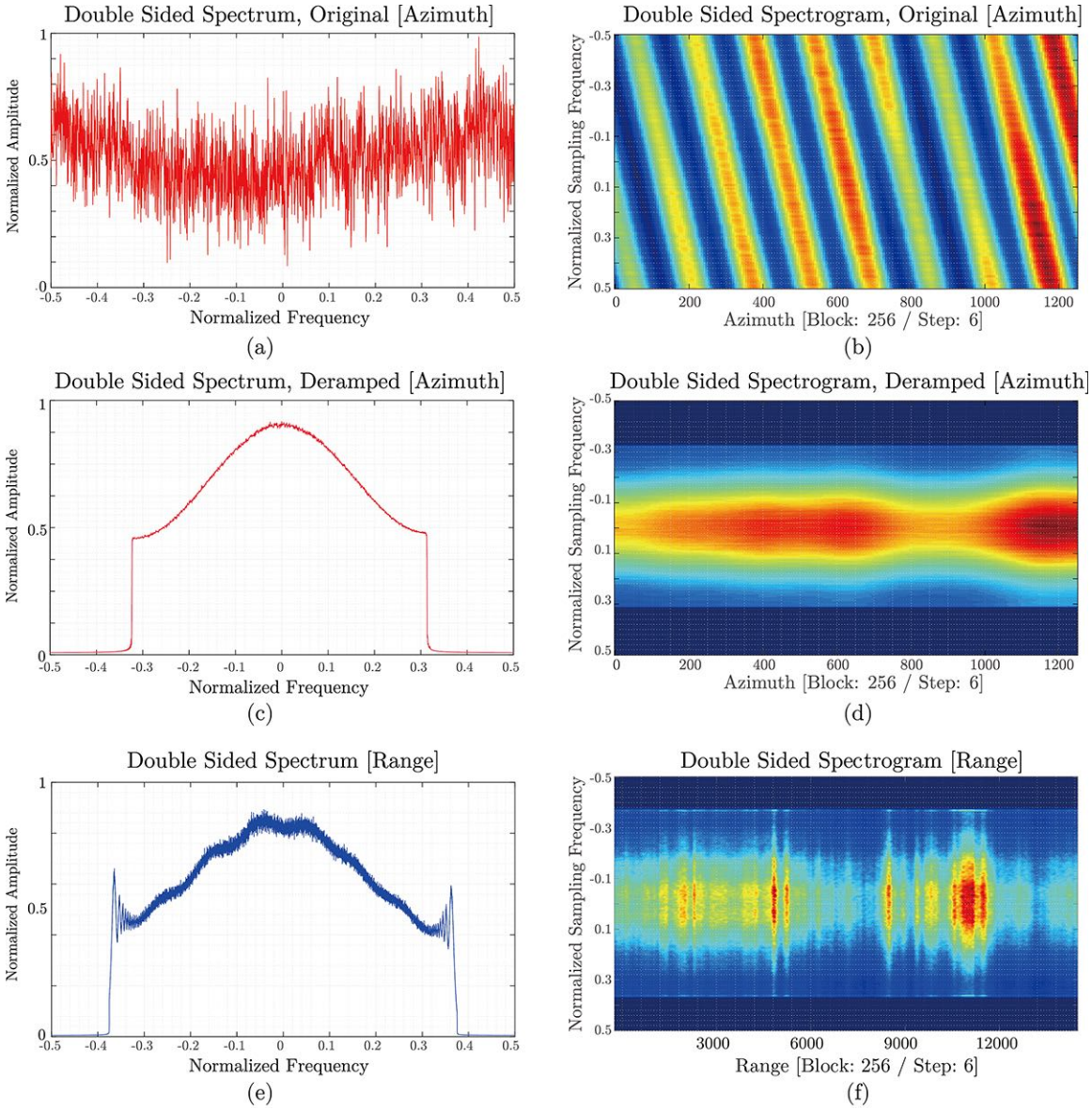

Fig. 4.7. The spectrum and spectrogram on azimuth and range direction for one single burst of TOPS. The spectrograms are calculated in blocks of 256 pixels and steps of 6 pixels. The frequency labels are all normalized frequency. (a)&(b): frequency domain along azimuth direction, the original data; (c)&(d): frequency domain along azimuth direction, after the deramping; (e)&(f): frequency domain along range direction. Range spectrum is not influenced by the deramp process in azimuth.

4.4.4 Enhanced Spectral Diversity and a Quick Implementation of Correcting the Coregistration Error

From equation 2.1, suppose now there is a miscoregistration time Δt in the slave image, the phase difference between master and miscoregistered slave is:

$$\begin{aligned} s_S(\eta+\Delta t)\cdot s_M^*(\eta) = s_{a,S}(\eta+\Delta t)\cdot s_{a,M}(\eta)\cdot \exp\Big\{-j\cdot\frac{4\pi}{\lambda}\cdot\Delta R\Big\} \\ \cdot\exp\big\{j2\pi f_{\eta_c}\Delta t\big\}\cdot\exp\big\{j2\pi K_t\eta\Delta t\big\}\cdot\exp\big\{j\pi K_t\Delta t^2\big\} \end{aligned} \tag{4.2}$$

For simplicity, it is assumed that $\eta_c = 0$ in equation 2.1 (η_c only serves as a reference time and do not change the final conclusion). $\Delta R = R_0^S - R_0^M$ is the difference of R_0 between master and slave. In equation 4.2, there are two unknowns, ΔR and Δt, but only one observation, $s_S(\eta+\Delta t)\cdot s_M^*(\eta)$, known as the interferogram. The system is underdetermined and there is no solution for Δt. However, if one took another measurement, then there are two measurements for two unknowns, then the unique solution for Δt could be found. In TOPS, as shown in figure 4.4, the targets inside the burst overlapping area receives two measurements from two different squint angles (another equivalent terminology is "two looks". In figure 4.3, the terminology "look" is used). With the two measurements(looks), one will be able to calculate Δt. Here one can denote $s_S(\eta+\Delta t)\cdot s_M^*(\eta)$ as Ifg, then ESD will generate a so-called "cross-interferogram" by the conjugate multiplication of the two measurements:

$$\mathrm{Ifg}_{,1}\cdot\mathrm{Ifg}_{,2}^* = A\exp\big\{j2\pi K_t(\eta_1-\eta_2)\Delta t\big\} \tag{4.3}$$

The complex conjugate multiplication cancels out most of the terms in equation 4.2. A is the amplitude envelop. If one denotes the phase in equation 4.3 as:

$$\phi_{\mathrm{ESD}} = 2\pi K_t(\eta_1-\eta_2)\Delta t \tag{4.4}$$

Now it becomes an equation with one observation and one unknown. Note that ϕ_{ESD} could be easily read from the cross interferogram phase. Hence the miscoregistration time Δt is derived.

I introduce here a quick implementation of correcting the miscoregistration time Δt without the necessity of resampling the slave image again. In the first place, note that Δt is usually very small. Take $\Delta t = 165\mu s$ as an example (corresponds to 0.1 pixel misalignment, which is 100 times the required coregistration accuracy) and f_{η_c} as $20Hz$, then in equation 4.2, $\pi K_t \Delta t^2 \approx 1.5 \times 10^{-5}$. This is a constant term for the whole image with very small values. Also it is assumed that the envelop function $s_a(\eta)$ do not change significantly when shifting by a small amount Δt. Taking an approximation by neglecting the last term with Δt^2 in equation 4.2, one could have the following:

$$s(\eta) \approx s(\eta + \Delta t) \cdot \exp\big\{ - j2\pi f_{\eta_c} \Delta t \big\} \cdot \exp\big\{ - j2\pi K_t \eta \Delta t \big\} \tag{4.5}$$

Since it is assumed that the envelope function value does not change when shifting only a small amount, they canceled out when deriving equation 4.5 from equation 4.2. Now, by combining equation 4.5 and 4.4 one would have:

$$s(\eta) \approx s(\eta + \Delta t) \cdot \exp\big\{ - j \cdot \phi_{\mathrm{ESD}} \cdot \frac{\eta}{\eta_1 - \eta_2} \big\} \cdot \exp\big\{ - j \cdot \phi_{\mathrm{ESD}} \cdot \frac{f_{\eta_c}}{K_t(\eta_1 - \eta_2)} \big\} \tag{4.6}$$

The last term in equation 4.6 is a constant phase term for the whole burst. This term is usually very small and is only adding a constant phase to the full image. A constant phase would not have any impact on the interferogram since it is already a double-reference measurement [44]. Thus the equation becomes:

$$s(\eta) \approx s(\eta + \Delta t) \cdot \exp\big\{ - j \cdot \phi_{\mathrm{ESD}} \cdot \frac{\eta}{\eta_1 - \eta_2} \big\} \tag{4.7}$$

This equation says that ESD could be applied by simply multiplying a linear phase term as a function of azimuth time η to the miscoregistered slave image. It does not involve any resampling process. Equation 4.7 also shows that no knowledge of the doppler centroid rate K_t is actually required for implementation. Theoretically, this is only true if one assumes K_t is exactly the same for the two different measurements. In reality, the variation of K_t for two different bursts is very small, so that one could safely consider K_t a constant value and accept this conclusion. At this point, the complete interferometric processing flow for TOPS could be concluded.

4.5 Minimum Spanning Tree: Coregister and Update Multiple Images

In previous sections, the focus is mainly on coregistering two images. In a time series analysis one will need to coregister a stack of images, thus the coregistering sequence become important. Firstly, for a long stack it is not suggested to coregister every slave images with the master image. This is because the ESD process depends greatly on the spatial coherence of the burst overlapping area [14], and that the spatial coherence decrease exponentially in time [25]. In this section I propose a very simple idea for finding the optimum sequence (in terms of the spanning tree) for coregistering a stack of images as well as updating new images to an existing stack.

MST is a very simple idea in graph theory and is already widely used in enormous applications, also including SAR imagery coregistration [68]. The greedy choice property of MST makes this simple algorithm well fit for TOPS ESD and updating new images to the already-coregistered stack. Here I want to illustrate how the properties of MST fit the purpose of coregistration.

In a typical time series analysis, at least twenty images are required. It raises the question of how to find the optimal sequence of coregistration pairs for performing ESD. Another question is how to find the optimal way to update a new image to the already-coregistered stack. MST could be a potential answer to both of these questions. The idea come from the greedy choice property of MST, which serves to the exact purpose of this scenario. A brief summarize of the greedy choice property is the following: locally optimal choices lead to global optimal solution.

The greedy choice property for MST is the following. For a graph $G = (V, E)$, suppose one cuts the vertices into two groups, S and $(V - S)$. Then any least weight crossing edge defined as $e = \{u, v\}$ with $u \in S$ and $v \in (V - S)$ is in some MST of G (some means when MST is not unique). The proof is given in [69].

The greedy choice of MST means the following:

1. Suppose one always wants to select the pair with the highest coherence value among all possible pairs. The property states that this pair (or, this edge) is in a MST tree;

2. After the first pair is selected, if one finds the pair (edge) with the second highest coherence value, then this pair is also in the MST tree;

3. Let's continues with the step in finding the edges with coherence value in descending order. If at one moment by adding one edge, the tree become cyclic, then this edge should be skipped and move to the next. The tree must be guaranteed to be a spanning tree at all time.

The above mentioned steps is actually the Kruskal's algorithm for generating the MST tree. It refers that all pairs with high coherence value will be guaranteed to be in the MST tree. In other words, one will always be able to perform ESD on those pairs with coherence value as high as possible.

4.5.1 MST in Selecting coregistration pairs

In the previous section, It has been shown that the key to ESD depends largely on the coherence of cross-interferogram at the burst overlapping region. A simple choice of edge weight for MST should be the coherence of cross-interferogram only at burst overlapping area. Since the weight is a single value, one could simply take a sample averaged coherence value as the weight. In addition, since it is needed to calculate the "minimum" spanning tree but it is wanted to choose pairs with maximum coherence, one could use either the reciprocal of coherence or negative of coherence as the weight value.

Using Kruskal's algorithm it could be seen that how the pair with highest coherence in order are selected to generate the MST (in the illustrated figure, it is actually generating the maximum spanning tree, but it is equivalent to negating the weight

and then apply the algorithm for the minimum spanning tree). In this section the steps of Kruskal's algorithm in finding optimal coregistration pairs will be given:

1. For a graph $G = (V, E)$ where V are the images and E are the edges that pairs up images with coherence as weight. All the E in descending orders will be sorted first. $E_T = \emptyset$ is marked at the very beginning. When the procedure finish, $T = (V, E_T)$ will be the desired MST.

2. All edges E are sorted in descending order;

3. One will start with the edge of the highest coherence value. For this edge $e = (u, v)$, it is added e to set E_T;

4. For each time a new edge is added into E_T in descending order, one needs to run a check first: if adding the current edge to the existing tree T will form a cycle, then this edge is discarded and move to the next.

5. The procedure stops when all the vertices are connected in the form of a spanning tree (a tree with no cycle and connects all vertices).

A more robust and scientific description could be found in [69]. Figure 4.8 is an illustration of finding MST in TOPS ESD coregistration. Kruskal's algorithm coincide with the idea in TOPS coregistration that one always want to find the pair with highest coherence value to minimize the coregistration error.

4.5.2 Updating a New Image to the Existing Stack

Another convenient point about MST is when updating new images. Both global & local optimal could be easily achieved with simple updating algorithm that comes from Kruskal's as well. There is no necessity in re-calculating the whole graph and only the newly added edges (that come with the newly added vertices) is needed for the adjustment. When the updating algorithm is presented, it could be shown that the updating algorithm also works in the sense that it always try to pick the edge

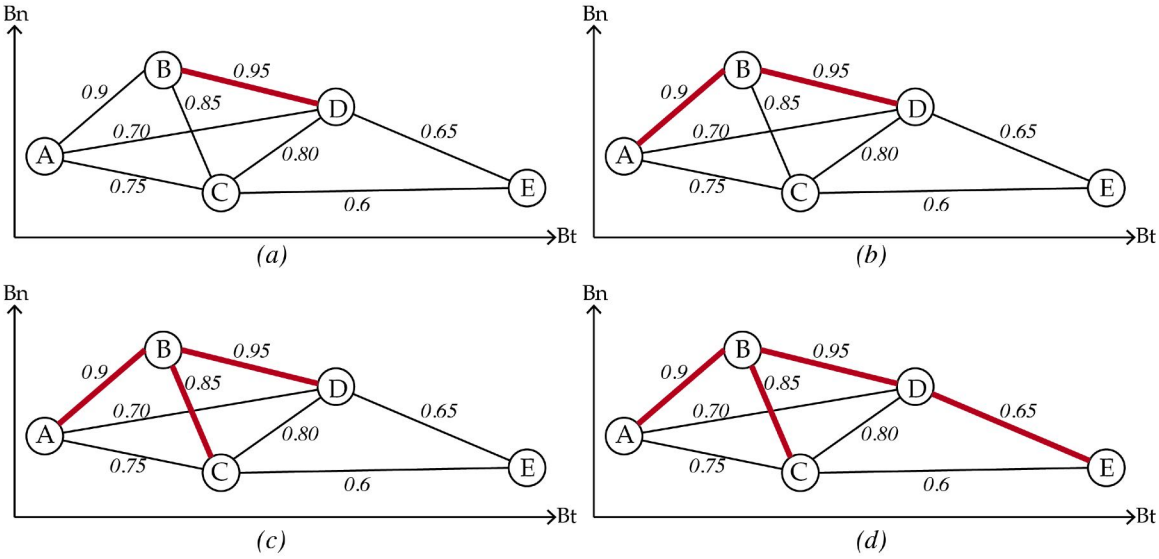

Fig. 4.8. An example of finding MST for 5 images. The weight on edges represents the coherence value in the burst overlapping zone. The x-axis is temporal baseline and y-axis spatial baseline. (a) The highest coherence is 0.95 connection B & D. This edge is added to E_T; (b) The next highest coherence is 0.9 connecting A & B; (c) The next highest coherence is 0.85 connecting B & C and is added; (d) The next highest coherence is 0.80 connecting C & D. But adding this edge to E_T will form a cycle: B->D->C->B. This edge is skipped. The next two edge with weights 0.75 and 0.70 will all form a cycle as well, so they are also skipped. Then the edge with weight 0.65 connects D & E and does not form a cycle. At this point the spanning tree is completed, and is shown as bold red lines in the figure.

with the highest coherence weight. Before I start, there are two lemmas that validates the whole updating algorithm [70]:

1. For a MST, $T = (V, E_T)$, if some vertices $v_{del} \in V$ and their corresponding edges $e_{del} \in E_T$ are deleted, then the remaining graph $T_{del} = (V - v_{del}, E_T - e_{del})$ is still a MST;

2. For a MST, $T = (V, E_T)$, if some vertices v_{add} and corresponding edges e_{add} are added to the graph. Suppose the MST for the new graph is $T_{add} = (V \cup v_{add}, E_{T,add})$, then $E_{T,add} \subset E_T \cup e_{add}$.

The first one says that if a vertex and the edge connecting this vertex from the MST are deleted, the remaining part is still a MST. The proof is simple. If the remaining part is not a MST, then there exist a MST. Thus if the deleted edge is added back, the original graph is no longer a MST as well (because one can use the "cut & paste" to replace the remaining part with the existed MST), this contradicts with the fact that the original graph is MST. The second one says that the edges of new MST must come from the edges of the original MST and the newly added edges. This could proved using exactly the same proof by contradiction method. With these two lemmas, the simple updating algorithm is ready to be presented here:

1. For a MST, $T = (V, E_T)$, if some vertices v_{add} and corresponding edges e_{add} are added to the graph. Find all the existing vertices $v_{del} \in V$ that are connected to the new vertices, $v_{add} = (v_{del}, v_{add})$. Remove all edges $e_{del} \in E_T$ that come from those vertices v_{del};

2. Now there is a new graph, $G_{add} = (V \cup v_{add}, e \cup e_{add})$. Also, partial of the graph edges are already part of the final MST tree, T_{add}. Different from the original Kruskal's algorithm that starts with $E_T = \emptyset$, here there is already a $E_{T,add} = E_T - e_{del}$ to start with.

3. Then one could just run the Kruskal's algorithm with the rest edges, $e_{add} \cup e_{del}$ until a spanning tree is completed.

An illustration is shown in figure 4.9. Here a new vertex U is added to the MST that is just computed. There are three edges coming out of U. These are the e_{add} and are marked blue. There are also three vertices connected to U, namely C, D, E. Correspondingly there are three edges from the three vertices in the original MST. These are the e_{del} and are also marked blue. Since partial MST is also a MST by the greedy choice property, it is not needed to compute the part $E_T - e_{del}$ again (marked as red in figure 4.9. So all one needs to do is to run the edges $e_{add} \cup e_{del}$ through Kruskal's algorithm to get the new MST. The proof of correctness is omitted here,

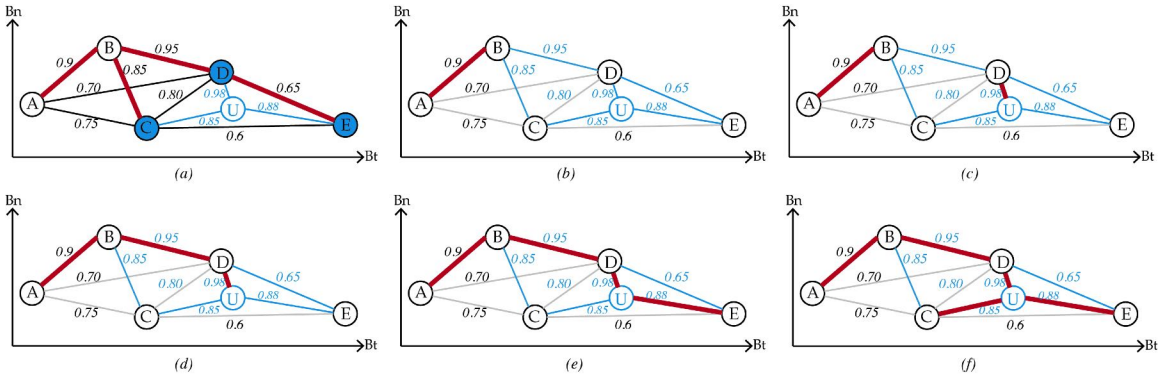

Fig. 4.9. An example of updating MST. (a) A new vertex U is added to the existing MST with three new edges marked as blue and connecting to three existing vertices, C, D, E; (b) All edges in the original MST that connects C, D, E are deleted and mark as blue as well; (c) Now all the blue edges are sorted in descending order and Kruskal's algorithm will be applied to the blue edges. 0.98 is the highest weight in all blue edges, so this edge is added to $E_{T,add}$ and marked as red; (d) Next is the edge with weight 0.95 and connecting B & D; (e) Next is the edge with weight 0.88 connecting U & E; (f) The last is edge with weight 0.85 connecting U & C. Now all the vertices are connected, updating MST is completed. It can be seen that the this particularly designed new MST removed two edges from the original MST and added three new edges.

but it is really very straightforward with the proof by contradiction and "cut & paste" that is mentioned above.

It is worth mentioning that, while there are a number of MST updating algorithms, this one is designed in particular to show that the algorithm is progressively making local optimal choices, i.e., choosing the best coherence that is available. This again shows that both the MST and updating algorithm coincide with the idea that one wants to choose the maximum coherence in ESD to minimize coregistration error.

Another point worth mentioning is the following. While this particularly designed example in figure 4.9 inserted a new image U in the middle of C, D, E to show that how the original MST edges are altered, in real-life scenarios, people tend to update images of only the newest. Due to the temporal decorrelation effect, it is most likely

that the updating algorithm will simple connect the updated image to the original MST without altering it.

At last, it is worth mentioning that there are other coregistration method for stack of images. Another widely used idea is to use redundant graph instead of the spanning tree [9, 31]. A redundant graph that comes with the least square method could be more robust to estimation error in exchange for computation complexity. In most cases where all coregistration pairs are having good coherence value, the simple MST method works well.

4.5.3 General Considerations for Coregistering Time Series Stack of TOPS Images

There are a few things that could introduce error to TOPS interferogram. The first consideration is the strong ground movement in azimuth direction. The strong azimuth movement will give interferometric phase jumps at burst edges. It should be noted that these phase jumps are legitimate geophysical signals and should not be considered as artifacts [10]. The other factor is atmosphere. While the atmospheric phase screen is quite unlikely to cause interferometric phase jumps [71], the ionosphere effect do have an impact to squinted acquisition mode such as TOPS and could create phase jumps in interferogram [72,73]. Studies have shown that it is desired to estimate the remove the ionospheric signal from the interferogram when the effect is strong. There are some other factors that could bias the final interferogram, such as DEM errors. However, for a very long stack of images, it is very likely that, in most of the cases all such factors will be within the noise level and be averaged out in temporal data stacking [71].

4.6 Two Examples

In this section two "classic" examples of TOPS interferogram are shown. The first interferogram is between a pair of images that come from the early phases of S1A in

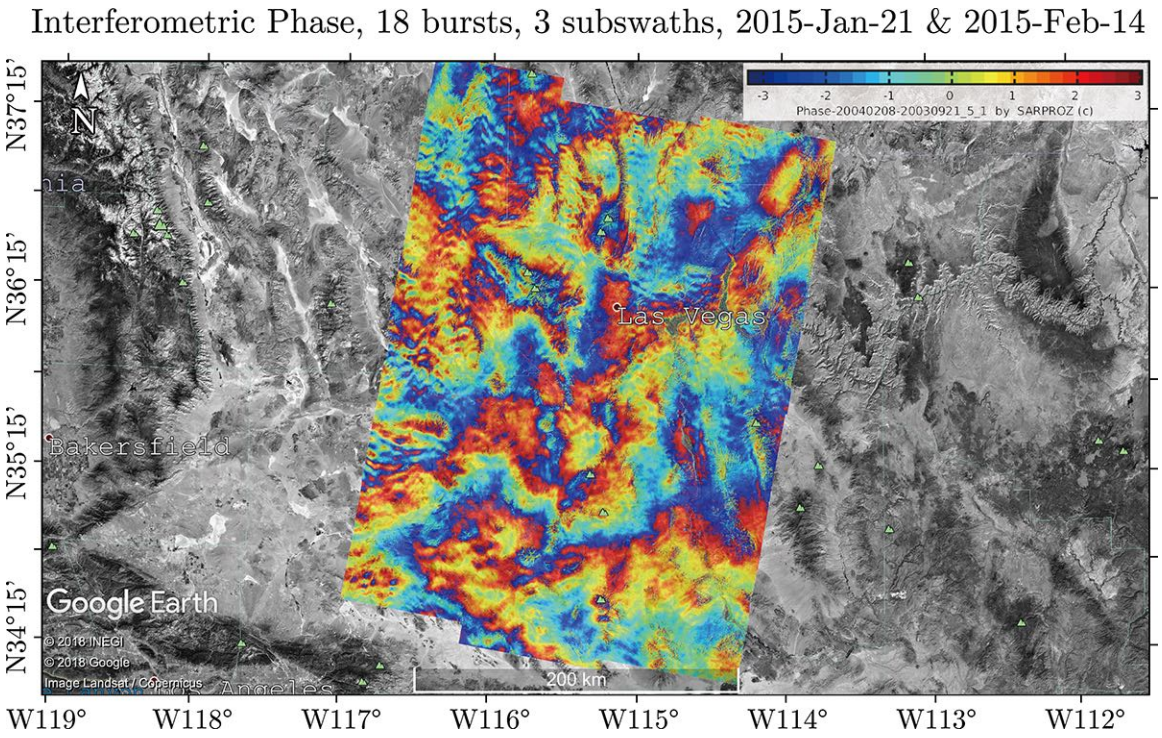

Fig. 4.10. Interferogram between date 2015-Jan-21 and 2015-Feb-14. The interferogram consists of 2 SLCs, 3 subswaths and 18 bursts each subswath on each date. The interferogram has removed topography based on SRTM. The fringes on the interferogram is most likely due to atmospheric effects. This area includes the Mojave desert and is an ideal site for interferometric purpose due to its high coherence.

January and February of 2015. The AOI is Las Vegas and Mojave desert in Nevada, USA. The desert usually means a very high coherence. High coherence means the dataset is the best candidate for testing the interferometric processing flow. The same dataset is also presented by [59]. The results from the reference and presented in figure 4.10 are identical.

The second example is a very good demonstration of TOPS's capability of large area monitoring, which is exactly what TOPS is designed and served for. On the 16th of September, 2015, an earthquake with magnitude 8.3 hit the offshore near Illapel, Chile. The huge impact of this major earthquake affected at least an area of 80,000

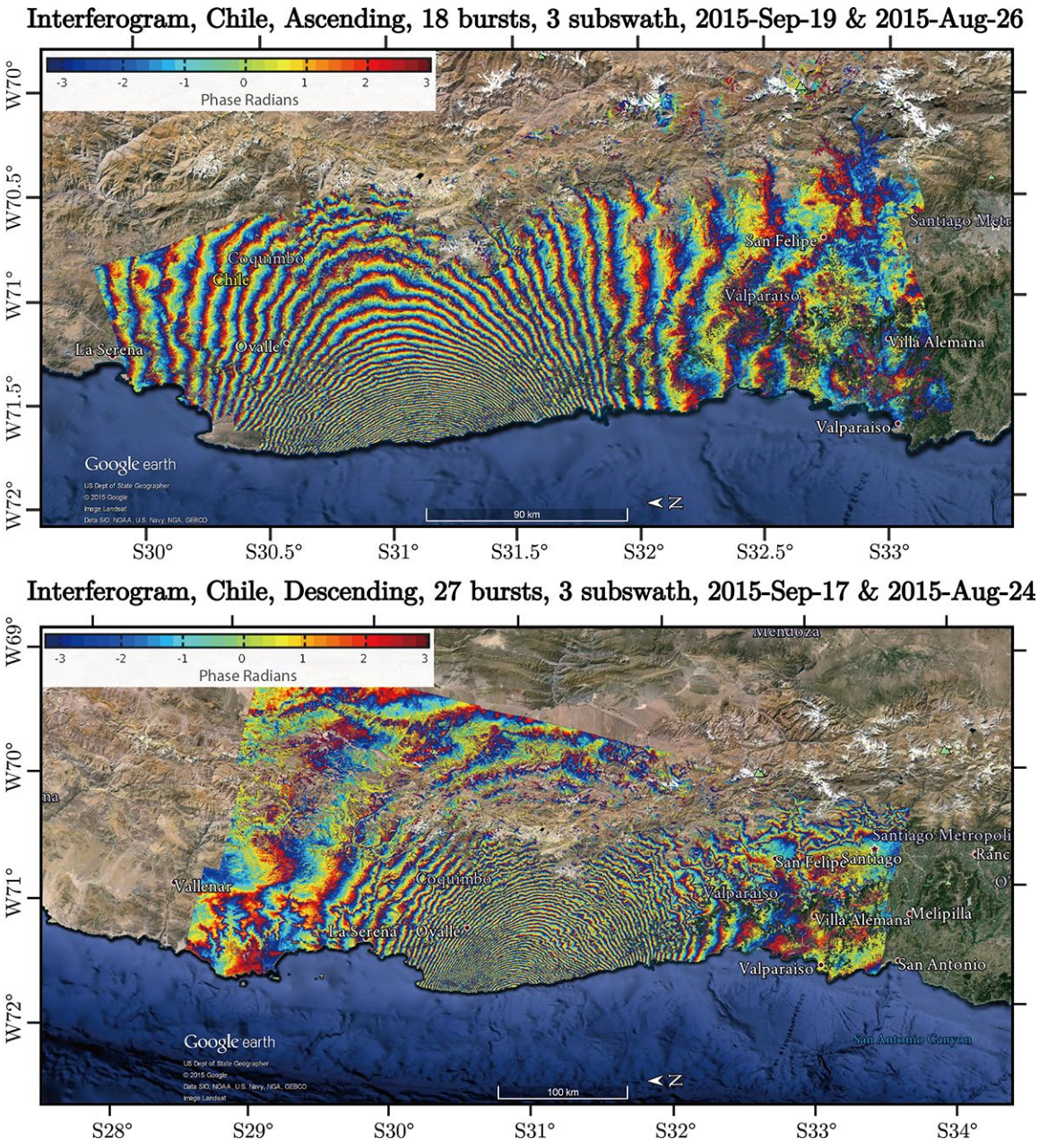

Fig. 4.11. The interferograms for the 2015 Illapel earthquake happened on the 16th of September in Chile with a magnitude of 8.3. Upper image: interferogram from ascending track, concatenating 2 SLCs on each date. Lower image: interferogram from descending track, concatenating 3 SLCs on each date.

km^2, and the Argentina capital city Buenos Aires 1,110 km away from the epic center could feel the the shake. In such cases, TOPS provided images from both ascending and descending tracks. By concatenating a couple of SLCs one is able to understand the full picture of this major earthquake and response promptly. Figure 4.11 presents two interferograms from two different tracks. The epic center of the earthquake could be quickly located at the center of the fringes, and by counting the number of fringes one could quickly understand the magnitude of the earthquake. More than dozens studies (or perhaps hundreds) have been carried out for this earthquake using Sentinel dataset.

4.7 Summary

This chapter proposed a "stripmap-like" and user-friendly interferometric processing flow for TOPS. Instead of a burst-wise processing chain, it is proposed to stitch the bursts into a continuous SLC image at the very beginning of processing chain. There are mainly two benefits behind this approach. In the first place, this approach enables a more user-friendly processing interface, especially for non-sar-expert who only wish to apply wide swath interferometry as a tool. In the second place, the proposed method would fit into an existing stripmap processing chain with all the TOPS related processing steps applied under the hood. Regarding the interferometric processing chain, a few key issues during the processing chain are addressed, and a quick implementation is demonstrated for the TOPS fine coregistration in the enhanced spectral diversity step without the need to resample the slave image for the second time. Two interferometric examples regarding TOPS and ScanSAR are shown with this processing chain. A simple MST graph approach for coregistering and updating a stack of S1 TOPS images is also introduced.

5. A COMMON INTERFEROMETRIC PROCESSING CHAIN FOR TOPS AND SCANSAR

5.1 Introduction

This chapter proposes to use the TOPS processing chain for another wide swath mode, the ScanSAR mode. TOPS processing chain is already discussed in the previous two sections. The same methodology could apply to ScanSAR system as well, since the two wide swath system shares a number of similarities.

This chapter is organized as follows. I will start by introducing the background and working mode of ScanSAR, followed by its impulse response function in azimuth direction. Then I will present each steps of how to apply the TOPS processing method to ScanSAR. At last some ScanSAR interferometric process examples are shown for the purpose of demonstrating the applicability of the processing flow.

5.2 Background of ScanSAR

ScanSAR system is the ancestor of TOPS mode. It is the first burst mode SAR system that switches between subswaths in range to expand the scanning area. It was first proposed in 1981 [3, 4], and was widely applied in a variety of sensors and missions. Among them were the Magellan imaging radar mission to Venus; the first and only scientific space-borne SAR system, SIR-C, that mounted all three bands (X/C/L) on board; then Radarsat, Envisat, TerraSAR-X and now ALOS-2.

The initiative of ScanSAR system is not for interferometry, and it is not until 1990s where Politecnico di Milano [5] and German Aerospace Center (DLR) [6] started relative work. Then the most famous ScanSAR interferometric application is the NASA operated SRTM mission in 2000, where the global topography was mapped

in a 11-days mission. The SRTM is still the most widely used DEM data in science community after almost 20 years.

ESA is the first to release ScanSAR SLC data in 2005 primarily used for interferometric purpose. However, despite the long history of ScanSAR mode interferometry, its scientific studies and applications are rather limited when comparing to stripmap mode. A few reasons are listed here. In the first place, ScanSAR system poses a more restricted burst synchronization requirement on interferometry. It has been explained in previous chapter that the TOPS system is more sensitive to azimuth spectral alignment, and it is the same for ScanSAR. Meanwhile, it requires very precise orbital control and bursts timing to achieve satisfactory burst synchronization. For older satellite systems such as Envisat, it remains a problem to control burst synchronization for delivering coherent interferometric products. In the second place, the first generation ScanSAR, such as Envisat ScanSAR, has a very low spatial resolution (15m by 80m), and this restricts the application scope for ScanSAR. At last, the process of ScanSAR is very different from conventional stripmap mode. It requires more complex processing flow than the stripmap processing chain. The imposed restriction of high quality data and the complexity of processing methods restrained people's familiarity to ScanSAR data processing and application.

The promotion of TOPS system by ESA brings wide swath mode back to popularity. TOPS solved most of the limitations of ScanSAR, mainly the burst synchronization, spatial resolution and amplitude scalloping effect. Now since TOPS is well known and well studied by more people, we are offered a new opportunity to go back and improve our understanding towards ScanSAR system. New satellite system such as ALOS-2 still use ScanSAR widely so it is still meaningful to study this system.

Although ScanSAR and TOPS works differently, they share a large portion of similarities, and their processing methodology could mostly be shared. I will describe the characteristics of ScanSAR, compare its similarity with TOPS and propose a common processing chain for the two working mode.

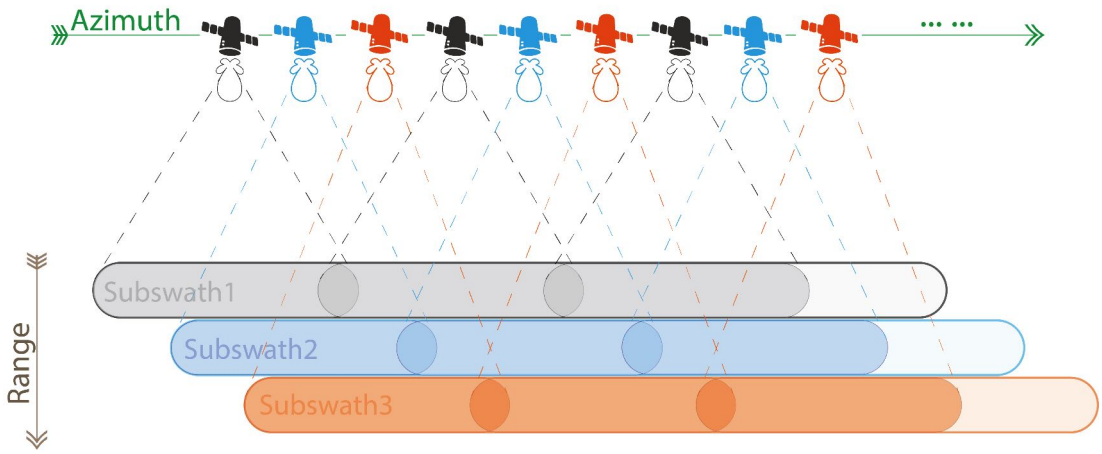

Fig. 5.1. A simplification of ScanSAR working mode with three subswath. Here the color is used to highlight the time period for scanning different subswath. Similar to TOPS, bursts in same subswath will have overlap area to make sure a continuous SLC could be stitched. The biggest difference between ScanSAR and TOPS is that ScanSAR do not steer antenna electronically in azimuth direction. Antenna beam pattern is only switched between subswath by adjusting the nadir angle.

5.3 Bursts Nature of ScanSAR

An illustration of ScanSAR working mode with three subswath is shown in figure 5.1. The first significant difference between ScanSAR and TOPS is that the antenna beam is not steered in azimuth direction in ScanSAR mode. At the very beginning, by adjusting the nadir angle, the antenna scans the first subswath for a certain time period. During the scanning in one subswath, the sending/receiving of pulses is identical to the stripmap case. This process is colored as the first black satellite in azimuth in figure 5.1. Then, the satellite adjusts the nadir angle and starts to scan the second subswath for another certain time period. This process is colored as the first blue satellite. Then the third subswath, as colored in orange. After all subswath are scanned, the satellite switches back to the first subswath and scans the second burst. This cycle continues as the satellite flies along. Similar to TOPS, the time period for scanning each burst is carefully calculated so that there are enough overlap area

for stitching the bursts into a continuous SLC image. Note that it is not necessary to follow the sequence of subswath 1 to 2 to 3. For example, in Envisat ScanSAR system, there are typically five subswath, and the scanning sequence is 1, 3, 5, 2, 4 and then back to 1.

The scalloping effect of ScanSAR is explained in figure 5.2. In stripmap mode, every target on the ground is illuminated by the full antenna pattern, which has the shape shown in figure 5.2(a) and shaded in green. In ScanSAR mode, every target is only illuminated by part of the full antenna pattern, because during the other time period the antenna is switched to another subswath for scanning. Figure 5.2(c) shows the case of Envisat ScanSAR, where each target will be illuminated three times. This means that the same target will appear in burst 1, 2 & 3 but at different positions with difference amplitude gain. This is usually referred as three looks. Note that for the target that appears at burst edges, the received echo from the target will have the minimum gain and minimum SNR. This is referred as the scalloping effect. As a comparison, it could be seen in figure 5.2(b) that in TOPS mode all targets are illuminated by the complete antenna beam pattern, thus the scalloping effect in TOPS mode is minimized. The only difference between tops and stripmap is that tops scans a target for a shorter time period, and thus smaller azimuth bandwidth.

At last, in both ScanSAR and TOPS system, the beam center crossing time (time of the amplitude gain peak) is generally not equal to zero doppler time, which means an additional doppler centroid will be introduced to their impulse response function in azimuth direction (figure 5.2(b) and 5.2(c)).

5.4 ScanSAR Impulse Response Function

ScanSAR and TOPS share a lot of similarities. In the first place, both system works almost the same in range direction as the stripmap mode. There is a minor and negligible modulation in range in TOPS mode; for ScanSAR system the signal direction in range direction should be equivalent to stripmap. Hence all the discussion

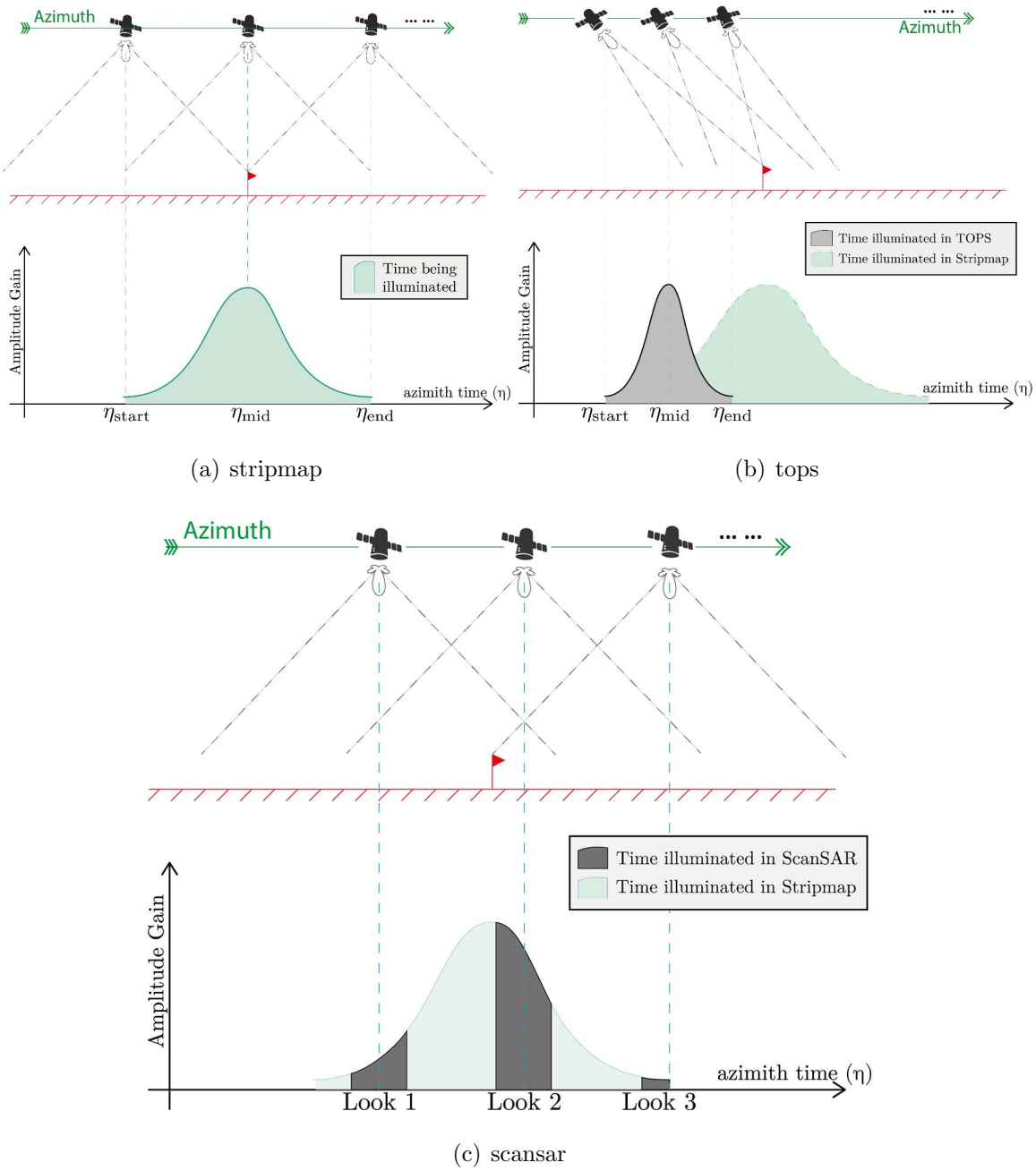

(a) stripmap

(b) tops

(c) scansar

Fig. 5.2. The illustration of the working mode for stripmap, tops and scansar and the amplitude gain as a function of azimuth time for one point target on the ground. In figure (b) and (c), the green color represents the time period that the given target on the ground (labelled in red) in scanned under TOPS or ScanSAR modes, and the grey color is the stripmap mode as reference.

below regarding ScanSAR will be focused in azimuth direction. In the second place, both system sacrifice azimuth bandwidth for a larger scanning range. In the third place, both IRF in azimuth direction could be considered as SAR signal system in presence of the squint, so that their IRF should be identical. As an example, for the ESA focused Envisat ScanSAR SLC product, the IRF on azimuth direction is [74]:

$$\begin{aligned} s(\eta) = s_a(\eta - \eta_c) \cdot \exp\Big\{ -j \cdot \frac{4\pi}{\lambda} \cdot R_0 \Big\} \\ \cdot \exp\big\{ j \cdot 2\pi \cdot K_a \eta_c \cdot (\eta - \eta_c) \big\} \\ \cdot \exp\big\{ j \cdot \pi \cdot K_a \cdot (\eta - \eta_c)^2 \big\} \end{aligned} \tag{5.1}$$

If one compare this equation to IRF of TOPS as in equation 2.1, it could be seen that the two IRF shares a striking resemblance. The only differences are: (1) In ScanSAR's IRF the envelop is centered at η_c. This is the mathematical expression for the scalloping effect, as we can see that the targets at burst edges will have smaller amplitude value since $s_a(\cdot)$ is usually a sinc$(\cdot)$ function; (2) In TOPS system the azimuth FM rate is represented as K_t where its derivation is given in [33], but in ScanSAR system the azimuth FM rate is represented using K_a to show distinction. K_a is the azimuth FM rate also in the stripmap mode. Except these two points, the rest are the same. This similarity determines that the processing flow for the two systems could be used interchangeably.

5.5 Applying TOPS Processing Chain to ScanSAR SLC

The complete ScanSAR processing chain is given in figure 4.3. The process is firstly designed for TOPS but it will be shown here that the same chain could serve also for the purpose of ScanSAR interferometric process.

5.5.1 Stitching Bursts

A typical ScanSAR burst is much shorter than TOPS burst. For example, one burst in Envisat ScanSAR consists of 48 lines. In the meta data, the zero doppler

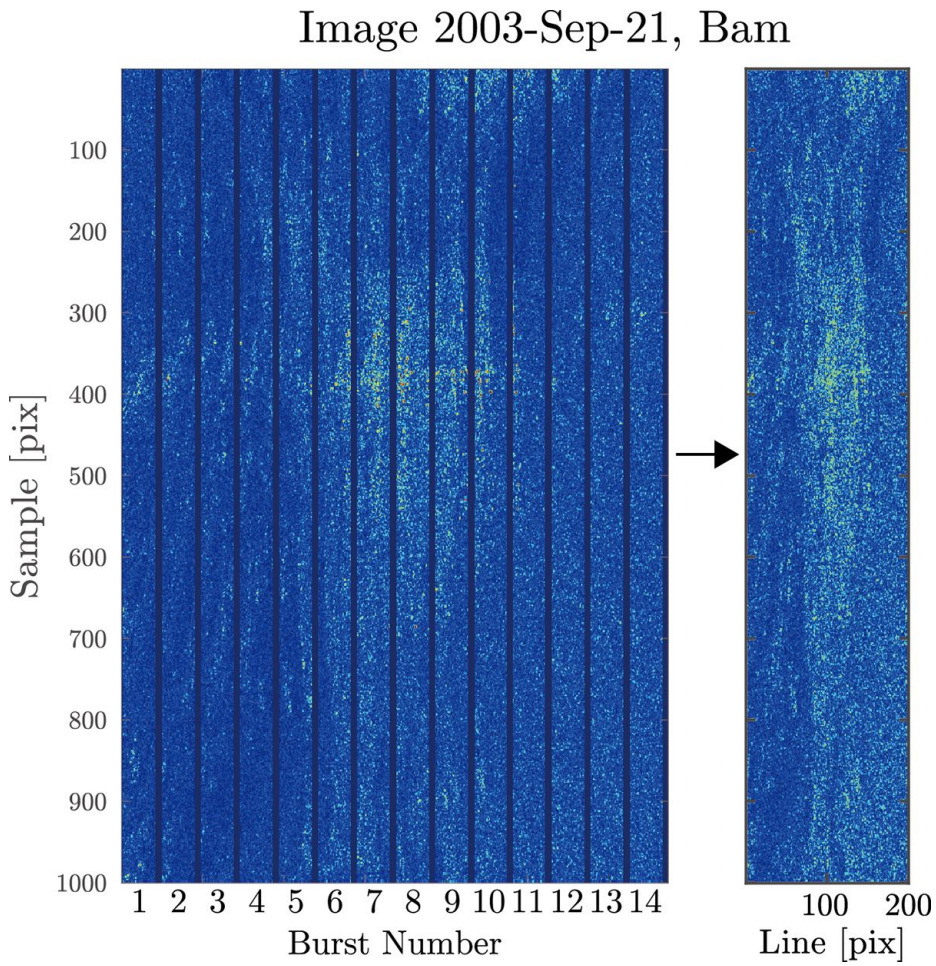

Fig. 5.3. An example of the Envisat ScanSAR burst mode image and after the bursts are stitched together into a continuous SAR image. Left: 14 bursts of the city of Bam. Each burst is 48 lines. The system is three looked so that one target will appear in three adjacent bursts. Specifically, one target will appear at the right edge of the first burst, the middle of the second burst and the left edge of the third burst. Right: the continuous SLC image after stitching the 14 bursts together. The bright area in the center of the image is the city of Bam, Iran.

azimuth time for each line will be given and is used for stitching together the bursts using the method described in section 4.4.1.

Envisat ScanSAR system is three looked. Multilooks in ScanSAR system is the guarantee to a continuous SLC after stitching. Combining multi looks could also

reduce the scalloping effect. Theoretically, a three-look system with 48 lines means that one could stitch the SLC using either the first 16 lines, the middle 16 lines or the last 16 lines. However, different from the case of TOPS, where one can stitch using either looks, it is suggested to always use the middle 16 lines for stitching purpose. The reasons are:

1. Due to the scalloping effect, the lines in the middle have highest SNR and the lines at the edge have the lowest SNR. For interferometric purpose, it is proposed to select the lines with higher SNR and hence higher coherence;

2. There are always a few lines at the very edge with zero value. For Envisat ScanSAR, approximately 8 out of the 48 lines are zero-padded data so that the size of bursts are consistent. If one stitches using the first or last 16 lines, then the lines with zeros will show up in the stitched SLC.

5.5.2 Deramp

Again, to comply with Nyquist sampling theorem, ScanSAR IRF need to be deramped to baseband before doing the resampling process in coregistration. Note that since Envisat ScanSAR system is not total zero-doppler steered, thus for resampling purpose one need to remove both the quadratic phase and the linear modulation phase when deramping. The proposed deramping process is the following:

$$s(\eta) \cdot \exp\left\{ -j \cdot \pi \cdot K_a \cdot (\eta - \eta_c)^2 \right\} \cdot \exp\left\{ -j \cdot \pi \cdot K_a \eta_c \cdot (\eta - \eta_c) \right\} \tag{5.2}$$

Figure 5.4 shows the deramping process of a sample burst from the same data in figure 5.3. Figure 5.4(a) & (c) is the azimuth spectrogram and spectrum before deramping. The azimuth bandwidth is much higher than the system PRF, thus the spectrum is under-sampled and severely aliased. Figure 5.4(b) & (d) is after applying the deramping function using equation 5.2. The azimuth bandwidth become baseband and is limited to PRF. Remember that in TOPS system the PRF (486Hz) is

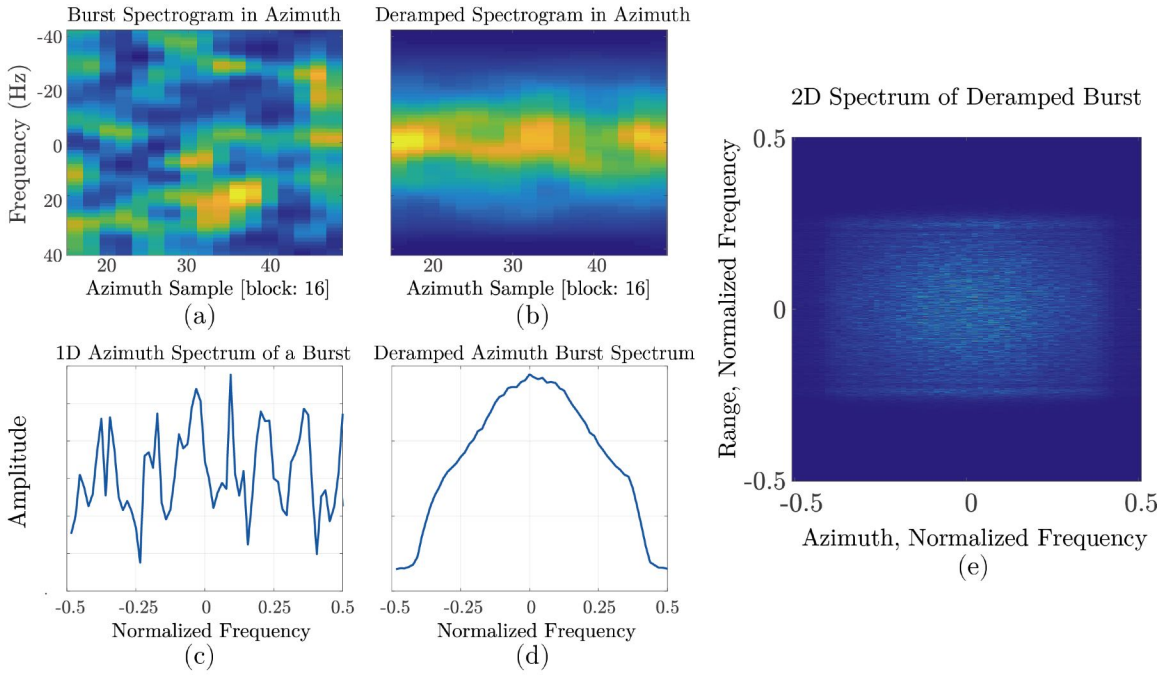

Fig. 5.4. The spectrum and spectrogram on azimuth direction for one single burst of Envisat ScanSAR. The spectrograms are calculated in blocks of 16 pixels and steps of 2 pixels. Upper left: the spectrogram in azimuth for one burst. Lower left: the 1D azimuth spectrum (averaged) of a burst. Upper middle: the spectrogram in azimuth after applying the deramping function. Lower middle: the 1D spectrum of the burst after deramp. Right: the 2D frequency domain plot of the deramped burst.

significantly higher than azimuth bandwidth (∼300Hz), so that there is some tolerance if the doppler centroid is shifted by a little. Here it can be seen in figure 5.4(b), (d) & (e) that the PRF is just right above the azimuth bandwidth with almost no margin left. This means that one need to know (or estimate) precisely the doppler centroid and make sure that the azimuth spectrum is totally baseband and aliasing-free before resampling process.

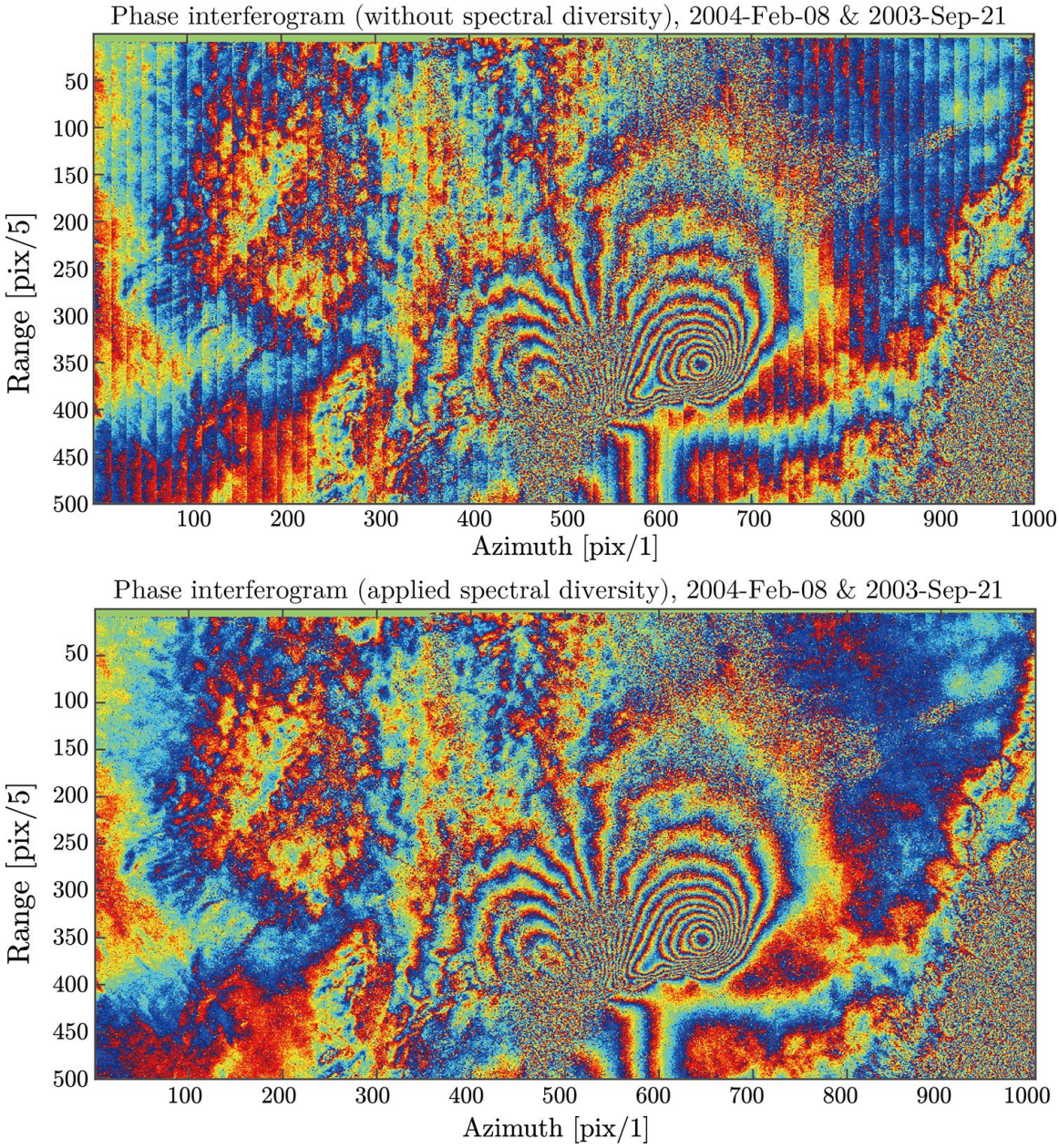

Fig. 5.5. Upper: The final interferogram (multi-looked by 5 in range direction) without performing the ESD correction. Lower: the interferogram after performing the ESD correction.

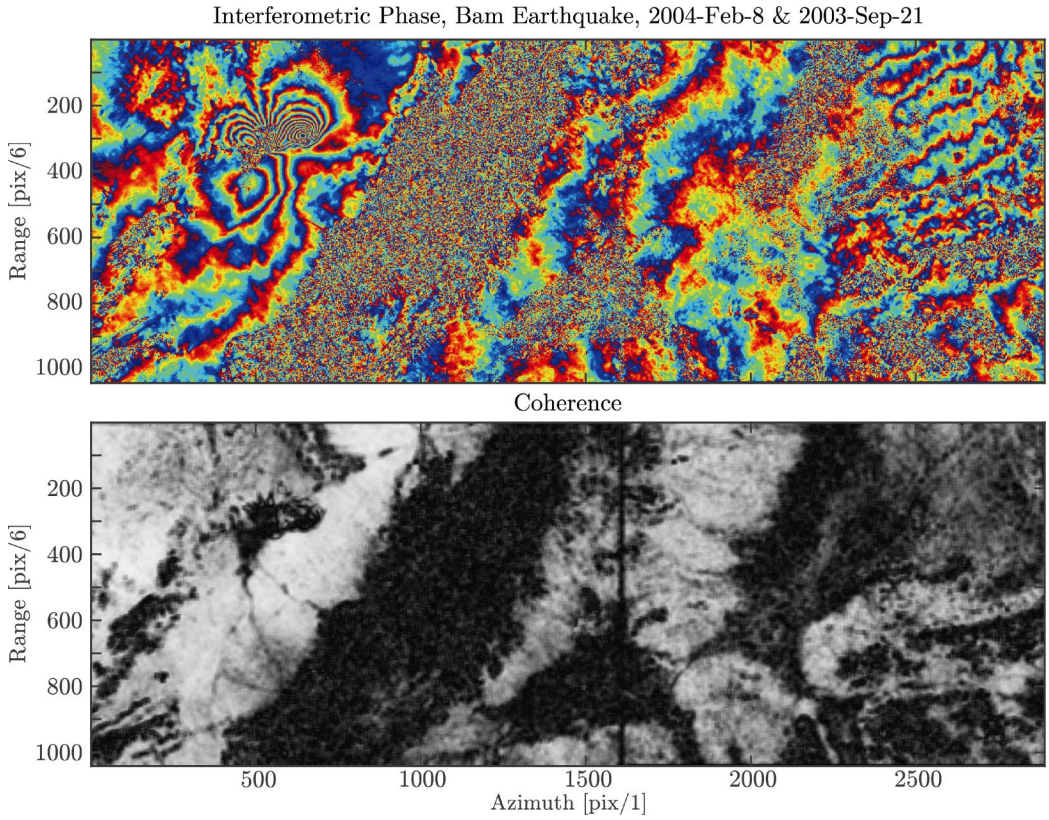

Fig. 5.6. Interferogram and coherence map for a pair of Envisat ScanSAR images showing the Bam earthquake happened on the 26th of December, 2003. The example contains a full subswath.

5.5.3 Coregistration, Reramping and Enhanced Spectral Diversity

The coregistration, reramping and ESD steps are really just replicates of TOPS case. The steps are identical to TOPS case and will not be discussed here furthermore. It is only worth mentioning that due to the presence of the quadratic phase term that exceeds the PRF, ESD is also a must for a ScanSAR system [44]. Figure 5.5 shows the interferometric with and without applying the ESD.

5.6 Example

In this section one pair of ScanSAR interferometric products are processed after implementing the ScanSAR processing chain. The fringe is shown in figure 5.6 and it records the Bam earthquake happened on the 26th of December, 2003 with magnitude 6.6. The master and slave images are taken on the 21th of September, 2003 and 8th of February, 2004 respectively. Despite of the large temporal baseline, a good burst synchronization (91% [75]), a small normal baseline (137 m) and the fact that the AOI is located at a deserted area all reduced other correlation factors. The interferogram is multilooked by 6 in range direction so that the resolution on two directions are similar. The azimuth resolution is 80 m. The earthquake pattern is explicitly revealed by the interferogram.

5.7 Summary

This chapter proposed to use the TOPS processing chain for ScanSAR interferometric process. The reason that this could work is due to the resemblance between TOPS and ScanSAR IRF in azimuth direction. Some key steps in ScanSAR processing are discussed in this chapter such as stitching bursts and burst deramping. The trivial difference between TOPS and ScanSAR mode is also presented. At last, one example of Envisat ScanSAR interferogram is shown to demonstrate the applicability of applying TOPS interferometric processing flow to ScanSAR system.

6. A PRACTICAL APPLICATION WITH S1 TOPS AND TIME SERIES ANALYSIS

6.1 Introduction

After all the methodologies and processing flows from previous chapters, a case study is presented in this chapter. For the purpose of demonstrating the large coverage and rich dataset of S1, a relative large area of interest, the San Joaquin Valley, is selected for estimating the velocity of ground subsidence for a period of three years with the time series analysis. This chapter will start with a very basic introduction of time series analysis methods. The study area of interest will then be introduced. The results will be presented at last.

6.2 Methodology

In this section, the very basic and necessary details in InSAR and time series analysis is presented. More details could be find in [76].

6.2.1 SAR Interferometry

As shown in equation 2.1, the phase can be defined as a function of the target distance from the sensor (in the following discussion, without loss of generality, the doppler centroid is all assumed to be zero):

$$\phi = \frac{4\pi}{\lambda} R \tag{6.1}$$

The interferogram is the difference of the master and slave image phase. Written in math, it is the conjugate multiplication of complex two dimensional arrays between

coregistered master and slave image. Denoting the master image as I_{M} and slave image as I_{S}, the interferogram is

$$\mathrm{Ifg} = I_{\mathrm{M}} \cdot I_{\mathrm{S}}^{*} \tag{6.2}$$

where Ifg means the interferogram. While the conjugate multiplication gives a complex array containing magnitude and phase, only the phase of the interferogram is used for quantifying displacements. The magnitude, if filtered, is what known as the spatial coherence. With reference to equation 6.2, the interferometric phase can be written as the phase difference between the two acquisitions:

$$\Delta\phi_{\mathrm{M,S}} = \frac{4\pi}{\lambda}(R_{\mathrm{M}} - R_{\mathrm{S}}) = \frac{4\pi}{\lambda}\Delta R \tag{6.3}$$

This is the simplified but famous equation of how interferogram works: if a target moves away from the satellite a distance of ΔR between the master and slave acquisition time, it will be reflected to the interferogram as a phase change of $\Delta\phi$. The SAR satellite system is able to measure $\Delta\phi$ and derive ΔR from it. An illustration of this is shown in figure 6.1. The illustration also explains that the sensitivity of SAR measurement is independent of the distance and is proportional to wavelength.

Under actual conditions, the path difference, ΔR, is a combination of several factors, including sensor-target distance change, variations in the atmospheric water vapor content at the time of master and slave image acquisitions, etc. In particular, the sensor-target distance can be affected either by a different acquisition geometry or by a target displacement. These factors, representing target displacement, terrain topography, atmospheric delay, and signal noise, are summed up as follows:

$$\Delta\phi = \Delta\phi^{\mathrm{displacement}} + \Delta\phi^{\mathrm{height}} + \Delta\phi^{\mathrm{flatten}} + \Delta\phi^{\mathrm{atmosphere}} + \Delta\phi^{\mathrm{noise}} \tag{6.4}$$

The objective of InSAR analysis is to extract the term $\Delta\phi^{\mathrm{displacement}}$ by removing the other phase terms. A high-resolution DEM can be used to estimate and remove $\Delta\phi^{\mathrm{height}}$, and a high resolution orbital state vector can be used for $\Delta\phi^{\mathrm{flatten}}$ term. There is no practical way to estimate the atmospheric contribution based on only a few interferograms, however, time series analysis (TSA) involving at least 20 images can be used to filter out random effects of the atmospheric delay.

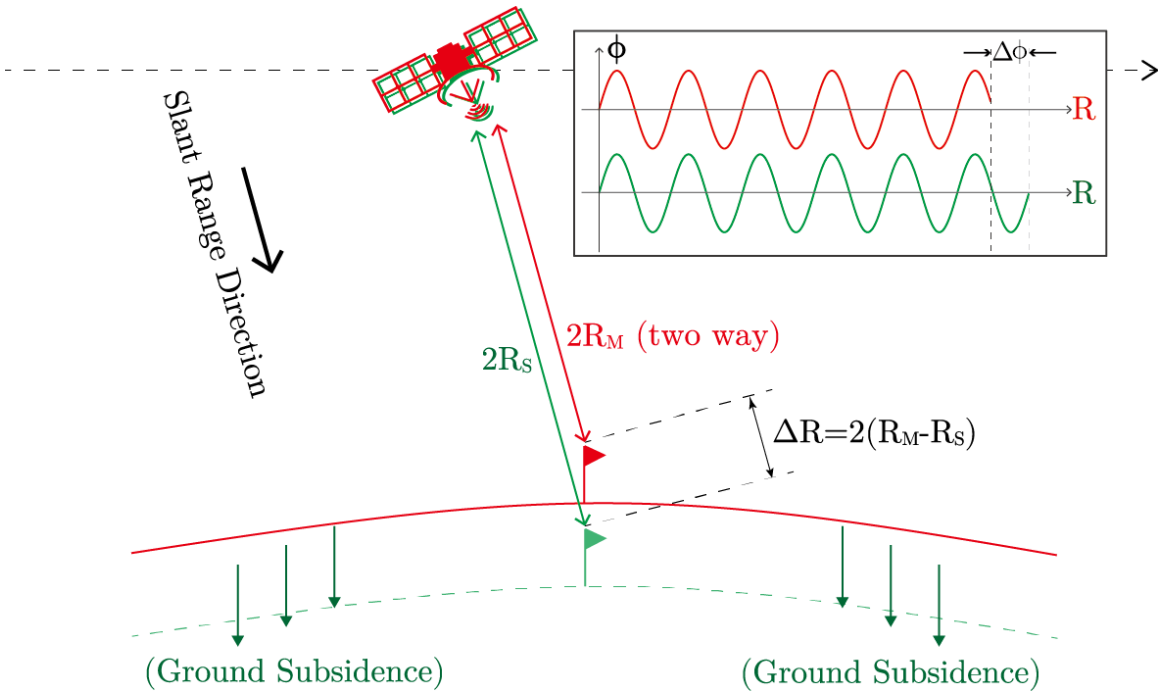

Fig. 6.1. A simple illustration of InSAR principle. A ground movement is measured by means of measuring the phase difference.

6.2.2 Time Series Analysis

In early 2000's, The Politecnico di Milano proposed the persistent scatterer interferometry (PSI) technique [77]. PSI is based on the idea that analyzing a long series of SAR images makes it possible to identify targets that do not change their electromagnetic signature throughout the entire dataset (referred as the persistent scatterers, or PS). Such targets are not affected by temporal or geometric decorrelation. Their phase can be quantified as a function of the acquisition parameters (normal and temporal baseline). By analyzing these PS points, it is possible to observe that height, displacement, and atmospheric delay show different spectral characteristics as a function of normal and temporal baseline and as a function of space. Therefore, the separation and estimation of various phase components is possible through the time series analysis.

Phase Equation PSI is a relative measurement technique. All the calculated parameters (height and velocity) are relative to some stable reference point contained within the AOI. Now I will briefly illustrate the basic idea of time series analysis. The objective of PSI is to estimate the height and relative displacement of targets. By selecting a stable reference point among various targets of interest and analyzing the interferometric phase of a selected point p, equation 6.4 can be expressed as follows:

$$\Delta\phi_{i,k}(p) = \Delta\phi_{i,k}^{\text{displacement}}(p) + \Delta\phi_{i,k}^{\text{height}}(p) + \Delta\phi_{i,k}^{\text{flatten}}(p) + \Delta\phi_{i,k}^{\text{atmosphere}}(p) + \Delta\phi_{i,k}^{\text{noise}}(p) \tag{6.5}$$

where the indices (i, k) denote the interferometric image couple, with k being the master image and i representing generic image of the dataset. The interferometric phase terms consist of the following contributions: displacement, height, flat terrain, atmospheric delay, and signal noise.

Height Term In the first place, the flat terrain term can be estimated from the orbital data. The height term has a linear relationship to the normal baseline, which can be rewritten by making explicit the dependency of the height $\Delta h(p)$ on the target of interest p and the dependency of the normal baseline $B_n^{(i)}$ on the i^{th} image of the dataset (the notation Δ is used here to denote the height difference between reference point o and given point p):

$$\Delta\phi_{i,k}^{\text{height}}(p) = \frac{4\pi}{\lambda} \cdot \frac{B_n^{(i)} \cdot \Delta h(p)}{R_k \cdot \sin\theta_k(p)} \tag{6.6}$$

Since λ, $\theta_k(p)$ and R_k are all known constants and do not vary with respect to different slave images, thus they can be grouped into a single constant, as follows:

$$\Delta\phi_{i,k}^{\text{height}}(p) = C_h^{(i)} \cdot B_n^{(i)} \cdot \Delta h(p) \tag{6.7}$$

where $C_h^{(i)}$ is a constant and $\Delta\phi_{i,k}^{\text{height}}$ is a function of spatial baseline $B_n^{(i)}$ and target height $h(p)$.

Displacement Term A common way to model the displacement term is to assume that it is linear over time. $\Delta v(p)$ is defined as the relative velocity of point p with

respect to the reference. $B_t^{(i)}$ represents the temporal baseline between the master and slave image, resulting in the expression for displacement defined as follows:

$$\Delta\phi_{i,k}^{\text{displacement}}(p) = \frac{4\pi}{\lambda} \cdot B_t^{(i)} \cdot \Delta v(p) = C_v^{(i)} \cdot B_t^{(i)} \cdot \Delta v(p) \tag{6.8}$$

which basically states that the displacement equals to the product of time and velocity.

Atmosphere Term The fourth term in the phase equation represents the atmospheric delay. The atmospheric delay has a decorrelation range of several hundred meters. In PSI analysis, one will construct a graph connecting only close points so that this term is negligible. Then for estimating the height and velocity of all points with respects to only one reference point, a graph inversion will be applied in ways such as least square. For the purpose of illustrating the basic idea of time series analysis this term is put aside in the following discussion.

Noise Term The noise term in equation 6.4 is estimated from model residuals. It is a good indicator of target point stability and reliability.

Estimating Height and Velocity: an Optimization Problem There are 5 unknown terms to solve in equation 6.4. The flat terrain could be solved in the first place, and atmospheric terms can be considered negligible for points close to each other, leaving the displacement, the height and the noise terms to consider. Under such consideration, after each term $\Delta\phi_{i,k}(p)$ is examined for the generic point p inside a small area, the problem reduces to a set of $N-1$ equations where N is the number of images, and the unknowns are height $\Delta h(p)$ and velocity $\Delta v(p)$ in the linear space $(B_n^{(i)}, B_t^{(i)})$.

The set of N-1 equations cannot be solved by the least square approximation method because the phase $\Delta\phi$ is wrapped to $[0, 2\pi)$, thus making it a non-linear system. The workaround is to use optimization algorithms. The proposed solution involves the maximization of the periodogram in which height and velocity represent

2-dimensional frequencies to be scanned [77]. To illustrate this concept, equation 6.4 can be rewritten as follows:

$$\Delta\phi_i = C_h^{(i)} \cdot B_n^{(i)} \cdot \Delta h + C_v^{(i)} \cdot B_t^{(i)} \cdot \Delta v + \Delta\phi_i^{\text{noise}} \tag{6.9}$$

The objective is to find a set of $(\Delta h, \Delta v)$ such that for each image i and given $\Delta\phi_i$, the total noise term $\Delta\phi_i^{\text{noise}}$ is minimized. Since the phase is periodic, which means that radiance 2π is equivalent to radiance 0, the problem cannot be simplified by minimizing $\sum \Delta\phi_i^{\text{noise}}$. Instead, the solution is to maximize the following term:

$$\frac{1}{N-1} \sum_{i=1}^{N-1} \exp\{j\phi_i^{\text{noise}}\} \tag{6.10}$$

where $1/(N-1)$ is the normalization factor. If there is no noise (in a perfect idealized situation) this value will reach its maximum at 1. To express equation 6.10 in a more rigorous form, the periodogram $\xi(\Delta h, \Delta v)$ is defined as follows:

$$\xi(\Delta h, \Delta v) = \frac{1}{N-1} \sum_{i=1}^{N-1} \exp\left\{ j\left(\Delta\phi_i - C_h^{(i)} B_n^{(i)} \Delta h - C_v^{(i)} B_t^{(i)} \Delta v\right)\right\} \tag{6.11}$$

This expression is equivalent to equation 6.10. The solution is provided by $\xi(\Delta h, \Delta v)$ that maximizes the absolute value of the periodogram. Mathematically, it can be expressed as follows:

$$(\Delta\hat{h}, \Delta\hat{v}) = \arg\max\left(\left|\xi(\Delta h, \Delta v)\right|\right) \tag{6.12}$$

The maximum absolute value of the periodogram is called the temporal coherence, defined as follows:

$$\xi(p) = \left|\xi(\Delta\hat{h}, \Delta\hat{v})\right| \tag{6.13}$$

Temporal Coherence Temporal coherence is a very important parameter for identifying persistent scatterers. It provides a measure of reliability of results. From the definition of temporal coherence, when the model driven by equation 6.12 matches the observed interferometric phase, the noise phase term $\Delta\phi_i^{\text{noise}}$ tends to zero, and the temporal coherence approaches 1. If the model does not match the observed phase,

the argument of the periodogram will be random and the temporal coherence will be low. When a target has low contribution from the noise term, good estimate of velocity and height can be determined, with the temporal coherence value approaching 1. On the other hand, when a target is not stable (e.g., vegetation, farm land), the phase of the target will appear to be random and the noise contribution to the phase term will be dominant. In this case it is difficult to arrive at a robust estimation of velocity and height since the temporal coherence will be close to 0. Therefore, the temporal coherence estimate can be used to determine if a potential target is actually a persistent scatterer. Implicit in the above considerations is the number of images N used in the analysis. Low number of images in a dataset will bias the temporal coherence to higher values, making it difficult to distinguish between stable and noisy points. In general, the more images, the better the estimate. The analysis becomes significantly more accurate as the number of available radar images increases.

6.3 Study Area of Interest

A brief introduction to the San Joaquin Valley Subsidence For this case study the California San Joaquin is selected. The San Joaquin Valley is part of the California Central Valley and is a very flat valley that dominates the geographical center of California. The Central Valley is 60 to 100 km wide and stretches approximately 720 kms from north to south. The valley is known as California's single most productive agricultural region and one of the most productive in the world, providing more than half of the fruits, vegetables and nuts grown in the United States. The agricultural relies heavily on the irrigation system. Despite the fact the valley is close to the sea, the state is famous for its semi-arid condition and suffers from droughts from time to time. The irrigation system thus depends heavily via an extensive system of reservoirs and canals, surface-water diversions and extensive groundwater withdrawal. This extensive withdrawal has caused water levels to decline on the west

side of the southern two-thirds of the Central Valley, also known as the San Joaquin Valley [78, 79].

The ground subsidence due to groundwater withdraw could be traced back to the 1920's. A famous photo shoot in 1977 [80] shows that one spot subsided almost 8.5 meters from 1925 to 1977. In drought seasons, over pumping groundwater for agricultural supply will lead to aquifer-system compaction. Another consequence is the land subsidence due to the permanent aquifer-system storage loss. Indeed, the recent drought in 2007-2009 and 2012-2015 has resulted in an alarming rate of subsidence, where the most critical places have reached 30cm-60cm per year. Until the current time the subsiding trend persists. It is critical to keep a close monitoring to the subsidence in real time.

Why I select this AOI The reason for picking this area as the studying site is for demonstrating the power of S1 in monitoring a large study area. The San Joaquin valley starts from Sacramento at north and stretches all the way to Bakersfield, the distance in north-south is almost 400 km, the distance in west-east could reach 150 km at most and the area is approximately 52,000 km^2. Only a wide swath system has the capability to monitor the entire area with only a few images (for the same date acquisition). As shown in figure 6.2, the three white rectangles represents the three subswaths in track 137 of S1 TOPS. For covering the entire San Joaquin Valley, 17 bursts (2 SLCs) from each subswath are stitched together. The middle and right subswaths could almost covers the entire valley. The large area of the San Joaquin Valley makes it a very good candidate to demonstrate the power of TOPS's wide coverage. As a comparison, the green footprint in the upper-left corner of S1 footprint in figure 6.2 is the footprint of a Cosmo Skymed X-band stripmap image. It could be seen that to monitor the same area, one would need almost 60 stripmap images to cover the same area in red rectangular box - which is the footprint of only 2 SLC images!

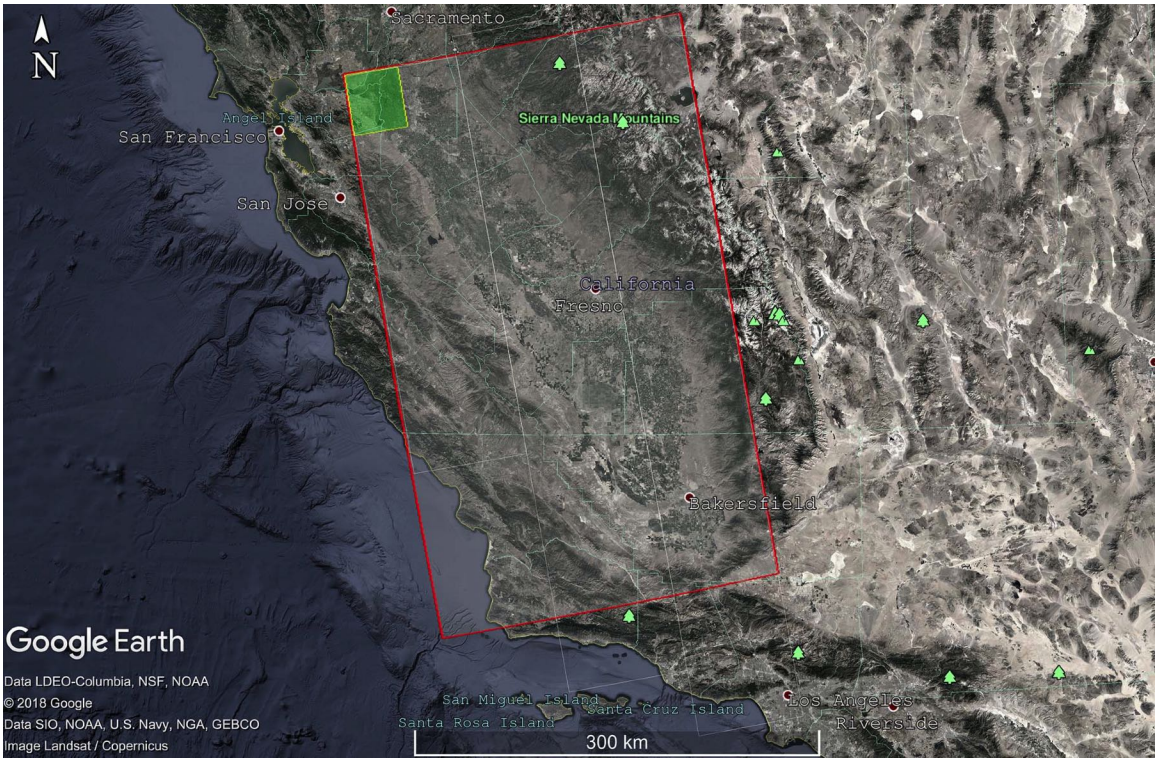

Fig. 6.2. The study area of interest is drawn in the red-outlined rectangle. The three white-outlined footprints are the three different subswaths that belongs to track 137. The yellow-outlined with green-background box at the upper-left corner of AOI represents a typical footprint of COSMO stripmap full frame. The dataset concatenates 2∼3 SLCs on azimuth direction so to get a larger area.

Dataset In this case study, both descending and ascending track are used for the analysis. Figure 6.2 shows the footprint in the ascending track.

For ascending track 137, a total of 175 SLC data from 55 different dates were used for the analysis. Images on the same dates are easily concatenated on azimuth direction due to the way TOPS acquires data. Each subswath have 17 bursts. The dataset is from April 2015 to April 2017. The majority temporal baseline of the dataset is 12 days. For descending track 144, a total of 215 SLC data from 69 different dates were used, spanning from November 2014 to September 2017. Each subswath have 15 bursts for covering the entire valley.

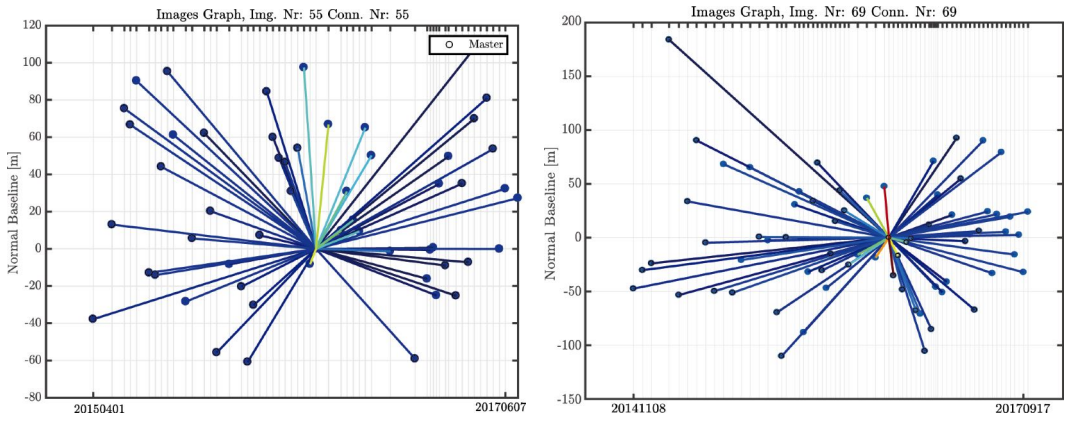

(a) Ascending (b) Descending

Fig. 6.3. A plot of ascending and descending S1 dataset used in this case study. The x-axis is the temporal baseline and the y-axis is the spatial baseline. The plot is also a demonstration of the good orbital control of S1.

6.4 Results

6.4.1 Interferograms

Four interferograms taken from the middle subswath of the ascending track are shown in figure 6.4. The purpose is to show the temporal decorrelation of the San Joaquin Valley. As a heavily vegetated area, the temporal decorrelation become quite obvious after 24 days and become almost totally noisy after 84 days. At this moment, only the S1 system could provide such rich dataset with an average 12 days revisit time. And only with such rich dataset and small temporal baseline (not to mention the small spatial baseline contributes to the coherence as well) could one perform a PSI analysis successfully in such heavily vegetated area.

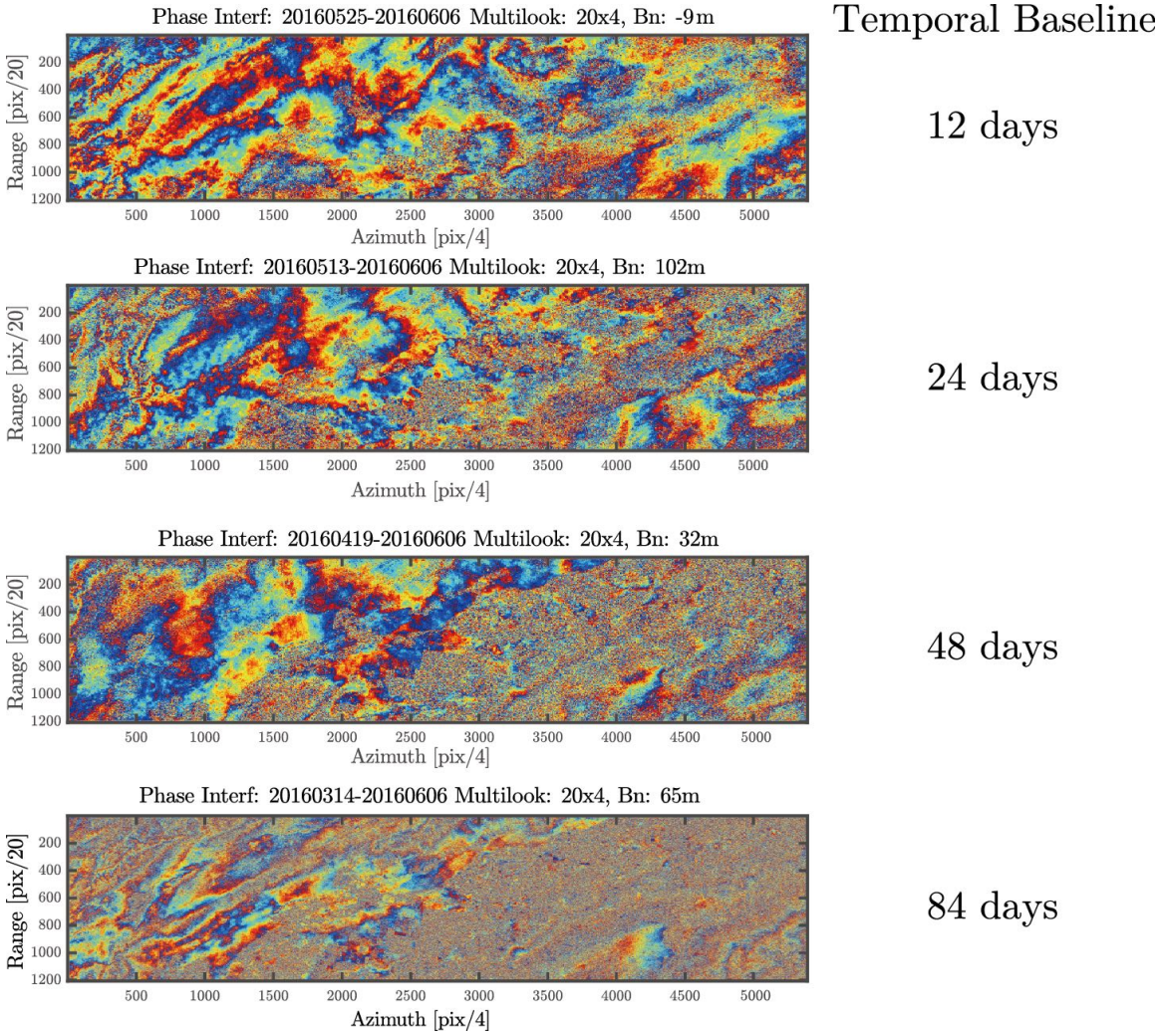

Fig. 6.4. Four interferograms from the middle subswath of ascending track. The temporal baseline increases from 12 days to 84 days. The interferometric coherence decrease exponentially as a function of time. In this AOI that is heavily vegetated, the interferogram is almost totally noisy after 84 days.

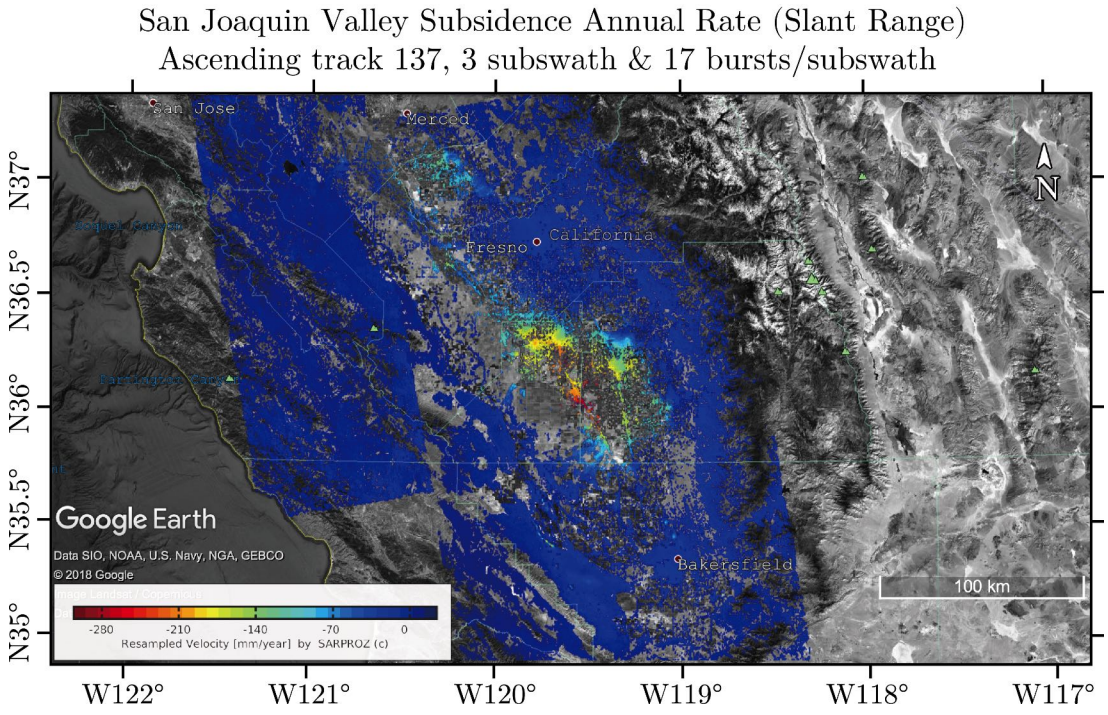

(a) Ascending

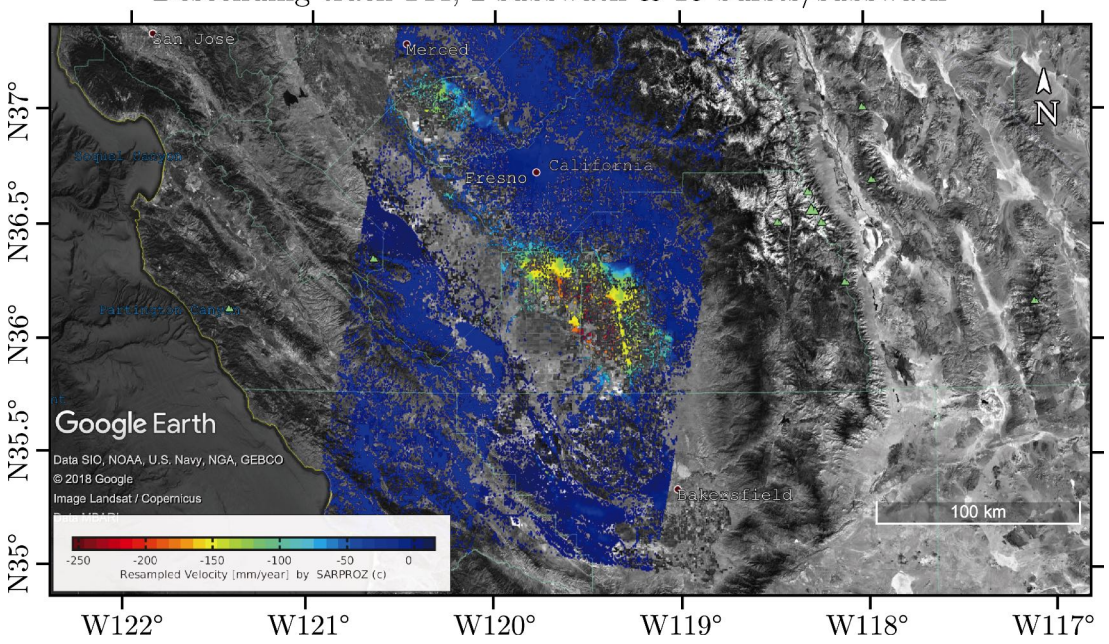

(b) Descending

Fig. 6.5. The annual subsidence rate projected to slant range direction in ascending and descending track with PSI analysis.

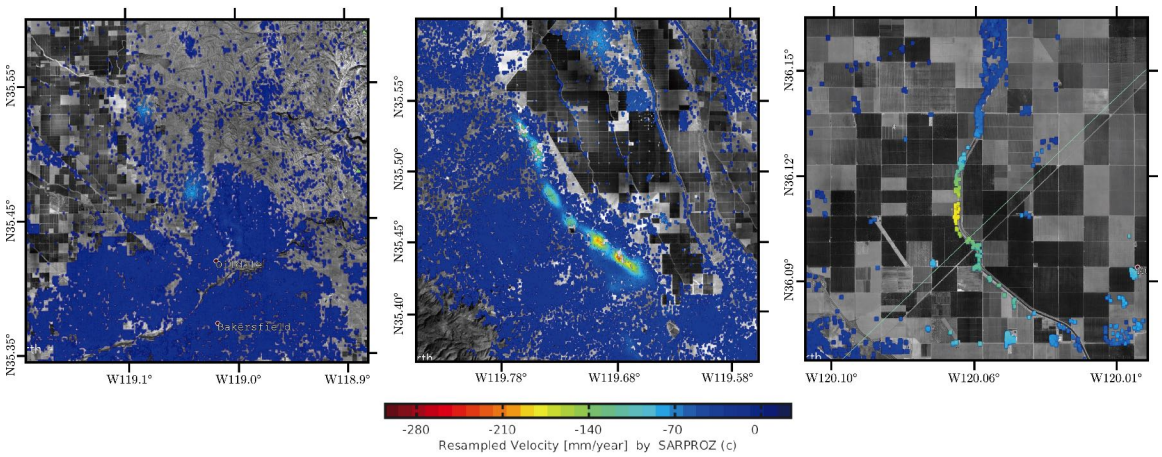

Fig. 6.6. Examples of local subsidence rate. Left: an oil field just to the north of Bakersfield. Middle: subsidence of an oil and gas fields. Right: subsidence of a section of roads.

6.4.2 Time Series Analysis Results

The PSI analysis method that is described in the previous section is used for the time series analysis. With the rich S1 dataset, it is proposed to simply use the star graph configuration for the time series analysis. The result is shown in figure 6.3.

The most severe subsidence zone could be found between Fresno and Bakersfield. The "red" subsidence zone could be clearly observed from both tracks and the annual velocity reaches almost 300 mm/year in satellite slant range direction. Translating to vertical subsidence, this could mean a rate of almost 400 mm/year. Another subsidence zone that is less severe could be found at the north of Fresno, where the maximum velocity could reach approximately 100 mm/year in slant range direction. The two subsidence zones have existed for a long time [81]. The newest data from S1 shows that those areas are keeping the subsiding rate with no signs of stopping. The major cause of the subsidence is the lasting drought and the exceeding extraction of ground water due to the drought [78, 79]. In addition, there are a number of oil fields located in the San Joaquin Valley. Oil fields are known for causing local ground subsidence. A few smaller subsidence zone could be found at the local oil fields. Two

examples are shown in the left and middle of figure 6.6. In fact, the subsiding zones shown in this section are all known in the past by other sensors [81–83]. The results from S1 only verified the subsiding is still ongoing.

One thing to notice is the discrepancy between the results from ascending and descending tracks. A couple of factors would contribute to this issue. In the first place, when there is not only vertical but also horizontal movement, the projection of movement to different tracks would be different. With two tracks one could potentially decompose the local movement into horizontal and vertical movement. It should also be noticed that the incidence angle varies with subswaths and tracks. The projection to different incidence angles would also be different. For the purpose of showing the subsiding trend it is enough to show the results as in figure 6.3, but for understanding better both the direction and velocity of the subsidence, one could combine results from two tracks and derive such results. In figure 6.2 one could see that the scatterers are sparser in the valley and denser in the surrounding deserted and mountainous area. In spite of S1's rich dataset that decreased the temporal decorrelation, since a star graph is used in the PSI analysis, such vegetated area as this AOI still restricts the availability of coherent persistent scatterers. This is a known limitation to PSI analysis in vegetated area. The approach to work around this limitation is the small baseline subset method. In the small baseline method, one will use a small-baseline graph instead of the star graph to increase coherence. However, one should be careful with the combination of such method and S1 dataset. S1 data have rather small baselines even after ESA relaxed the restriction of S1's orbital tube exactly for the purpose of PSI analysis [27]. Such small baselines would introduce bigger error in height estimation. Using a small baseline approach means both small temporal baseline and small spatial baseline. If the parameters are not well estimated, the error would propagate in the graph inversion step and introduce significant bias to the final result. This is also why in the case study I start with the PSI analysis: a longer temporal baseline would make it more precise in estimating the velocity.

6.5 Summary

In this chapter, a case study for the subsidence in San Joaquin Valley, California is conducted. The basics of SAR interferometry and PSI analysis is introduced, followed by the PSI process results of S1 for San Joaquin Valley subsidence. The process result reveals several subsidence zones with alarmingly large subsiding rate. The case study is a suitable application with Sentinel-1 TOPS dataset, and it shows the proposed processing chain discussed in the previous chapters is applicable and practical.

7. SUMMARY

This thesis discussed and realized the complete Sentinel-1 wide swath interferometric processing workflow. A number of aspects are being thoroughly discussed, such as comparing the two different coregistration approaches, proposing the stripmap-like processing flow for TOPS and extending the TOPS workflow to ScanSAR. All the works were aiming at one goal, which is to realize a generalized and robust Sentinel-1 processing system that would serve better in applications in civil, earth observation and other practical fields. Specially, the significance of this work includes the following:

1. Proposed the feasibility of doing coregistration using the cross-correlation-and-linear-transformation method plus the enhanced spectral diversity. In addition, the quantified comparison between the cross-correlation coregistration method and the geometrical coregistration approach was presented. Coregistration is the most important steps in Sentinel-1 interferometric processing, however there are still doubts on what approach to use and what is the performance of each approach. In this work the advantages and disadvantages of each approach are carefully evaluated, and the scenarios for where each approach works best are studied;

2. Proposed a stripmap-like processing flow for Sentinel-1 TOPS. While some of the existing platforms process TOPS data bursts by burst, the author proposed to stitch the bursts at the very beginning to get a stripmap-like SLC image. The most important reason is to fit the TOPS processing flow to the existing and mature stripmap processing platform. Since the ultimate aim of the research is to serve for applications, the idea is also to provide user friendly processing interface and processing flow. The proposed workflow will give the

users the identical interfaces and products as in processing the stripmap mode with all the wide-swath related processes implemented under the table. With the realization of this workflow, any non-SAR-experts working on their applications with minimum InSAR knowledge would be able to process and analyze S1 TOPS data without learning the complex theories behind TOPS;

3. Extended the TOPS processing chain to the ScanSAR system. ScanSAR system is still widely used, thus it is still useful to adopt the aforementioned two proposals to the ScanSAR processing chain as well. This work started with EnviSAT ScanSAR system and presented the feasibility of sharing the processing flow between TOPS and ScanSAR system;

4. Experimented with the TOPS processing chain for the time series analysis in the California Central Valley. The experiment is a demonstration of how one can use the TOPS rich dataset and large coverage to monitor a very large area with satisfactory results.

All of the proposed methodologies and process workflows are validated with large amount of real data so that the work is practical and applicable. In addition, the content of this thesis is implemented as a processing package into an existing SAR/InSAR processing package, SARPROZ [66], and is open to the public users. The processing package is capable of processing S1 TOPS and Envisat ScanSAR. The development of this processing package is both for validating the robustness of proposed workflow and for utilizing the power of S1 dataset in real world applications. It should be worth mentioning that the processing package already helped other research groups with their own S1 dataset and AOI, and some of their works are already published [84–90]. The works from other groups are also approvals of this thesis, since successful applications of S1 TOPS interferometry in civil, earth observation and other aspects is the final goal of this work. The future work will also focus on the continuous development of wide swath processing chain.

REFERENCES

[1] T. G. Farr, P. A. Rosen, E. Caro, R. Crippen, R. Duren, S. Hensley, M. Kobrick, M. Paller, E. Rodriguez, L. Roth *et al.*, "The Shuttle Radar Topography mission," *Reviews of geophysics*, vol. 45, no. 2, 2007.

[2] I. G. Cumming and F. H. Wong, *Digital processing of synthetic aperture radar data: algorithms and implementation*. Artech house, 2005. [Online]. Available: https://books.google.com/books?id=e9xxQgAACAAJ

[3] K. Tomiyasu, "Conceptual performance of a satellite borne, wide swath synthetic aperture radar," *IEEE Transactions on Geoscience and Remote Sensing*, vol. GE-19, no. 2, pp. 108–116, 1981.

[4] R. K. Moore, J. P. Claassen, and Y. H. Lin, "Scanning spaceborne synthetic aperture radar with integrated radiometer," *IEEE Transactions on Aerospace and Electronic Systems*, vol. AES-17, no. 3, pp. 410–421, 1981.

[5] A. M. Guarnieri and C. Prati, "ScanSAR focusing and interferometry," *IEEE Transactions on Geoscience and Remote Sensing*, vol. 34, no. 4, pp. 1029–1038, 1996.

[6] J. Holzner and R. Bamler, "Burst-mode and ScanSAR interferometry," *IEEE transactions on geoscience and remote sensing*, vol. 40, no. 9, pp. 1917–1934, 2002.

[7] P. Guccione, "Interferometry with ENVISAT wide swath ScanSAR data," *IEEE Geoscience and Remote Sensing Letters*, vol. 3, no. 3, pp. 377–381, 2006.

[8] N. Miranda and P. Meadows, "ASAR wide swath burst synchronization data update," ESA, techreport, 2013. [Online]. Available: https://earth.esa.int/documents/10174/990529/ASAR_Burst_Synchronisation_Data_Update_2.1

[9] N. Yagüe-Martínez, P. Prats-Iraola, F. R. González, R. Brcic, R. Shau, D. Geudtner, M. Eineder, and R. Bamler, "Interferometric Processing of Sentinel-1 TOPS Data," *IEEE Transactions on Geoscience and Remote Sensing*, vol. 54, no. 4, pp. 2220–2234, Apr. 2016.

[10] F. De Zan and A. M. M. Guarnieri, "TOPSAR: Terrain observation by progressive scans," *IEEE Transactions on Geoscience and Remote Sensing*, vol. 44, no. 9, pp. 2352–2360, 2006.

[11] A. Meta, J. Mittermayer, P. Prats, R. Scheiber, and U. Steinbrecher, "TOPS imaging with TerraSAR-X: Mode design and performance analysis," *IEEE Transactions on Geoscience and Remote Sensing*, vol. 48, no. 2, pp. 759–769, 2010.

[12] S. Wollstadt, P. Prats, M. Bachmann, J. Mittermayer, and R. Scheiber, "Scalloping correction in TOPS imaging mode SAR data," *IEEE Geoscience and Remote Sensing Letters*, vol. 9, no. 4, pp. 614–618, 2012.

[13] N. Miranda, P. Meadows, G. Hajduch, A. Pilgrim, R. Piantanida, D. Giudici, D. Small, A. Schubert, R. Husson, P. Vincent *et al.*, "The Sentinel-1A instrument and operational product performance status," in *Geoscience and Remote Sensing Symposium (IGARSS), 2015 IEEE International*. IEEE, 2015, pp. 2824–2827.

[14] P. Prats-Iraola, R. Scheiber, L. Marotti, S. Wollstadt, and A. Reigber, "TOPS interferometry with TerraSAR-X," *IEEE Transactions on geoscience and remote sensing*, vol. 50, no. 8, pp. 3179–3188, 2012.

[15] R. Scheiber, M. Jäger, P. Prats-Iraola, F. De Zan, and D. Geudtner, "Speckle tracking and interferometric processing of TerraSAR-X TOPS data for mapping nonstationary scenarios," *IEEE Journal of Selected Topics in Applied Earth Observations and Remote Sensing*, vol. 8, no. 4, pp. 1709–1720, 2015.

[16] F. De Zan, P. Prats-Iraola, R. Scheiber, and A. Rucci, "Interferometry with TOPS: Coregistration and azimuth shifts," in *EUSAR 2014; 10th European Conference on Synthetic Aperture Radar; Proceedings of*. VDE, 2014, pp. 1–4. [Online]. Available: http://ieeexplore.ieee.org/document/6856955/

[17] P. Potin, B. Rosich, P. Grimont, N. Miranda, I. Shurmer, A. O'Connell, R. Torres, and M. Krassenburg, "Sentinel-1 mission status," in *EUSAR 2016: 11th European Conference on Synthetic Aperture Radar, Proceedings of*. VDE, 2016, pp. 1–6. [Online]. Available: http://ieeexplore.ieee.org/document/7559246/

[18] T. J. Wright, J. Biggs, P. Crippa, S. K. Ebmeier, J. Elliott, P. Gonzalez, A. Hooper, Y. Larsen, Z. Li, P. Marinkovic, B. Parsons, K. Spaans, R. Walters, and M. Ziebart, "Towards Routine Monitoring of Tectonic and Volcanic Deformation with Sentinel-1," in *Proceedings of the ESA FRINGE Workshop, Frascati, Italy*, 2015. [Online]. Available: http://seom.esa.int/fringe2015/files/presentation295.pdf

[19] D. Geudtner, R. Torres, P. Snoeij, and M. Davidson, "Sentinel-1 System Overview ," in *Proceedings of the ESA FRINGE Workshop, Frascati, Italy*. VDE, 2011, pp. 1–6. [Online]. Available: https://earth.esa.int/documents/10174/1567860/Sentinel-1+System_Fringe_final_1.pdf

[20] E. Intrieri, F. Raspini, A. Fumagalli, P. Lu, S. Del Conte, P. Farina, J. Allievi, A. Ferretti, and N. Casagli, "The Maoxian landslide as seen from space: detecting precursors of failure with Sentinel-1 data," *Landslides*, vol. 15, no. 1, pp. 123–133, 2018. [Online]. Available: https://doi.org/10.1007/s10346-017-0915-7

[21] I. J. Hamling, S. Hreinsdóttir, K. Clark, J. Elliott, C. Liang, E. Fielding, N. Litchfield, P. Villamor, L. Wallace, T. J. Wright *et al.*, "Complex multifault rupture during the 2016 M w 7.8 Kaikōura earthquake, New Zealand," *Science*, vol. 356, no. 6334, 2017.

[22] G. Solaro, V. De Novellis, R. Castaldo, C. Luca, R. Lanari, M. Manunta, and F. Casu, "Coseismic Fault Model of Mw 8.3 2015 Illapel Earthquake (Chile) Retrieved from Multi-Orbit Sentinel-1A DInSAR Measurements," *Remote Sensing*, vol. 8, p. 323, 2016.

[23] P. Marinkovic and Y. Larsen, "Subsidence of Beijing (China) mapped by Copernicus Sentinel-1 time series interferometry," Jul. 2016. [Online]. Available: https://doi.org/10.5281/zenodo.57567

[24] D. Geudtner, R. Torres, P. Snoeij, and M. Davidson, "Sentinel-1 System Overview," in *Proceedings of the 9th European Conference on Synthetic Aperture Radar, Nürnberg, Germany*, 2012, pp. 23–26. [Online]. Available: https://dragon3.esa.int/documents/10174/1567860/Sentinel-1+System_Fringe_final_1.pdf

[25] F. Rocca, "Modeling interferogram stacks," *IEEE Transactions on Geoscience and Remote Sensing*, vol. 45, no. 10, pp. 3289–3299, 2007.

[26] F. Gatelli, A. M. Guamieri, F. Parizzi, P. Pasquali, C. Prati, and F. Rocca, "The wavenumber shift in SAR interferometry," *IEEE Transactions on Geoscience and Remote Sensing*, vol. 32, no. 4, pp. 855–865, Jul. 1994.

[27] P. Potin, "Sentinel-1 mission status," in *Proceedings of the ESA FRINGE Workshop, Frascati, Italy*, 2015. [Online]. Available: http://seom.esa.int/fringe2015/files/presentation357.pdf

[28] N. Yagüe-Martínez, F. R. González, R. Brcic, and R. Shau, "Interferometric Evaluation of Sentinel-1A TOPS data," in *Proceedings of the ESA FRINGE Workshop, Frascati, Italy*, 2015. [Online]. Available: http://seom.esa.int/fringe2015/files/presentation204.pdf

[29] E. Sansosti, P. Berardino, M. Manunta, F. Serafino, and G. Fornaro, "Geometrical SAR image registration," *IEEE Transactions on Geoscience and Remote Sensing*, vol. 44, no. 10, pp. 2861–2870, Oct. 2006.

[30] Y. Larsen and P. Marinkovic, "Sentinel-1 TOPS data coregistration operational and practical considerations," in *Proceedings of the ESA FRINGE Workshop, Frascati, Italy*, 2015. [Online]. Available: http://seom.esa.int/fringe2015/files/presentation322.pdf

[31] H. Fattahi, P. Agram, and M. Simons, "A Network-Based Enhanced Spectral Diversity Approach for TOPS Time-Series Analysis," *IEEE Transactions on Geoscience and Remote Sensing*, vol. 55, no. 2, pp. 777–786, Feb. 2017.

[32] N. Yagüe-Martínez, F. De Zan, and P. Prats-Iraola, "Coregistration of Interferometric Stacks of Sentinel-1 TOPS Data," *IEEE Geoscience and Remote Sensing Letters*, vol. 14, no. 7, pp. 1002–1006, 2017.

[33] N. Miranda, "Definition of the TOPS SLC deramping function for products generated by the S-1 IPF," ESA, techreport COPE-GSEG-EOPG-TN-14-0025, 2015. [Online]. Available: https://earth.esa.int/documents/247904/1653442/Sentinel-1-TOPS-SLC_Deramping

[34] R. Piantanida, G. Hajduch, and J. Poullaouec, "Sentinel-1 Level 1 Detailed Algorithm Definition," ESA, techreport SEN-TN-52-7445, 2016. [Online]. Available: https://sentinel.esa.int/documents/247904/1877131/Sentinel-1-Level-1-Detailed-Algorithm-Definition

[35] I. G. Cumming and F. H. Wong, *Digital processing of synthetic aperture radar data: algorithms and implementation*. Artech house, 2005, ch. 6: The Range Doppler Algorithin, p. 245. [Online]. Available: https://books.google.com/books?id=e9xxQgAACAAJ

[36] M. Bara, R. Scheiber, A. Broquetas, and A. Moreira, "Interferometric SAR signal analysis in the presence of squint," *IEEE Transactions on Geoscience and Remote Sensing*, vol. 38, no. 5, pp. 2164–2178, 2000.

[37] A. Ferretti, A. Monti Guarnieri, C. Prati, and F. Rocca, "InSAR processing: a practical approach," in *InSAR Principles: Guidelines for SAR Interferometry Processing and Interpretation*, ser. ESA TM. ESA, 2007. [Online]. Available: https://books.google.com/books?id=f6CbNAAACAAJ

[38] M. Rodriguez-Cassola, P. Prats-Iraola, F. De Zan, R. Scheiber, A. Reigber, D. Geudtner, and A. Moreira, "Doppler-related distortions in TOPS SAR images," *IEEE Transactions on Geoscience and Remote Sensing*, vol. 53, no. 1, pp. 25–35, 2015.

[39] D. Small, "Generation of digital elevation models through spaceborne SAR interferometry," Ph.D. dissertation, University of Zürich, 1998. [Online]. Available: https://www.geo.uzh.ch/dam/jcr:cd893224-28bc-4edd-b4d7-9b9b3e847164/1998_DavidSmall.pdf

[40] D. Geudtner, N. YAGUE-MARTINEZ, P. Prats *et al.*, "Sentinel-1 InSAR Performance: Results from the Sentinel-1A In-Orbit Commissioning," in *Proceedings of the ESA FRINGE Workshop, Frascati, Italy*, 2015. [Online]. Available: http://seom.esa.int/fringe2015/files/presentation367.pdf

[41] M. Schwerdt, K. Schmidt, N. Tous Ramon, P. Klenk, N. Yague-Martinez, P. Prats-Iraola, M. Zink, and D. Geudtner, "Independent system calibration of Sentinel-1B," *Remote Sensing*, vol. 9, no. 6, p. 511, 2017.

[42] P. Prats-Iraola, M. Rodriguez-Cassola, P. Lopez-Dekker, R. Scheiber, F. De Zan, I. Barat, and D. Geudtner, "Considerations of the Orbital Tube for Interferometric Applications," in *Proceedings of the ESA FRINGE Workshop, Frascati, Italy*, 2015. [Online]. Available: http://seom.esa.int/fringe2015/files/Contribution132.pdf

[43] D. Just and R. Bamler, "Phase statistics of interferograms with applications to synthetic aperture radar," *Applied optics*, vol. 33, no. 20, pp. 4361–4368, 1994.

[44] R. Scheiber and A. Moreira, "Coregistration of interferometric SAR images using spectral diversity," *IEEE Transactions on Geoscience and Remote Sensing*, vol. 38, no. 5, pp. 2179–2191, 2000.

[45] S. Mancon, A. Monti Guarnieri, and S. Tebaldini, "Sentinel-1 precise orbit calibration and validation," in *Proceedings of the ESA FRINGE Workshop, Frascati, Italy*, 2015. [Online]. Available: http://seom.esa.int/fringe2015/files/presentation330.pdf

[46] C. Knapp and G. Carter, "The generalized correlation method for estimation of time delay," *IEEE Transactions on Acoustics, Speech, and Signal Processing*, vol. 24, no. 4, pp. 320–327, Aug. 1976.

[47] S. Stein, "Algorithms for ambiguity function processing," *IEEE Transactions on Acoustics, Speech, and Signal Processing*, vol. 29, no. 3, pp. 588–599, Jun. 1981.

[48] R. Bamler and M. Eineder, "Accuracy of Differential Shift Estimation by Correlation and Split-Bandwidth Interferometry for Wideband and Delta-k SAR Systems," *IEEE Geoscience and Remote Sensing Letters*, vol. 2, no. 2, pp. 151–155, Apr. 2005. [Online]. Available: http://ieeexplore.ieee.org/document/1420294/

[49] R. Bamler, "Interferometric stereo radargrammetry: absolute height determination from ERS-ENVISAT interferograms," in *Geoscience and Remote Sensing Symposium (IGARSS), 2000 IEEE International*, vol. 2, 2000, pp. 742–745.

[50] R. F. Hanssen, "Stochastic model for radar interferometry," in *Radar interferometry: data interpretation and error analysis*. Springer Science & Business Media, 2001, vol. 2. [Online]. Available: https://books.google.com/books?id=bqNkJUk4wtMC

[51] G. C. Carter, "Coherence and time delay estimation," *Proceedings of the IEEE*, vol. 75, no. 2, pp. 236–255, 1987.

[52] H. A. Zebker and J. Villasenor, "Decorrelation in interferometric radar echoes," *IEEE Transactions on Geoscience and Remote Sensing*, vol. 30, no. 5, pp. 950–959, Sep. 1992. [Online]. Available: http://ieeexplore.ieee.org/document/175330/

[53] C. Patri and F. Rocca, "Range Resolution Enhancement with Multiple Sar Surveys Combination," in *IGARSS '92 International Geoscience and Remote Sensing Symposium*, vol. 2. IEEE, 1992, pp. 1576–1578. [Online]. Available: http://ieeexplore.ieee.org/document/578637/

[54] F. Serafino, "SAR image coregistration based on isolated point scatterers," *IEEE Geoscience and Remote Sensing Letters*, vol. 3, no. 3, pp. 354–358, 2006.

[55] I. S. Yetik and A. Nehorai, "Performance bounds on image registration," *IEEE Transactions on Signal Processing*, vol. 54, no. 5, pp. 1737–1749, 2006.

[56] J. Li and P. Huang, "A comment on "performance bounds on image registration"," *IEEE Transactions on Signal Processing*, vol. 57, no. 6, pp. 2432–2433, Jun. 2009.

[57] J. Biggs, T. Wright, Z. Lu, and B. Parsons, "Multi-interferogram method for measuring interseismic deformation: Denali Fault, Alaska," *Geophysical Journal International*, vol. 170, no. 3, pp. 1165–1179, 2007.

[58] D. Sandwell, R. Mellors, X. Tong, M. Xu, Xiaohua andWei, and P. Wessel, "GMTSAR: An InSAR Processing System Based on Generic Mapping Tools," UC San Diego: Scripps Institution of Oceanography, techreport, 2011, e.4 Enhanced Spectral Diversity. [Online]. Available: http://topex.ucsd.edu/gmtsar/tar/GMTSAR_2ND_TEX.pdf

[59] R. Grandin, "Interferometric processing of SLC Sentinel-1 TOPS data," in *Proceedings of the ESA FRINGE Workshop, Frascati, Italy*, 2015. [Online]. Available: http://seom.esa.int/fringe2015/files/Contribution116.pdf

[60] A. Hein, "Interferometry," in *Processing of SAR Data*. Springer, 2004.

[61] J. Holzner, "Signal theory and processing for burst-mode and ScanSAR interferometry," Ph.D. dissertation, The University of Edinburgh, 2003. [Online]. Available: http://hdl.handle.net/1842/23054

[62] C. Liang, " Interferometric Processing of Multi-mode Synthetic Aperture Radar Data and the Applications," Ph.D. dissertation, Peking University, 2014.

[63] L. Veci, "Sentinel-1 Toolbox: TOPS Interferometry Tutorial," ESA, techreport, 2016. [Online]. Available: http://sentinel1.s3.amazonaws.com/docs/S1TBX%20TOPSAR%20Interferometry%20with%20Sentinel-1%20Tutorial.pdf

[64] U. Wegnüller, C. Werner, T. Strozzi, A. Wiesmann, O. Frey, and M. Santoro, "Sentinel-1 Support in the GAMMA Software," *Procedia Computer Science*, vol. 100, pp. 1305–1312, 2016. [Online]. Available: http://linkinghub.elsevier.com/retrieve/pii/S1877050916324152

[65] K. Wang, X. Xu, and Y. Fialko, "Improving Burst Alignment in TOPS Interferometry With Bivariate Enhanced Spectral Diversity," *IEEE Geoscience and Remote Sensing Letters*, vol. 14, no. 12, pp. 2423–2427, 2017.

[66] D. Perissin, Z. Wang, and T. Wang, "SARPROZ InSAR Tool for Urban Subsidence/manmade Structure Stability Monitoring in China," in *Proc. of ISRSE 2011, Sidney (Australia)*, 2011.

[67] M. Manunta, P. Berardino, M. Bonano, C. De Luca, S. Elefante, A. Fusco, R. Lanari, M. Manzo, A. Pepe, E. Sansosti, I. Zinno, and F. Casu, "An Efficient Sentinel-1 TOPS SBAS-DInSAR Processing Chain," in *Proceedings of the ESA FRINGE Workshop, Frascati, Italy*, 2015. [Online]. Available: http://seom.esa.int/fringe2015/files/presentation251.pdf

[68] A. Refice, F. Bovenga, and R. Nutricato, "MST-based stepwise connection strategies for multipass radar data, with application to coregistration and equalization," *IEEE transactions on geoscience and remote sensing*, vol. 44, no. 8, pp. 2029–2040, 2006.

[69] T. H. Cormen, C. E. Leiserson, R. L. Rivest, and C. Stein, *Introduction to algorithms third edition*. MIT Applied Mathematics Research eXpress, 2009, ch. Minimum Spanning Trees, pp. 624–642. [Online]. Available: https://mitpress.mit.edu/books/introduction-algorithms

[70] F. Chin and D. Houck, "Algorithms for updating minimal spanning trees," *Journal of Computer and System Sciences*, vol. 16, no. 3, pp. 333–344, 1978.

[71] P. Marinkovic and Y. Larsen, "Sentinel-1 IW mode time-series analysis: When/How/Whether to stitch?" in *Proceedings of the ESA FRINGE Workshop, Frascati, Italy*, 2015. [Online]. Available: http://seom.esa.int/fringe2015/files/presentation323.pdf

[72] H. Fattahi, M. Simons, and P. Agram, "InSAR Time-Series Estimation of the Ionospheric Phase Delay: An Extension of the Split Range-Spectrum Technique," *IEEE Transactions on Geoscience and Remote Sensing*, vol. 55, no. 10, pp. 5984–5996, 2017.

[73] G. Gomba, F. R. González, and F. De Zan, "Ionospheric phase screen compensation for the Sentinel-1 TOPS and ALOS-2 ScanSAR modes," *IEEE Transactions on Geoscience and Remote Sensing*, vol. 55, no. 1, pp. 223–235, 2017.

[74] I. G. Cumming and F. H. Wong, *Digital processing of synthetic aperture radar data: algorithms and implementation*. Artech house, 2005, ch. Chapter 10: Processing ScanSAR Data, p. 432. [Online]. Available: https://books.google.com/books?id=e9xxQgAACAAJ

[75] A. Wiesmann, C. Werner, M. Santoro, U. Wegmuller, and T. Strozzi, "ScanSAR interferometry for land use applications and terrain deformation," in *IEEE International Conference on Geoscience and Remote Sensing Symposium*. IEEE, 2006, pp. 3103–3106.

[76] D. Perissin, *Interferometric SAR Multitemporal Processing: Techniques and Applications*. Cham: Springer International Publishing, 2016, pp. 145–176. [Online]. Available: https://doi.org/10.1007/978-3-319-47037-5_8

[77] A. Ferretti, C. Prati, and F. Rocca, "Permanent scatterers in SAR interferometry," *IEEE Transactions on geoscience and remote sensing*, vol. 39, no. 1, pp. 8–20, 2001.

[78] C. C. Faunt and M. Sneed, "Water availability and subsidence in California's Central Valley," *San Francisco Estuary and Watershed Science*, vol. 13, no. 3, pp. 675–684, 2015. [Online]. Available: http://escholarship.org/uc/item/6qn2711x

[79] C. C. Faunt, M. Sneed, J. Traum, and J. T. Brandt, "Water availability and land subsidence in the Central Valley, California, USA," *Hydrogeology Journal*, vol. 24, no. 3, pp. 675–684, May 2016. [Online]. Available: https://doi.org/10.1007/s10040-015-1339-x

[80] D. L. Galloway, D. R. Jones, and S. E. Ingebritsen, "San Joaquin Valley, California: Largerst Human Alteration of the Earth's Surface," in *Land subsidence in the United States*. US Geological Survey, 1999, vol. 1182. [Online]. Available: https://pubs.usgs.gov/circ/circ1182/

[81] T. G. Farr, "InSAR measurements of subsidence in the Central Valley, California from 2007-present," in *EUSAR 2016: 11th European Conference on Synthetic Aperture Radar, Proceedings of*. VDE, 2016, pp. 1–3. [Online]. Available: http://ieeexplore.ieee.org/document/7559369/

[82] T. G. Farr, C. Jones, and Z. Liu, "Progress report: subsidence in the Central Valley, California," Jet Propulsion Laboratory, California Institute of Technology, Tech. Rep., 2015. [Online]. Available: http://water.ca.gov/groundwater/docs/NASA_REPORT.pdf

[83] T. G. Farr, C. E. Jones, and Z. Liu, "Progress Report: Subsidence in California, March 2015-September 2016," Jet Propulsion Laboratory, California Institute of Technology, Tech. Rep., 2017. [Online]. Available: http://www.water.ca.gov/waterconditions/docs/2017/JPL%20subsidence%20report%20final%20for%20public%20dec%202016.pdf

[84] M. Bakon, M. Marchamalo, Y. Qin, A. J. García-Sánchez, S. Alvarez, D. Perissin, J. Papco, and R. Martínez, "Madrid as Seen from Sentinel-1:

Preliminary Results," *Procedia Computer Science*, vol. 100, pp. 1155–1162, 2016, international Conference on ENTERprise Information Systems/International Conference on Project MANagement/International Conference on Health and Social Care Information Systems and Technologies, CENTERIS/ProjMAN / HCist 2016. [Online]. Available: http://www.sciencedirect.com/science/article/pii/S1877050916324383

[85] F. Canaslan Comut, A. Ustun, M. Lazecky, and D. Perissin, "Capability of Detecting Rapid Subsidence with COSMO SKYMED and Sentinel-1 Dataset over Konya City," in *Living Planet Symposium*, ser. ESA Special Publication, vol. 740, Aug. 2016, p. 295. [Online]. Available: http://www.academia.edu/26649629/CAPABILITY_OF_DETECTING_RAPID_SUBSIDENCE_WITH_COSMO_SKYMED_AND_SENTINEL-1_DATASET_OVER_KONYA_CITY

[86] P. Milillo, R. Bürgmann, P. Lundgren, J. Salzer, D. Perissin, E. Fielding, F. Biondi, and G. Milillo, "Space geodetic monitoring of engineered structures: The ongoing destabilization of the Mosul dam, Iraq," *Scientific Reports*, vol. 6, 2016. [Online]. Available: http://dx.doi.org/10.1038/srep37408

[87] M. Lazecky, F. C. Comut, M. Bakon, Y. Qin, D. Perissin, E. Hatton, K. Spaans, P. J. G. Mendez, P. Guimaraes, J. J. M. de Sousa, D. Kocich, and A. Ustun, "Concept of an Effective Sentinel-1 Satellite SAR Interferometry System," *Procedia Computer Science*, vol. 100, pp. 14–18, 2016, international Conference on ENTERprise Information Systems/International Conference on Project MANagement/International Conference on Health and Social Care Information Systems and Technologies, CENTERIS/ProjMAN / HCist 2016. [Online]. Available: http://www.sciencedirect.com/science/article/pii/S1877050916322852

[88] M. Lazecky, F. Canaslan Comut, Y. Qin, and D. Perissin, "Sentinel-1 Interferometry System in the High-Performance Computing Environment," in *The Rise of Big Spatial Data*, I. Ivan, A. Singleton, J. Horák, and T. Inspektor, Eds. Cham: Springer International Publishing, 2017, pp. 131–139. [Online]. Available: https://link.springer.com/chapter/10.1007/978-3-319-45123-7_10

[89] S. J. Mi, Y. T. Li, F. Wang, L. Li, Y. Ge, L. Luo, C. L. Zhang, and J. B. Chen, "a Research on Monitoring Surface Deformation and Relationships with Surface Parameters in Qinghai Tibetan Plateau Permafrost," *ISPRS - International Archives of the Photogrammetry, Remote Sensing and Spatial Information Sciences*, pp. 629–633, Sep. 2017.

[90] Y. Maghsoudi, F. van der Meer, C. Hecker, D. Perissin, and A. Saepuloh, "Using PS-InSAR to detect surface deformation in geothermal areas of West Java in Indonesia," *International Journal of Applied Earth Observation and Geoinformation*, vol. 64, pp. 386–396, 2018. [Online]. Available: http://www.sciencedirect.com/science/article/pii/S0303243417300788

VITA

Yuxiao QIN received the B.Sc. degree in GIS and Remote Sensing from Peking University, China in 2010; the M.Sc. degree in Earth System Science from the Chinese University of Hong Kong in 2011; the M.Sc. degree in Electrical and Computer Engineering from Purdue University, U.S.A. in 2017. He is currently a doctoral student in the geomatics group, Civil Engineering at Purdue University.

His current research interests include SAR and InSAR data processing and interpretation, SAR time series analysis, and the algorithm and software development for the wide swath mode such as TOPS and ScanSAR.